ABSTRACT

MATHEMATICAL MODELING OF MEMBRANE FILTRATION

by
Pejman Sanaei

The purpose of this thesis is to formulate and investigate new mathematical models for membrane filtration. The work presented is divided into six chapters. In the first chapter the problem is introduced and motivated. In the second chapter, a new mathematical model for flow and fouling in a pleated membrane filter is presented. Pleated membrane filters are widely used in many applications, and offer significantly better surface area to volume ratios than equal area unpleated membrane filters. However, their filtration characteristics are markedly inferior to those of equivalent unpleated membrane filters in dead-end filtration. While several hypotheses have been advanced for this, one possibility is that the flow field induced by the pleating leads to spatially nonuniform fouling of the filter, which in turn degrades performance. This hypothesis is investigated by developing a simplified model for the flow and fouling within a pleated membrane filter. The model accounts for the pleated membrane geometry (which affects the flow), for porous support layers surrounding the membrane, and for two membrane fouling mechanisms: (i) adsorption of very small particles within membrane pores; and (ii) blocking of entire pores by large particles. Asymptotic techniques are used based on the small pleat aspect ratio to solve the model, and solutions are compared to those for the closest-equivalent unpleated filter.

In the third and fourth chapters, mathematical models are proposed to describe the effects of filter membrane morphology on filtration efficiency. A reasonable question that membrane filter manufacturers may ask is: what is the optimal configuration of filter membranes, in terms of internal morphology (pore size and shape), to achieve the most efficient filtration? In order to answer this question, a

robust measure of filtration performance must be first proposed. Filter membrane performance can be measured in a number of different ways. As filtration occurs, the membrane becomes blocked, or fouled, by the impurities in the feed solution, and any performance measure must take account of this. For example, one performance measure might be the total throughput – the amount of filtered feed solution – at the end of filtration process, when the membrane is so badly blocked that it is deemed no longer functional. A simplified mathematical model is proposed, which (i) characterizes membrane internal pore structure via pore or permeability profiles in the depth of the membrane; (ii) accounts for various membrane fouling mechanisms (adsorption and blocking in Chapter 3, and cake formation in Chapter 4); and (iii) defines a measure of filter performance; and (iv) predicts the optimum pore or permeability profile for the chosen performance measure.

In the fifth chapter, a model for more complex pore morphology is described. Many models have been proposed to describe particle capture by membrane filters and the associated fluid dynamics, but most such models are based on a very simple structure in which the pores of the membrane are assumed to be simple circularly-cylindrical tubes spanning the depth of the membrane. Real membranes used in applications usually have much more complex geometry, with interconnected pores which may branch and bifurcate. Pores are also typically larger on the upstream side of the membrane than on the downstream side. An idealized mathematical model is presented, in which a membrane consists of a series of bifurcating pores, which decrease in size as the membrane is traversed. The membrane's permeability decreases as the filtration progresses, ultimately falling to zero. The dependence of filtration efficiency on the characteristics of the branching structure is discussed.

The sixth chapter concludes the thesis with a discussion of future work.

MATHEMATICAL MODELING OF MEMBRANE FILTRATION

by
Pejman Sanaei

A Dissertation
Submitted to the Faculty of
New Jersey Institute of Technology and
Rutgers, The State University of New Jersey – Newark
in Partial Fulfillment of the Requirements for the Degree of
Doctor of Philosophy in Mathematical Sciences

Department of Mathematical Sciences, NJIT
Department of Mathematics and Computer Science, Rutgers-Newark

August 2017

APPROVAL PAGE

MATHEMATICAL MODELING OF MEMBRANE FILTRATION

Pejman Sanaei

Linda J. Cummings, Dissertation Advisor — Date
Professor of Mathematics, New Jersey Institute of Technology

Lou Kondic, Committee Member — Date
Professor of Mathematics, New Jersey Institute of Technology

Michael S. Siegel, Committee Member — Date
Professor of Mathematics, New Jersey Institute of Technology

Ian M. Griffiths, Committee Member — Date
Royal Society University Research Fellow, University of Oxford

---

Emilie Dressaire, Committee Member — Date
Professor of Mechanical and Aerospace Engineering, New York University Tandon School of Engineering

---

Anil Kumar, Committee Member — Date
Principal Process Engineer at Sanofi Genzyme

BIOGRAPHICAL SKETCH

Author: Pejman Sanaei

Degree: Doctor of Philosophy

Date: August 2017

Undergraduate and Graduate Education:

- Doctor of Philosophy in Mathematical Sciences,
  New Jersey Institute of Technology, Newark, NJ, 2017
- Master of Science in Applied Statistics,
  New Jersey Institute of Technology, Newark, NJ, 2016
- Master of Science in Pure Mathematics,
  Shiraz University, Iran, 2009
- Bachelor of Science in Mechanical Engineering,
  Shiraz University, Iran, 2006

Major: Mathematical Sciences

Presentations and Publications:

P. Sanaei, G.W. Richardson, T.P. Witelski and L.J. Cummings, "Flow and fouling in a pleated membrane filter," *Journal of Fluid Mechanics*, 795:36-59, 2016.

P. Sanaei and L.J. Cummings, "Flow and fouling in membrane filters: Effects of membrane morphology," *Journal of Fluid Mechanics*, 818:744-771, 2017.

P. Sanaei and L.J. Cummings, "Optimum permeability profile and fouling in membrane filters," *Preprint.*

P. Sanaei and L.J. Cummings, "Modeling flow and fouling in membrane filters with complex pore morphology," *Preprint.*

P. Sanaei, I.M. Griffiths, L.J. Cummings and S.L. Waters, "Curvature and stress driven tissue growth in a tissue engineering scaffold pore," *Preprint.*

P. Sanaei, L.J. Cummings and I.M. Griffiths, "Comparing a continuum and a network mathematical model for membrane filters," *In preparation.*

P. Sanaei and L.J. Cummings, "Fouling of a filter membrane with complex microstructure: A simplified mathematical model," *Conference Presentation*, Annual Meeting of Society for Industrial and Applied Mathematics, Pittsburgh, 2017.

P. Sanaei and L.J. Cummings, "Modeling of membrane filters, Optimizing internal structure and morphology," *Conference Presentation*, Annual Meeting of Society for Industrial and Applied Mathematics, Student Days Talks, Pittsburgh, 2017.

P. Sanaei and L.J. Cummings, "Mathematical modeling of pleated membrane filters," *Conference Presentation*, Society for Industrial and Applied Mathematics–Computational Science and Engineering, Atlanta, 2017.

L.J. Cummings and P. Sanaei, "Optimizing internal structure of membrane filters," *Conference Presentation*, 69$^{\text{th}}$ Bulletin of the American Physical Society Division of Fluid Dynamics, Portland, 2016.

P. Sanaei and L.J. Cummings, "Modeling branching pore structures in membrane filters," *Conference Presentation*, 69$^{\text{th}}$ Bulletin of the American Physical Society Division of Fluid Dynamics, Portland, 2016.

P. Sanaei and L.J. Cummings, "Optimum permeability profile and fouling in membrane filters," *Conference Presentation*, Annual Meeting of Society for Industrial and Applied Mathematics, Boston, 2016.

L.J. Cummings and P. Sanaei, "Mathematical modeling of membrane filtration," *Conference Presentation*, 19$^{\text{th}}$ European Conference on Mathematics for Industry, Spain, 2016.

P. Sanaei and L.J. Cummings, "Flow and fouling in membrane filters: effects of membrane morphology," *Conference Presentation*, 68$^{\text{th}}$ Bulletin of the American Physical Society Division of Fluid Dynamics, Boston, 2015.

P. Sanaei and L.J. Cummings, "Simplified model for fouling of a pleated membrane filter," *Conference Presentation*, 67$^{\text{th}}$ Bulletin of the American Physical Society Division of Fluid Dynamics, San Francisco, 2014.

I dedicate my dissertation work to my parents' souls.

ACKNOWLEDGMENT

I would like to thank my advisor Professor Linda J. Cummings, for her immense patience, support, and guidance. Professor Cummings has been an inspiration through her enthusiasm and encouragement to pursue exciting ideas, and her practicality and guidance.

I next thank Professors Lou Kondic, Michael Siegel, Emilie Dressaire and Doctors Ian M. Griffiths and Anil Kumar, for being on my thesis committee. Professors Kondic and Siegel have provided invaluable feedback, assistance, and instruction during my time at NJIT. Our collaboration with Professor Dressaire has been very helpful as I have moved forward with my thesis work. I would like to thank Doctor Anil Kumar formerly of Pall Corporation, for his assistance in providing and interpreting experimental data. In particular, I would also like to thank Doctor Ian Griffiths for his guidance and support. His suggestions and critiques are essential in the completion and improvement of this work.

My thanks to the Department of Mathematical Sciences for giving me the opportunity to pursue a degree at such a prestigious university.

In addition, thanks to my family, specifically my lovely wife, Christeen and siblings, Parastoo and Peiman for all of their support during my PhD at NJIT.

Finally, special thanks go to fellow graduate students Emel Khan, Ensela Mema, Randolph J. Leiser, Szu-Pei Fu, Haiyang Qi, Michael Pedneult, Yiming Yu, Li Yu, Mahdi Bandegi, Ivana Seric, Aminur Rahman, Ryan H. Allaire, Binan Gu, Yixuan Sun, Andrew DeStefan, Rui Cao, Matthew Moye and Michael A. Lam for the countless discussions and late nights.

TABLE OF CONTENTS

TABLE OF CONTENTS
(Continued)

Chapter **Page**

LIST OF TABLES

LIST OF FIGURES

LIST OF FIGURES
(Continued)

Figure **Page**

LIST OF FIGURES
(Continued)

Figure **Page**

LIST OF FIGURES
(Continued)

Figure **Page**

LIST OF FIGURES
(Continued)

Figure **Page**

CHAPTER 1

INTRODUCTION

1.1 Introduction and Motivation

Membrane filters – essentially, thin sheets of porous medium which act as filters – are in widespread industrial use, and represent a multi-billion dollar industry in the US alone. Major multinational companies such as W.L. Gore & Associates, and Pall Corporation, manufacture a huge range of membrane-based filtration products, and maintain a keen interest in improving and optimizing their filters. Membrane filtration is used in applications as diverse as water purification [30]; treatment of radioactive sludge [17]; various purification processes in the biotech industry [6, 7, 27, 28]; the cleaning of air or other gases [10]; and beer clarification [51].[1] While the underlying applications and the details of the filtration may vary dramatically (gas vs. liquid filtration; small vs. large particle removal; slow vs. fast throughput; rigid vs. deformable particles), the broad engineering challenge of efficient filtration is the same: to achieve finely-controlled separation at low power consumption.

The desired separation control is to remove only those particles in a certain size range from the input flow (often referred to as "feed" or "challenge solution"); and the obvious resolution to the engineering challenge would appear to be to use the largest pore size and void fraction consistent with the separation requirement. However, these membrane characteristics (and hence the filter's behavior and performance) are far from constant over its lifetime: the particles removed from the feed are deposited within and on the membrane filter, fouling it and degrading the performance over time [5, 21, 30]. The processes by which this fouling occurs are complex, and depend strongly on several factors, including: the internal structure of the membrane [27]; the

[1] The literature is large; the references included for these applications are examples only.

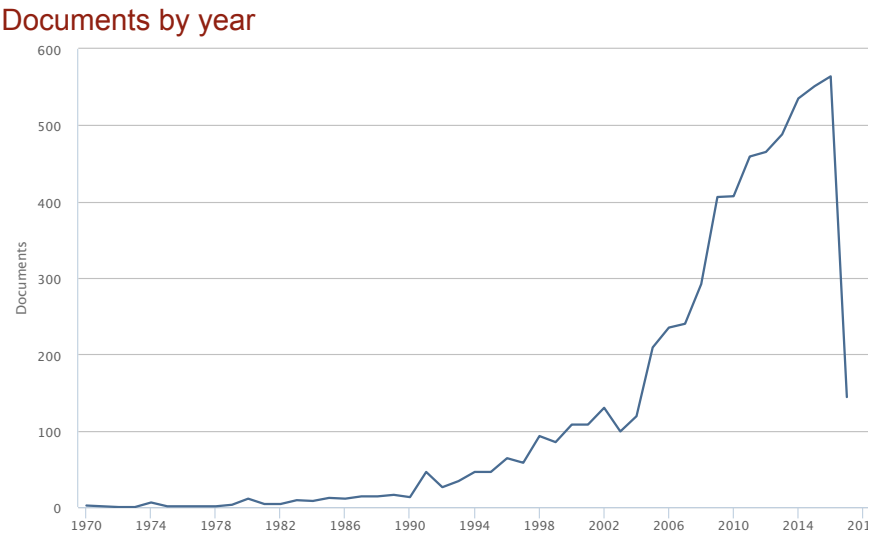

Figure 1.1 Data on publications whose title, abstract or keywords contain the words "membrane" and "filtration" and "fouling".
Source: *https://www.scopus.com.*

flow characteristics of the feed solution [7,9,10,26]; and the type of particles in the feed (the shape, size, and chemistry affects how they are removed by the membrane [13]).

With the widespread industrial use of filters, the associated literature is large and covers all aspects of membrane filtration processes, from membrane preparation and manufacture, through characterization, to performance analysis, and includes both theoretical and experimental modeling. By analyzing the literature on the subtopic of membrane fouling, a search on `www.scopus.com` yields 6317 documents over the last 47 years, the last 8 years each offering 400 to 600 new publications; see Figure 1.1. The area is clearly still of increasing interest; it is notable that the experimental literature far outweighs the theoretical; and among the theoretical literature, there is a paucity of studies that offer first-principles, predictive mathematical models [30].

Iritani [30] recently compiled a very useful review of the membrane fouling literature between 1935 and 2013, paying particular attention to the theoretical modeling literature (other review papers exist of course, e.g., [5], [52], but this is

one of the most recent and comprehensive). The existing modeling literature is predominantly engineering in nature; fewer than 0.5% of the papers depicted in Figure 1.1 are classified as Mathematics. The accepted practice in the filtration literature is to classify membrane fouling (pore-blocking) into different types or regimes: *complete blocking* (individual particles land on individual pores and seal completely); *intermediate blocking* (individual particles land either on open pores, or on top of already blocked pores); *standard blocking* (pores become internally stenosed by deposition of small particles); and *cake filtration* (a dense "cake" layer of particles builds up on the upstream side of the filter). Each regime is associated with different flow characteristics, and different sub-models have been proposed for the regimes [30]. The focus in each sub-model depends on the type of filtration scenario: the two most common scenarios are filtration under constant pressure drop; and filtration at constant prescribed flux. In the former case, the modeling emphasis is on obtaining explicit relationships between the instantaneous filtration rate $Q(t)$ at time t, and the total volume $V(t)$ of filtrate collected (essentially, $V = \int_0^t Q\, dt'$); while in the latter case, the relationship between the pressure required to sustain the constant flux, and the volume $V(t)$ processed, is more relevant to the efficiency of the filtration.

In *complete blocking*, the accepted sub-model assumes a decrease in available membrane area that is linear in the volume V processed. *Partial blocking* also assumes a V-dependent decrease in available area, but with an exponential dependence on V. This model was historically proposed entirely empirically, and for nearly 50 years lacked any firm theoretical or mechanistic understanding (though it has since been interpreted from a mechanistic viewpoint [22, 25, 26]). In *standard blocking*, pores (assumed identical and cylindrical) are assumed to constrict [44] such that pore volume decreases proportionally to filtrate volume $V(t)$, leading ultimately to total constriction. The *cake filtration* regime is modeled by including a layer of increasing thickness (growing proportionally to the filtrate volume $V(t)$) on the upstream side of

the membrane, which adds a further resistance in series with that of the membrane. Individual sub-models have been combined pairwise to construct hybrid models that can describe situations where two of these fouling mechanisms operate simultaneously [6,21]. There is also a variety of stochastic approaches, exemplified in [8,12–15,50,53].

Notwithstanding this activity and progress, a complete and coherent predictive framework that can realistically describe all fouling modes of a membrane filter is still lacking. Iritani concludes his review by noting that "... further development of simple yet effective mathematical models for elucidating the complicated pore-blocking phenomena in membrane filtration would be highly desirable for guiding decisions on the optimal choice of the membrane and membrane-cleaning strategy in industrial use. In particular, there is the increasingly critical need to develop models which are applicable ... also to [feeds] containing a wide variety of [impurities]" [30]. This view is echoed by contacts in the Research & Development sections of W.L. Gore & Associates, and at Pall Corporation. In conversations with Doctors A. Kumar (formerly of Pall Corporation) and S. Swaminathan (formerly of W.L. Gore & Associates) they have underscored the importance of understanding how the complex internal structure of a membrane can affect the results of filtration, something that at present is not well modeled [2]. These issues of particle size distribution within the feed solution, and of nonuniform internal membrane structure, are aspects that will be investigated via first-principles modeling, analysis and simulations.

This thesis is concerned with the development, analysis and computational simulation of new models governing membrane filtration, in several situations of widespread practical interest: (i) flow and fouling within pleated filter cartridges, (ii) membrane fouling models for internally heterogeneous membranes, (iii) modeling membrane filtration with multiple fouling mechanisms: the effect of permeability variations; and (iv) modeling flow and fouling in membrane filters with complex pore morphology. In all scenarios, we will build models that account for an arbitrary

particle size distribution within the feed solution, and account also for a distribution of membrane pore sizes [50]. The work completed to date on these problems in Chapters 2, 3, 4 and 5, and outline our current work and future directions is described in Chapter 6. First-principles theoretical studies of these scenarios should be of interest to those carrying out fundamental experimental research on such systems, as well as to those seeking to extend the scope of current applications and improve on manufacturing processes.

CHAPTER 2

FOULING OF A PLEATED FILTER

2.1 Introduction

Pleated membrane filter cartridges are used in a wide variety of applications to remove particles and undesired impurities of a certain size range from a fluid. A typical filter design is shown in Figure 2.1: a membrane filter (with pore size chosen depending on the particular application) is sandwiched between two, much more porous, support layers. The resulting three-layer structure is pleated and packed into an annular cylindrical cartridge with mesh walls. This arrangement is placed within a larger impermeable housing and attached to a feed supply pump (Figure 2.2), which forces the feed solution through the cartridge from the outer to the inner wall. This design has the advantage that a large filtration surface area can be confined to a small volume, allowing for rapid filtration. However, filtration performance, as measured by flux processed for a given pressure drop, is inferior when compared to the equivalent area flat (non-pleated) membrane in dead-end filtration. The precise reasons for this difference in performance have so far proved elusive, and likely involve several factors: for example, the porous support layers that surround the pleated membrane add resistance, which increases as the pleat packing density (PPD) within the cartridge increases; the fluid dynamics through the pleated structure are much more complex than in dead end (unidirectional) filtration through a non-pleated filter; and the membrane filter itself may become damaged during the process of pleating. Recent studies have focused mainly on elucidating, empirically, how filter cartridge performance scales with any given factor such as PPD; see, e.g., [9, 11, 20, 35, 36]. In this chapter, the focus is on the fluid-dynamical aspects of filtration, in particular: how the pleated geometry affects fluid flow through the filter; how particles carried

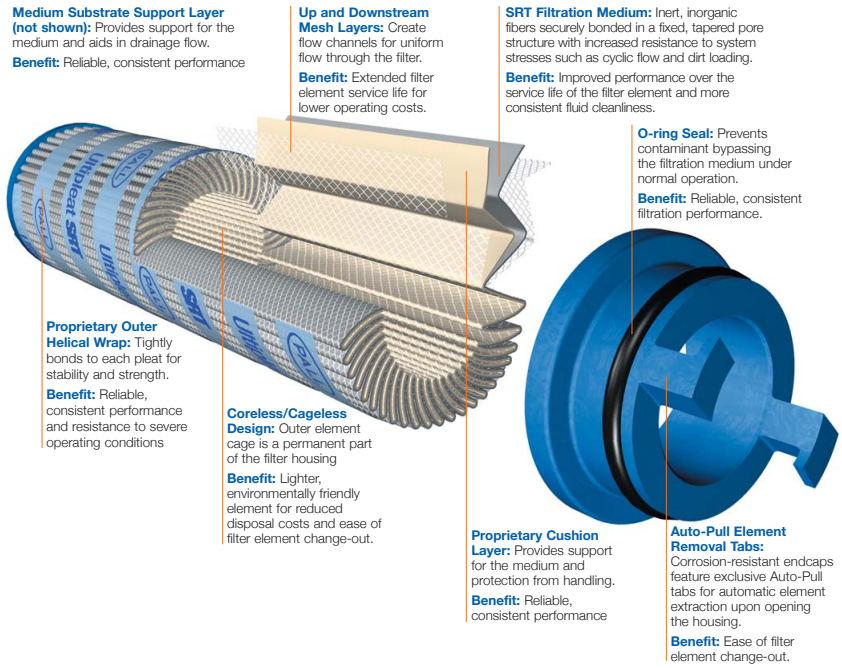

Figure 2.1 Typical geometry of a pleated membrane filter cartridge. Reproduced, with permission, from Pall's Power Generation Catalog. *Source: [1].*

by the flow are deposited on and within the filter membrane; and how this fouling affects the total flux through the filter (and hence its performance).

During membrane filtration, the pores of the membrane become fouled with impurities, which are carried by the feed solution. Filter performance thus ultimately deteriorates, via a combination of mechanisms: (i) Particles smaller than the membrane pore size are deposited (or *adsorbed*) within the pores, shrinking the pore diameter and increasing membrane resistance. (ii) Particles larger than the pores cannot pass through the membrane. Assuming that such particles follow streamlines (large particle Péclet number, leading to passive advection), they will be sieved out and deposited on top of pores, *blocking* them. (iii) Once pores are blocked in this way, in the late stages of filtration, larger particles can form a *cake* on top of the membrane, adding additional resistance via another porous layer on top. By the time this stage is reached the filtration is very inefficient due to the high resistance, and filters are normally discarded (or cleaned) before significant caking has occurred.

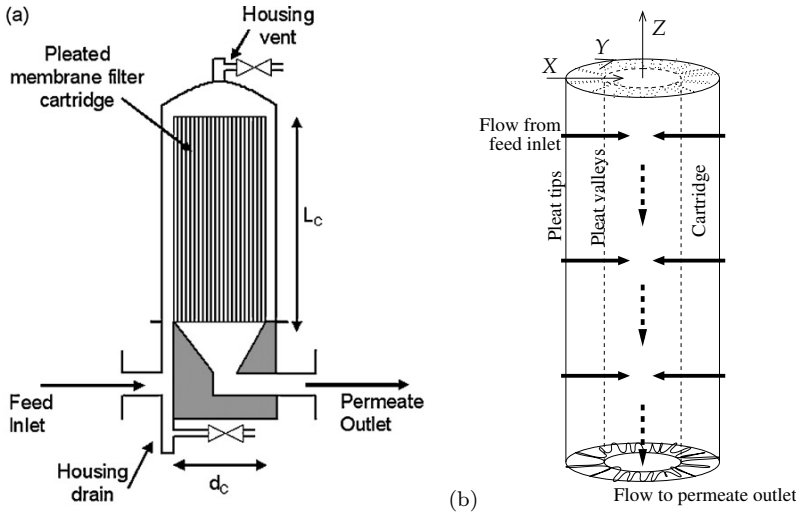

Figure 2.2 (a) Schematic showing the external housing and pleated filter cartridge within it. (b) Idealization of the pleated filter cartridge geometry, indicating also the coordinates used in the model (X is measured in the inward radial direction, while Y is arc length along the outer cylinder boundary, measured as indicated). *Source: [10], (reproduced with permission).*

Mathematical models for all three fouling mechanisms have been proposed, mostly based on empirical laws of how membrane resistance relates to total volume processed, or net flow-rate through the membrane, in the different fouling regimes (see, for example, [6, 17, 21, 39, 51], among many others). In this chapter, we take a different approach that carefully accounts for the fluid dynamics induced by the pleat geometry and couples the fluid dynamics to a first-principles model for fouling (via adsorption (i) and blocking (ii)).

An important early study on mathematical modelling of filtering problems is the work presented in [33]. This research makes use of approaches that are similar in spirit to ours. These authors also consider flow through a two-dimensional pleated filter, and exploit (as we do) the small aspect ratio of the pleat to simplify the fluid dynamics and fouling problems. The work differs from ours in several key respects however. First, there is no porous support material separating the pleats in that work, so that flow between the pleats is modelled as Stokes flow rather than Darcy flow. Second, fouling of the pleated filter is assumed to occur only via the caking referred

to in (iii) above (in the applications we consider this is the "end stage" of the fouling process, when the filter is nearing the end of its useful life). A primary focus of [33] is tracking and analysing mathematically the cake boundary as it builds up. Once cake has formed on the filter surface, that part of the filter admits no flux through it, in contrast to our model, where blockage of a pore simply increases the resistance locally. Thirdly, the work of [33] focuses on the case of a constant prescribed flux, whereas we consider the case of flow driven by a constant pressure drop, so that as fouling occurs, the flux through our filter drops to zero. While the geometry of our filtering problem corresponds to that of [33], our formulation was done independently of their work and for completeness we provide all details of the derivation of our model.

This chapter is laid out as follows: in Section 2.2, we develop a mathematical model for the flow through a pleated sandwich of membrane filter and porous support layers. We consider the case of high pleat packing density (PPD), using an asymptotic approach to exploit both the small aspect ratio of a pleat and the thinness of the membrane relative to the support layers. The model contains the membrane permeability $K_{\mathrm{m}}(\mathbf{X};T)$, which evolves as a function of space and time. Initially, this is constant, but as particles are deposited on and within the membrane, spatial variation develops according to our proposed membrane fouling model. The model we develop has several different features: we illustrate these by means of representative solutions, and we compare the pleated filter with the closest equivalent flat (non-pleated) filter, in Section 2.3. In order to make a meaningful comparison, and to identify the performance difference due to the pleated geometry, we compare to a flat filter surrounded by the same thickness of support material as the pleated filter (details of the solution for this simple one-dimensional model are included in the appendix). We conclude with a discussion in Section 2.4.

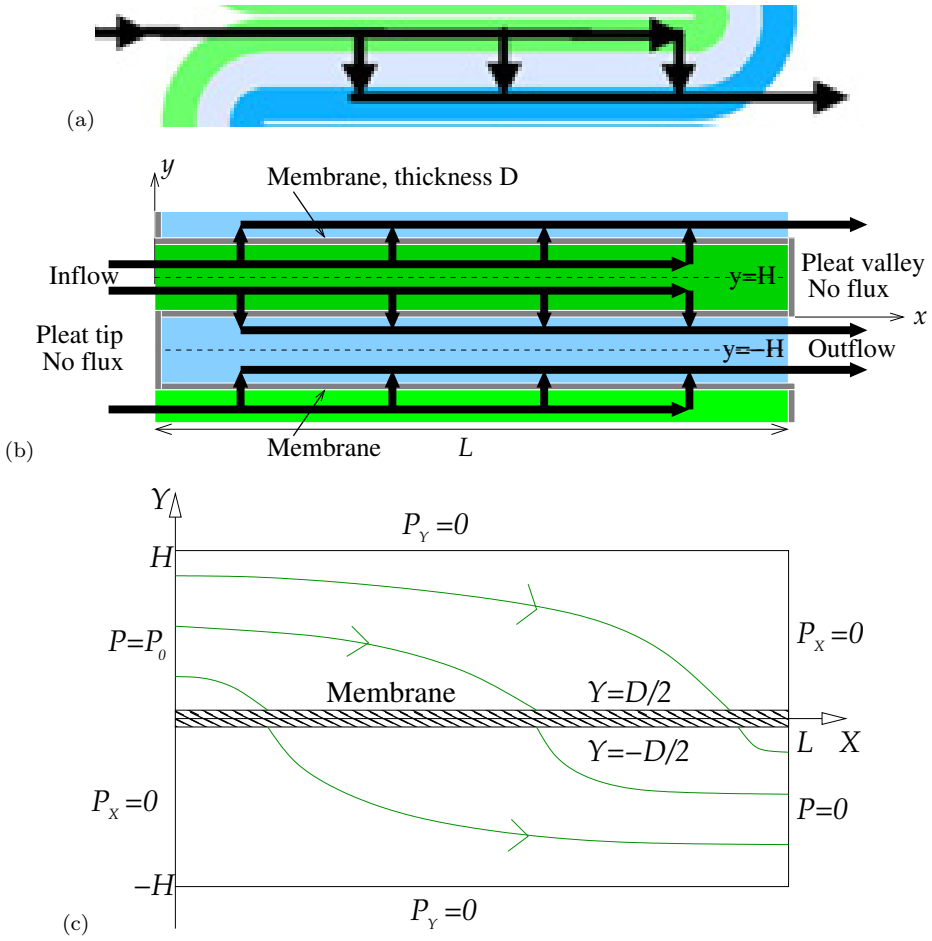

Figure 2.3 (a) Section of the pleated geometry, which is repeated periodically (adapted from [20]). The Z-axis in Figure 2.2(b) is here perpendicular to the page. Green/blue correspond to support layers exterior/interior to the annulus; grey represents the membrane filter (in reality much thinner than the support layers), and the heavy black arrows indicate the flow direction. (b) Idealized membrane geometry to be considered in our model. Symmetry lines (dashed) are located at $Y = \pm H$, and the straight portion of the pleat occupies $0 \leq X \leq L$. (c) The problem domain and boundary conditions at inlet and outlet. Some schematic flow streamlines are also shown.

2.2 Mathematical Modeling

2.2.1 Modeling Assumptions: Outline

The geometry of a cylindrical pleated membrane filter cartridge is sketched in Figures 2.1–2.2 and described in the Introduction. Figure 2.2(b) also introduces the coordinates that will be used in this chapter: the Z-direction is along the cylinder's axis, the X-direction is radially *inwards* measured from the cartridge outer wall, and Y is arc length around the outer cylinder boundary, measured as indicated. We idealize the rather complicated flow scenario depicted in Figure 2.2 in several ways. We assume there is no variation in the Z-direction, and that all pleats are identical. This justifies our considering flow confined to a cross-section at constant Z, within a single pleat, which we assume to be part of a periodic array (periodic in arc length Y). We simplify further by neglecting the curvature of the cylindrical cartridge, considering instead one section of a linear periodic array in rectangular cartesian (X, Y)-coordinates. We restrict our attention to the case of tightly-packed pleats, as shown in Figure 2.3(a). In this situation, the length L of the pleat (from outer to inner cartridge boundary; X-direction in Figures 2.2(b) and 2.3(b)) is much greater than the pleat thickness (the thickness of support layers plus membrane in the Y-direction), so that the vast majority of the flow through the pleat is expected to pass through the pleat length rather than its ends. This observation suggests neglecting the flow through the ends of the pleats (the pleat tips and valleys) as being negligible relative to the flow through the straight section of the membrane (the section parallel to the X-axis). With this in mind, we make our final simplification, idealizing the pleat geometry to be rectangular and imposing no-flux conditions at pleat tips and valleys where shown in Figure 2.3(b). This simplification is justified further (i) by noting that the high membrane curvature in the pleat tips and valleys is likely to lead locally to very low membrane permeability and high resistance to flow (particularly on the inside of the tight curve); and (ii) by limited experimental data [19] on filters subjected to

dust-laden air and then analyzed, which indicate little or no dust particle deposition at the actual fold locations.

The sketches in Figures 2.3(b) and (c) summarize the simplified flow problem to be solved. Figure 2.3(b) clarifies how the pleat geometry of 2.3(a) is idealized (the same color coding is used to distinguish between inflow and outflow sides of the membrane), while Figure 2.3(c) shows the solution domain, with the boundary conditions to be applied on the pressure. The flow region considered is from the lower to the upper periodicity boundary (the dashed symmetry lines in Figure 2.3(b)): $-H \leq Y \leq H$, and from $X = 0$ to $X = L$ along the membrane, with the membrane itself occupying region $-D/2 \leq Y \leq D/2$, $0 \leq X \leq L$ (hatched region in Figure 2.3(c)). Our small aspect ratio assumptions, to be discussed further below, are represented by the dimensionless parameters $\epsilon = H/L \ll 1$, $\delta = D/H \ll 1$. Figures 2.3(b) and (c) also indicate the inflow and outflow, the no-flux boundaries at the pleat valley ($X = L$, $0 \leq Y \leq H$) and tip ($X = 0$, $-H \leq Y \leq 0$), and the symmetry conditions at the support layer mid-surfaces ($Y = \pm H$). In general throughout this thesis, we use upper-case characters to denote dimensional variables, while the lower-case equivalent will be dimensionless.

The tight packing means that the whole flow domain considered is occupied by porous medium (support layer or membrane), within which Darcy flow of an incompressible Newtonian feed solution, viscosity μ, is assumed, with velocity $\mathbf{U} = (U, V)$ and pressure P. We assume the feed solution to be a dilute suspension of particles, which are advected passively through the support layers. The permeabilities of support layers and membrane are K, K_{m}, respectively, with $K_{\mathrm{m}}/K \ll 1$ in accordance with data for real filter cartridges (see Table 2.1). We allow support layer permeability K to vary along the pleat,[1] but assume it is symmetric above

[1]Due to the annular configuration of the cartridge, the valley ends of pleats will be more compressed than the tip ends, leading to lower permeability at the valleys; see Figures 2.1 and 2.2).

and below the membrane. For the most part, we assume that K varies only in the coordinate X along the pleat, $K(X)$; the case of permeability that can vary also in the Y direction, $K(X,Y)$, is discussed briefly in Section 2.2.3. In general, K_{m} will vary in both space and time as membrane fouling occurs, with the variation in time being quasi-static: $K_{\mathrm{m}}(X,T)$.[2] The time evolution of the membrane permeability similarly induces time variation into the solution for the pressure and fluid velocity within the pleat. However, since no explicit time-dependence appears in the Darcy flow model, we will mostly suppress the time dependence to simplify notation, writing $K_{\mathrm{m}}(X)$, $P(X,Y)$, etc. This (quasi-static) assumption that only the dynamics of membrane fouling need explicit consideration amounts to an assumption (borne out by data) that fouling occurs on a timescale long compared with that of fluid transit time across the pleated cartridge.

To arrive at a tractable fouling model, we consider a membrane composed of an identical array of uniformly distributed cylindrical pores of radius $A(T)$. Within our model, membrane resistance is assumed to increase in time due to fouling by two mechanisms: (i) $A(T)$ decreases in time due to *adsorption* of tiny particles within the pores; and (ii) pores become *blocked* from above by particles too large to pass through pores. In order to model (ii), we monitor $N(X,T)$, the number of unblocked pores per unit area of membrane. Again, we will mostly suppress the time-dependence here to simplify notation, writing just A and $N(X)$. Membrane permeability will be expressed as a function of both A and N.

2.2.2 Governing Equations

The feed is assumed to be a dilute suspension of particles, which do not affect the fluid dynamics directly (though they do have an indirect effect via the fouling, which results in increased system resistance). We therefore use a single-phase model, in

[2]We do not account for any fouling of the support layers, which are not designed to capture particles: the pores of these layers are very much larger than those of the membrane filter.

which Darcy velocity $\mathbf{U} = (U, V)$ within the support layers is given in terms of the pressure $P(X, Y)$ by

$$\mathbf{U} = (U, V) = -\frac{K}{\mu}\nabla P, \quad \nabla = (\partial_X, \partial_Y). \tag{2.1}$$

Incompressibility of the feed solution requires

$$\nabla \cdot \mathbf{U} = 0 \quad \Rightarrow \quad \nabla \cdot (K\nabla P) = 0, \tag{2.2}$$

within the support layers. As discussed in Section 2.2.1 above, we assume that the flow is driven by an imposed pressure difference, P_0, across the pleated membrane; that there is no flux through the pleat valley on the inflow side and the pleat tip on the outflow side; and we impose symmetry across the support layer centerlines $Y = \pm H$ (see Figure 2.3). Hence, we impose boundary conditions

$$P^+(0, Y) = P_0,\ P_X^+(L, Y) = 0,\ P_Y^+(X, H) = 0, \tag{2.3}$$

$$P_X^-(0, Y) = 0,\ P^-(L, Y) = 0,\ P_Y^-(X, -H) = 0, \tag{2.4}$$

where we use $\pm$ superscripts to distinguish between quantities evaluated in $Y \gtrless 0$ respectively, on either side of the membrane. For most of our simulations, we take P_0 to be a specified constant, reflecting flow driven by a fixed pressure drop between inlet and outlet; but we will also present some results for fixed-flux scenarios, where P_0 increases in time in order to maintain the same flux as the system resistance increases due to fouling (see Section 2.2.3).

Similar to (2.1), we also assume Darcy flow across the membrane, which is itself a porous medium, though much less permeable than the support layers. We are primarily concerned with the flux, V_{m}, per unit area across the membrane in the Y-direction. Anticipating in advance the fact that the pressure within the membrane will be independent of the coordinate Y perpendicular to the membrane (due to

the small aspect ratio $D/L = \epsilon\delta \ll 1$), and given that the pressure is continuous across the interface between the membrane and support layers, the vertical pressure gradient within the membrane may be written, correct to leading order in $\epsilon\delta$, as $(P^+|_{Y=D/2} - P^-|_{Y=-D/2})/D$. The Darcy law for the flow through the membrane then gives

$$|V_{\rm m}| = \frac{K_{\rm m}}{\mu D}\left[P^+\big|_{Y=D/2} - P^-\big|_{Y=-D/2}\right], \qquad 0 \le X \le L, \tag{2.5}$$

where, by continuity of flux, $|V_{\rm m}(X)| = |V(X, D/2)| = |V(X, -D/2)|$ (with V as defined in (2.1)),

$$|V_{\rm m}| = \frac{K}{\mu}\left.\frac{\partial P^+}{\partial Y}\right|_{Y=D/2} = \frac{K}{\mu}\left.\frac{\partial P^-}{\partial Y}\right|_{Y=-D/2}, \qquad 0 \le X \le L. \tag{2.6}$$

The total flux through the membrane, Q (per unit length along the axis of the cartridge), which will be an important performance characteristic in our simulations, is defined by

$$Q = \int_0^L |V_{\rm m}| dX = \int_0^L \frac{K}{\mu}\left.\frac{\partial P^+}{\partial Y}\right|_{Y=D/2} dX. \tag{2.7}$$

Membrane permeability $K_{\rm m}$ changes, over timescales long compared to the fluid transit time, due to pore shrinkage (arising from particle adsorption) and to blocking of pores by large particles. We now consider these fouling phenomena in more detail. We assume that membrane pores are long thin cylindrical tubes, of length D and radius $A(T)$, spanning the membrane, which initially all have the same radius, $A(0) = A_0$. A more sophisticated model would allow for non-uniform shrinkage of pores due to the adsorption, but in our simple model, we assume uniform adsorption, so that the pore radius does not vary spatially. Where an individual pore (at position X and time T) is unblocked the total flux through it $Q_{\rm u,pore}(X, T)$ is given (approximately) by the Hagen-Poiseuille formula

$$Q_{\rm u,pore} = \frac{1}{R_{\rm u}}(P^+|_{Y=D/2} - P^-|_{Y=-D/2}) \quad \text{where} \quad R_{\rm u} = \frac{8\mu D}{\pi A^4}, \tag{2.8}$$

and $R_{\rm u}$ is the pore resistance. Blocking occurs when a large particle becomes trapped at the entrance to a pore, obstructing the flow. We model this effect by adding an extra resistance of magnitude $8\mu D\rho_{\rm b}/(\pi A_0^4)$, where $\rho_{\rm b}$ is a dimensionless number, in series with the Hagen-Poiseuille resistance $R_{\rm u}$. The flux through a blocked pore, $Q_{\rm b,pore}(X,T)$, is thus given by

$$Q_{\rm b,pore} = \frac{1}{R_{\rm b}}(P^+|_{Y=D/2} - P^-|_{Y=-D/2}) \quad \text{where} \quad R_{\rm b} = \frac{8\mu D}{\pi A_0^4}\left(\left(\frac{A_0}{A}\right)^4 + \rho_{\rm b}\right). \tag{2.9}$$

The dimensionless parameter $\rho_{\rm b}$ characterizes blocking strength: for large values of $\rho_{\rm b}$ pore resistance increases dramatically after blocking, while for small values resistance is almost unchanged. In the limit $\rho_{\rm b} \to \infty$, our model captures the simplest blocking assumption; that deposition of a large particle over a pore blocks it completely.

We can now relate the number densities of unblocked and blocked pores, $N(X,T)$ and $N_0 - N(X,T)$ respectively (where $N_0 = N(X,0)$), to the membrane permeability $K_{\rm m}$ by noting that the flux $|V_{\rm m}|$ of fluid (per unit area of membrane) is

$$|V_{\rm m}| = N(X,T)Q_{\rm u,pore} + (N_0 - N(X,T))Q_{\rm b,pore}$$

so that, on substituting for $Q_{\rm u,pore}$ from (2.8) and for $Q_{\rm b,pore}$ from (2.9) in the above and comparing to (2.5), we obtain

$$K_{\rm m} = \frac{\pi A_0^4}{8}\left(\frac{N}{(A_0/A)^4} + \frac{N_0 - N}{(A_0/A)^4 + \rho_{\rm b}}\right). \tag{2.10}$$

To complete the model, we need equations describing the evolution of $N(X,T)$, the local number density of unblocked pores, and $A(T)$ the pore radius. We assume a pore is blocked whenever a particle with radius $S > A(T)$ is advected to the pore entrance. If we assume a cumulative particle size distribution function $G(S)$, giving the number of particles per unit volume of fluid with radius smaller than S, then the concentration of particles of size $S > A(T)$ is $G_\infty - G(A)$ (where $G_\infty = \lim_{S\to\infty} G(S)$ is the total particle concentration). The probability that a particular pore is blocked

(per unit time) is thus $(G_\infty - G(A))$ multipled by the flux through the pore, $Q_{\text{u,pore}}$ (given by (2.8)):

$$\left[\begin{array}{c}\text{Probability per unit time that}\\ \text{pore of radius } A \text{ is blocked}\end{array}\right] = \frac{\pi A^4}{8\mu D}(G_\infty - G(A))(P^+|_{Y=D/2} - P^-|_{Y=-D/2}).$$

Given that, we assume unblocked pores all have radius $A(T)$, the number of pores blocked per unit time, per unit area, is equal to $N(X,T)$ times the probability, per unit time, that a pore of radius $A(T)$ is blocked. It follows that the rate of change of the number density (per unit area) of unblocked pores, is given by

$$\frac{\partial N}{\partial T} = -N\frac{\pi A^4}{8\mu D}(G_\infty - G(A))(P^+|_{Y=D/2} - P^-|_{Y=-D/2}). \tag{2.11}$$

In order to describe fouling, we make the simplest possible assumption, namely uniform adsorption within the pores, so that particle radius decreases uniformly according to

$$\frac{\partial A}{\partial T} = -E, \quad A|_{T=0} = A_0, \tag{2.12}$$

for some constant E. Deposition within pores in reality will be controlled by a complex interplay between suspended particles in the feed, and the membrane material, the details of which will vary from one system to another; in the absence of detailed experimental data, our model reflects an assumption that the rate of loss of pore area is proportional to the pore circumference only, other effects being largely the same from one pore to another.

All our simulations will be conducted with an exponential cumulative particle distribution of the form

$$G(S) = G_\infty(1 - e^{-BS}), \tag{2.13}$$

where B^{-1} is a characteristic particle size. This functional form was not chosen to fit to any specific dataset, but has the general features required. While some particle size distributions characterized in the literature (see, *e.g.*, [21], with two distinct characteristic particle sizes) are more complicated, we recall that our model implicitly assumes two separate particle size distributions: the "macroscopic" particles modelled by $G(S)$ with pore-blocking potential; and the "microscopic" particles implicit in our pore adsorption model.

2.2.3 Scaling, Nondimensionalization and Asymptotics

Even with the simplifications introduced the model above is complicated, and we therefore exploit asymptotic analysis based on the small aspect ratio of the pleat ($\epsilon = H/L \ll 1$), and on the thinness of the membrane relative to the support layer ($\delta = D/H \ll 1$); see Table 2.2, which summarizes the model parameters and gives estimates, where available. For the most part, we consider filtration driven by a fixed pressure drop, P_0, between inlet and outlet, and this is the basis on which we nondimensionalize below. We will also present some simulations for a prescribed flux scenario, for which the scalings are a little different; we comment briefly on this in Section 2.2.3 below.

Fluid Dynamics In order to exploit the asymptotic simplifications, we introduce dimensionless variables as follows:

$$\begin{aligned} P^{\pm}(X,Y) = P_0 p^{\pm}(x,y), \quad (X,Y) = (Lx, Hy), \\ K(X) = K_{\mathrm{av}} k(x), \quad K_{\mathrm{m}}(X) = K_{\mathrm{m0}} k_{\mathrm{m}}(x), \end{aligned} \tag{2.14}$$

where $K_{\mathrm{av}} = (1/L)\int_0^L K(X)dX$ is the average support layer permeability and K_{m0} is a typical initial membrane permeability. For definiteness, we can take it to be the initial membrane permeability in the expression (2.10), with $A = A_0$ and $N = N_0$. For conciseness in the following, we will indicate dependence on variables only

where necessary, but it should be understood that all functions except the support layer permeability k vary in both space and time. In the dimensionless coordinates, our idealized problem for the pressure $p^{\pm}(x,y)$ within the support layers (equations (2.2)–(2.4)) becomes

$$\epsilon^2(k(x)p_x^+)_x + (k(x)p_y^+)_y = 0, \quad \delta/2 \le y \le 1, \tag{2.15}$$

$$p^+(0,y) = 1, \quad p_x^+(1,y) = 0, \quad p_y^+(x,1) = 0, \tag{2.16}$$

$$\epsilon^2(k(x)p_x^-)_x + (k(x)p_y^-)_y = 0, \quad -1 \le y \le -\delta/2, \tag{2.17}$$

$$p_x^-(0,y) = 0, \quad p^-(1,y) = 0, \quad p_y^-(x,-1) = 0. \tag{2.18}$$

This system is closed by enforcing flux continuity across the membrane, equations (2.5) and (2.6), which gives

$$p_y^+|_{y=\delta/2} = p_y^-|_{y=-\delta/2} = \epsilon^2\Gamma\frac{k_{\mathrm{m}}(x)}{k(x)}\left[p^+|_{y=\delta/2} - p^-|_{y=-\delta/2}\right], \tag{2.19}$$

where the key dimensionless parameter Γ is defined by

$$\Gamma = \frac{K_{\mathrm{m0}}L^2}{K_{\mathrm{av}}HD} \tag{2.20}$$

and gives a scaled measure of the relative importance of the resistance of the packing material to that of the membrane, such that if $\Gamma \gg 1$ the packing material provides most of the resistance whereas if $\Gamma \ll 1$ the membrane provides most of the resistance. We now seek asymptotic solutions for $p^{\pm}$ in the distinguished limit $\Gamma = O(1)$, $\epsilon \ll 1$ and $\delta \ll 1$ (note that our solution is asymptotically valid for all $\Gamma \ll 1/\epsilon^2$) by expanding $p^{\pm}$ in powers of ϵ as follows:

$$p^+(x,y) = p_0^+(x) + \epsilon^2 p_1^+(x,y) + \cdots, \quad p^-(x,y) = p_0^-(x) + \epsilon^2 p_1^-(x,y) + \cdots. \tag{2.21}$$

We will determine coupled equations for the as yet unknown functions $p_0^{\pm}(x)$ by seeking a solvability condition on the first order solutions $p_1^{\pm}(x,y)$. This is effected

by substituting the expansions (2.21) into (2.15)-(2.18) and taking the $O(\epsilon^2)$ terms,

$$\frac{\partial}{\partial y}\left(k(x)\frac{\partial p_1^+}{\partial y}\right)+\frac{\partial}{\partial x}\left(k(x)\frac{\partial p_0^+}{\partial x}\right)=0, \tag{2.22}$$

$$\left.\frac{\partial p_1^+}{\partial y}\right|_{y=1}=0, \qquad \left.k(x)\frac{\partial p_1^+}{\partial y}\right|_{y=0^+}=\Gamma k_{\mathrm{m}}(x)(p_0^+-p_0^-), \tag{2.23}$$

$$\frac{\partial}{\partial y}\left(k(x)\frac{\partial p_1^-}{\partial y}\right)+\frac{\partial}{\partial x}\left(k(x)\frac{\partial p_0^-}{\partial x}\right)=0, \tag{2.24}$$

$$\left.\frac{\partial p_1^-}{\partial y}\right|_{y=-1}=0, \qquad \left.k(x)\frac{\partial p_1^-}{\partial y}\right|_{y=0^-}=\Gamma k_{\mathrm{m}}(x)(p_0^+-p_0^-). \tag{2.25}$$

Integrating (2.22) between $y=0$ and $y=1$ and applying the boundary conditions (2.23) leads to a solvability condition in the form of an ODE (in x) for $p_0^+(x)$ and $p_0^-(x)$. Similarly, integration of (2.24) between $y=-1$ and $y=0$ and application of the boundary conditions (2.25) leads to a second ODE. Boundary conditions on these two ODEs come from the leading order terms of (2.16) and (2.18). The resulting simplified model for p_0^+ and p_0^- is

$$\frac{\partial}{\partial x}\left(k(x)\frac{\partial p_0^+}{\partial x}\right)=\Gamma k_{\mathrm{m}}(x)(p_0^+-p_0^-), \tag{2.26}$$

$$\frac{\partial}{\partial x}\left(k(x)\frac{\partial p_0^-}{\partial x}\right)=-\Gamma k_{\mathrm{m}}(x)(p_0^+-p_0^-), \tag{2.27}$$

$$p_0^+|_{x=0}=1, \qquad \left.\frac{\partial p_0^+}{\partial x}\right|_{x=1}=0, \tag{2.28}$$

$$\left.\frac{\partial p_0^-}{\partial x}\right|_{x=0}=0, \qquad p_0^-|_{x=1}=0. \tag{2.29}$$

In addition, p_1^+ and p_1^- can be found by solving the differential equations (2.22) and (2.24) subject to boundary conditions (2.23) and (2.25) respectively, giving

$$p_1^+(x,y)=-\frac{(k(x)p_{0x}^+)_x}{k(x)}\left(\frac{y^2}{2}-y\right)+h^+(x),$$
$$p_1^-(x,y)=-\frac{(k(x)p_{0x}^-)_x}{k(x)}\left(\frac{y^2}{2}+y\right)+h^-(x),$$

for some functions $h^{\pm}(x)$.

This model, at leading order, describes two porous medium flows (with pressures $p_0^+(x)$ and $p_0^-(x)$) separated by a membrane through which fluid is driven (from one side to the other) by the local pressure difference.

Generalization to support layer with y-dependent permeability $k(x,y)$: It is straightforward to generalize this treatment to a support layer with permeability $k(x,y)$. Dependence on y could be introduced by (for example) choice of a support material with a layered structure. The result obtained is identical to (2.26)–(2.29) except that $k(x)$ is replaced by $\hat{k}^+(x)$ in (2.26) and $\hat{k}^-(x)$ in (2.27), where $\hat{k}^+(x)$ and $\hat{k}^-(x)$ are the y-averages of the permeability, above and below the membrane, respectively,

$$\hat{k}^+(x) = \int_0^1 k(x,y)dy \qquad \text{and} \qquad \hat{k}^-(x) = \int_{-1}^0 k(x,y)dy. \tag{2.30}$$

When we come to suggest possible improvements to the pleated filter system in Section 2.4, we will return to this generalized formulation.

The Small Γ Limit: In this limit, the dominant resistance to flow is that of the membrane (as opposed to that of the porous support layers) and, to leading order in Γ, the solution to (2.26)–(2.29) is just

$$p_0^+ = 1 \quad \text{and} \quad p_0^- = 0. \tag{2.31}$$

It is apparent that the situation here is identical to that of a flat membrane across which a constant pressure difference is applied. We would thus expect membrane fouling to occur uniformly along the length of the membrane, leading to optimal membrane performance (see Appendix A and the simulations of Section 2.3).

Method of Solution It is apparent from (2.26) and (2.27) that $(k(x)(p_0^+ + p_0^-)_x)_x = 0$. This statement is readily integrated twice to obtain an expression for p_0^- in terms

of p_0^+

$$p_0^-(x) = -p_0^+(x) - c_1(t)\int_0^x \frac{dx'}{k(x')} - c_2(t) \tag{2.32}$$

for some $c_1(t)$ and $c_2(t)$ (which are independent of x, but will vary in time as fouling occurs). By substituting (2.32) into (2.26), we obtain a single equation for p_0^+ containing two arbitrary functions of time,

$$\left(k(x)p_{0x}^+(x)\right)_x - 2\Gamma k_{\mathrm{m}}(x)p_0^+(x) = \Gamma k_{\mathrm{m}}(x)\left(c_1(t)\int_0^x \frac{dx'}{k(x')} + c_2(t)\right), \tag{2.33}$$

which must be solved subject to the four boundary conditions

$$\begin{aligned} p_0^+|_{x=0} = 1, \qquad p_{0x}^+|_{x=0} = -\frac{c_1(t)}{k(0)}, \\ p_0^+|_{x=1} = -\left(c_1(t)\int_0^1 \frac{dx}{k(x)} + c_2(t)\right), \qquad p_{0x}^+|_{x=1} = 0. \end{aligned} \tag{2.34}$$

Hence, with p_0^+ determined, we have the leading-order solution for the pressure within the support layers, from equations (2.21) and (2.32).

The Flux of Fluid Through the Pleat The total dimensionless flux q, which we will use to characterize membrane performance later, is defined in terms of total dimensional flux Q (equation (2.7)) by $Q = Q_0 q$, where $Q_0 = K_{\mathrm{m}0}P_0L/(\mu D)$. By mass conservation, the total flux of fluid flowing across the membrane is equal to that flowing across the inlet boundary and so

$$q = -\frac{k}{\Gamma}\frac{\partial p_0^+}{\partial x}\bigg|_{x=0}. \tag{2.35}$$

Another useful quantity for understanding the progress of fouling is the flux $|V_{\mathrm{m}}|$ (as defined in (2.6)), per unit area, through the membrane (from top to bottom) as a function of position X along the membrane. When we define the dimensionless analogue, $|v_{\mathrm{m}}|$, of this quantity by $|V_{\mathrm{m}}| = |v_{\mathrm{m}}|K_{\mathrm{m}0}P_0/(\mu D)$, this satisfies the relation

$$|v_{\mathrm{m}}(x,t)| = p_0^+(x,t) - p_0^-(x,t). \tag{2.36}$$

Membrane Fouling The membrane permeability k_{m} and the flow vary in time due only to the fouling by deposited particles, which occurs in a spatially nonuniform manner. In (2.10), we expressed membrane permeability in terms of the pore radius A, and the number of unblocked pores per unit area, N. We scale each of these quantities with their initial values,

$$A = A_0 a, \quad N(X) = N_0 n(x). \tag{2.37}$$

We note further that Eq. (2.11) defines a natural timescale for the problem (that of blocking), while G_∞ gives a natural scale for the particle size distribution, motivating us to rescale as follows:

$$T = \frac{8\mu D}{\pi P_0 G_\infty A_0^4} t, \quad G = G_\infty g(s), \quad S = A_0 s, \quad B = \frac{b}{A_0}, \quad g(s) = 1 - e^{-bs} \tag{2.38}$$

while (2.10) gives a natural choice of K_{m0} and leads to the definition

$$K_{\mathrm{m0}} = \frac{\pi A_0^4 N_0}{8}. \tag{2.39}$$

Applying these rescalings together with our original nondimensionalization (2.14) to equations (2.10), (2.11) and (2.12), we obtain the remaining dimensionless equations in the model

$$k_{\mathrm{m}}(x,t) = a^4 \left(n + \frac{1-n}{1+\rho_{\mathrm{b}} a^4} \right), \tag{2.40}$$

$$\frac{\partial n}{\partial t} = -n a^4 e^{-ba} (p^+|_{y=\delta/2} - p^-|_{y=-\delta/2}), \quad n|_{t=0} = 1, \tag{2.41}$$

$$\frac{\partial a}{\partial t} = -\beta, \quad a|_{t=0} = 1, \tag{2.42}$$

where the dimensionless parameter β is given by

$$\beta = \frac{8\mu E D}{\pi A_0^5 P_0 G_\infty}.$$

Fluid Velocity and Streamfunction in Support Layers: It will be convenient in our simulations to be able to visualize the fluid flow through the support layers. Since the flow within these layers is quasistatic and two-dimensional, a streamfunction ψ may be defined. From the asymptotic solution for the pressure, (2.21), and using the dimensionless form of the Darcy equation, we have dimensionless velocity in the upper and lower support layers given by

$$\mathbf{u}^{\pm}(x,y) = \left(-k(x)p_{0x}^{\pm}(x), (k(x)p_{0x}^{\pm}(x))_x(y \mp 1)\right).$$

From the streamfunction definition

$$\mathbf{u}^{\pm}(x,y) = (\psi^{\pm}(x,y)_y, -\psi^{\pm}(x,y)_x),$$

we find

$$\psi^{+}(x,y) = -k(x)p_{0x}^{+}(x)(y-1), \quad \psi^{-}(x,y) = -k(x)p_{0x}^{-}(x)(y+1) - c_1, \tag{2.43}$$

where the integration constant in ψ^- (the same c_1 that was introduced in Eq.(2.32)) was chosen to match streamlines on the x-axis (the filter membrane location).

Modification for the Constant Flux Case: In the alternative scenario, where the total flux Q_0 through the membrane is fixed instead of the pressure drop, we define the inlet pressure by $P_0\zeta(t)$, where ζ increases monotonically as the membrane is fouled, in such a way as to sustain constant total flux $Q = Q_0$ (as defined by (2.7)). By modifying equation (2.35)

$$\zeta\left[\frac{k}{\Gamma}\frac{\partial p_0^{+}}{\partial x}\right]_{x=0}^{x=1} = q_0, \text{ constant, for all } t, \tag{2.44}$$

with dimensionless flux as defined there.

2.2.4 Model Summary

Our final model is represented by (2.21), (2.32), (2.33), (2.34), (2.40), (2.41), (2.42). At this stage, we now emphasize each quantity that depends on space and/or time. At each instant of time, we must solve the boundary value problem (2.33)

$$\frac{\partial}{\partial x}\left(k(x)\frac{\partial p_0^+(x,t)}{\partial x}\right) - 2\Gamma k_{\rm m}(x,t)p_0^+(x,t) = \Gamma k_{\rm m}(x,t)\left(c_1(t)\int_0^x \frac{dx}{k(x)} + c_2(t)\right), \tag{2.45}$$

subject to conditions (2.34)

$$p_0^+(0,t) = 1,\ p_{0x}^+(0,t) = -\frac{c_1(t)}{k(0)}, \tag{2.46}$$

$$p_0^+(1,t) = -\left(c_1(t)\int_0^1 \frac{dx}{k(x)} + c_2(t)\right),\ p_{0x}^+(1,t) = 0, \tag{2.47}$$

in terms of which the pressures in the support layers are given by (2.21), (2.32). Note that, we have four boundary conditions (2.46), (2.47) for the second-order equation (2.45), which ensures that the unknown functions $c_1(t)$ and $c_2(t)$ are fixed also. The membrane permeability $k_{\rm m}(x,t)$ varies quasistatically in (2.45) due to the fouling; it satisfies (2.40)

$$k_{\rm m}(x,t) = a(t)^4\left[n(x,t) + \frac{(1-n(x,t))}{(1+\rho_{\rm b}a(t)^4)}\right], \quad \text{where} \quad a(t) = 1-\beta t. \tag{2.48}$$

The number density of unblocked pores, $n(x,t)$, varies according to (2.41),

$$\frac{\partial n(x,t)}{\partial t} = -n(x,t)a(t)^4 e^{-ba(t)}\left(2p_0^+(x,t) + c_1(t)\int_0^x \frac{dx}{k(x)} + c_2(t)\right),$$
$$n(x,0) = 1. \tag{2.49}$$

The solution scheme for this system is straightforward: At time $t = 0$ assign $k_{\rm m}(x,0) = k_{m0} = 1$. Then: (i) solve the boundary value problem (2.45), (2.46), (2.47) for $p_0^+(x,t)$; (ii) use this solution, and the current membrane permeability $k_{\rm m}(x,t)$

and pore radius $a(t)$ as given by (2.48) to solve (2.49) for $n(x,t)$; (iii) update $k_{\mathrm{m}}(x,t)$ and $a(t)$ via (2.48) according to the new $n(x,t)$; and (iv) use the updated $k_{\mathrm{m}}(x,t)$ and return to step (i); repeat.

2.3 Results

The model contains a number of parameters, which are summarized in Table 2.1 (dimensional parameters) and Table 2.2 (dimensionless parameters) along with typical values, where known. Considerable variation in the exact values is possible as indicated in the table, but exhaustive investigation of the effects of each parameter is impractical, hence for most of our simulations, we fix their values as discussed below.

Table 2.1 Approximate Dimensional Parameter Values [34]

Parameter	**Description**	**Typical Value**
L	Length of the pleat	1.3 cm
H	Support layer thickness	1 mm
D	Membrane thickness	300 μm
A_0	Initial pore radius	2 μm (very variable)
B^{-1}	Characteristic particle size	4 μm (very variable)
E	Adsorption coefficient within pores	Unknown (depends on characteristics of membrane and feed solution)
G_∞	Total particle concentration	Depends on application
N_0	Number of pores per unit area	7×10^{10} m^{-2} (very variable)
P_0	Pressure drop	Depends on application
K_{av}	Average support layer permeability	10^{-11} m^2 (very variable)
K_{m0}	Clean membrane permeability	5×10^{-13} m^2 (very variable)

Table 2.2 Approximate Dimensionless Parameter Values

Parameter	**Formula**	**Typical value**
ϵ	H/L	0.077
δ	D/H	0.3
β	$(8\mu ED)/(\pi A_0^5 P_0 G_\infty)$	Unknown; values in range 0.001–0.1 used
Γ	$K_{\mathrm{m0}} L^2/(K_{\mathrm{av}} HD)$	1–50
b	BA_0	0.2–10
ρ_{b}	Additional constant resistance when pore blocked.	Unknown; values in range 0.25–10 used

The relative measure of the resistance of the packing material to that of the membrane, Γ, could certainly vary quite widely from one system to another depending on the detailed structure of the filter membrane and the support layers. Our analysis assumes $\Gamma = O(1)$, which appears to be in line with data for real pleated filters [34]. Based on the values given in Tables 2.1 and 2.2 we take $\Gamma = 10$ throughout most of our simulations (Figures 2.4–2.6), but consider how results depend on Γ in Figure 2.7. The dimensionless pore shrinkage rate, β, is unknown but will be small (this represents the timescale on which pores close due to adsorption, relative to that on which particles block individual pores from upstream): we set $\beta = 0.02$. Assuming the characteristic particle size to be larger than the membrane pore size, we set b, the ratio of initial pore size to characteristic particle size, to 0.5 for most simulations. Finally, assuming that blocking of a pore by a particle increases its resistance by some $O(1)$ factor, we set $\rho_{\mathrm{b}} = 2$ for most simulations. We briefly demonstrate the effect of changing parameters ρ_{b} and b in Figure 2.6.

For the support layer permeability function $k(x)$, we investigate several different profiles to see how this affects the outcome. For a real pleated filter, we anticipate that decreasing support layer permeability will be the more realistic scenario, since the annular cartridge leads to higher compression (and lower permeability) of the layers at the inner cartridge boundary (corresponding to $x = 1$; we refer the reader back to Figures 2.2 and 2.3 for the cartridge geometry). However, for a more complete investigation, and to gain further insight into the model behavior, we also consider increasing support permeability profiles, and the case of uniform support permeability. The different profiles considered are:

$$k(x) = \begin{cases} k_1(x) = 1 & \text{uniform} \\ k_2(x) = 1.5 - x & \text{linear decreasing} \\ k_3(x) = \frac{1}{1.2}\left(\tanh\left(\frac{0.5-x}{0.25}\right) + 1.2\right) & \text{abruptly decreasing} \\ k_4(x) = 0.5 + x & \text{linear increasing} \\ k_5(x) = \frac{1}{1.2}\left(\tanh\left(\frac{x-0.5}{0.25}\right) + 1.2\right) & \text{abruptly increasing} \end{cases} \tag{2.50}$$

(note that each of these support permeability profiles averages to 1, in line with the nondimensionalization chosen for $k(x)$).

We solve the model numerically for each chosen permeability profile, until the membrane becomes impermeable and the total flux through it falls to zero at final time $t = t_f$: for each simulation considered here the flux falls to zero by virtue of the pore radius $a \to 0$ and hence $t_f = 1/\beta = 50$ (see equation (2.48)). Our numerical scheme is straightforward, based on second-order accurate finite difference spatial discretization of the equations, with a simple explicit time step in the pore-blocking equation (2.49). Figure 2.4(a) shows the streamlines, obtained by plotting the level curves of $\psi^{\pm}(x, y)$ defined in (2.43), within the support layers at $t = 0.2t_f$ for the case of uniform support layer permeability k_1; since the streamlines appear qualitatively similar for the other cases k_2 through k_5 we do not show streamlines for all cases. Figures 2.4(b)-(f) show the evolution of the membrane permeability $k_{\mathrm{m}}(x, t)$ until it

falls to zero, for each support permeability profile k_1 to k_5 in (2.50). We also (below) compare results for our pleated filter model with the closest equivalent non-pleated membrane (a flat membrane, surrounded by the same porous support layers as the pleated filter, but in dead-end filtration; see Appendix A for the solution of this problem).

Figures 2.4(a) and 2.4(b) show the results for the case of uniform support layer permeability (USP), $k_1(x) = 1$. Here the fouling profile remains symmetric about the centerline $x = 0.5$, but is distinctly nonuniform in x. Fouling occurs preferentially at the edges of the domain, near the pleat valleys and tips. Since the pore-clogging (adsorption) mechanism is assumed to operate homogeneously throughout the membrane, this enhanced edge-fouling can be due only to greater pore-blocking there, which itself is a consequence of enhanced flux through the membrane in those regions (evidenced by the streamline pattern).

Figures 2.4(c) and 2.4(d) show results for decreasing support layer permeability (DSP) profiles. In both cases, the symmetry is now broken; the highest flow rate, and the fouling, are skewed towards the right-hand boundary $x = 1$ where support permeability is lowest. Compared with the previous USP case, the support permeability is higher where the flow enters. Hence, compared with USP, the flow has an easier path through the support layer, and a greater proportion of the flow entering will pass along the support layer in the x-direction, rather than through the membrane. Both Figures show this same trend, but the effect is more dramatic in Figure 2.4(d), where the support permeability spatial profile is more extreme (and hence the support permeability at entry is higher).

As we would anticipate, the converse trend is seen for the increasing support layer permeability (ISP) profiles (Figures 2.4(e) and 2.4(f)). Here, the fluid has an initially difficult path through the upper support layer parallel to the membrane. Thus initially (again relative to the USP case) a greater proportion of fluid prefers to

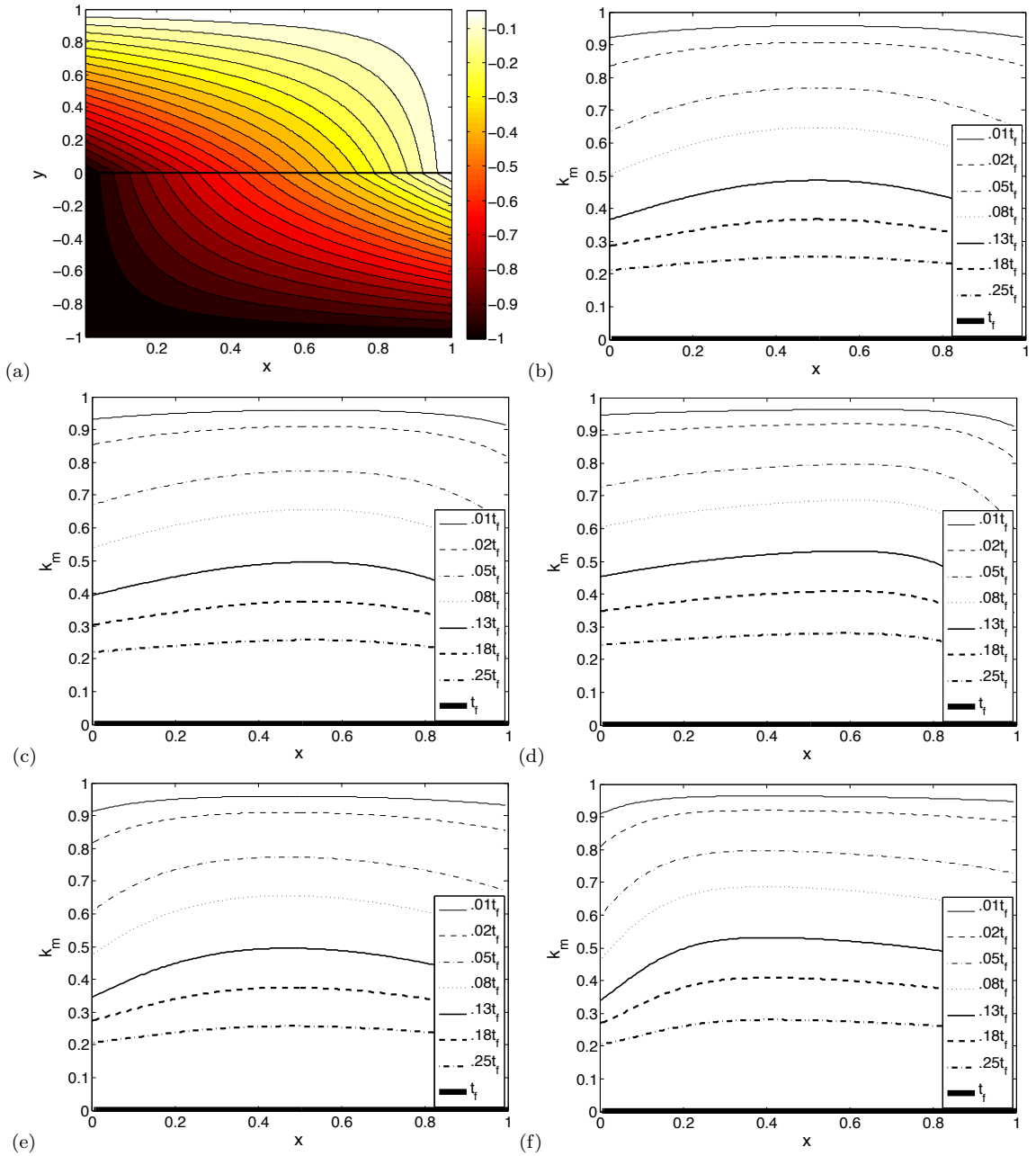

Figure 2.4 (a) The streamlines (level curves of $\psi^{\pm}(x, y)$) at time $t = 0.2t_f$ for the case of uniform support layer permeability $k(x) = k_1(x) = 1$. (b)-(f): Membrane permeability $k_{\rm m}$ at several different times (indicated in the legends) for the support permeability profiles k_1–k_5 (defined in (2.50)), respectively. In all cases, $t_f = 50$. Other parameter values are: $\beta = 0.02$, $\Gamma = 10$, $b = 0.5$, $\rho_{\rm b} = 2$.

flow through the membrane near the boundary $x = 0$, rather than along the support layer in the x-direction. This leads to a greater flux through the $x = 0$ end of the membrane, with greater particle deposition in that region, giving decreased membrane permeability there as time increases.

In all cases, however, as $t \to t_f$ the membrane permeability necessarily becomes uniform again. The explanation for this is straightforward: if $k_{\mathrm{m}} \to 0$ in one area of the membrane then that part is impermeable, and fluid must pass through other parts of the membrane, fouling those until $k_{\mathrm{m}} = 0$ over the whole membrane.

We remark that the fouling patterns obtained here, with increased fouling in the neighbourhood of pleat valleys and tips, appear qualitatively consistent with the experimental data of [19] on the deposition of dust particles within a pleated filter. It is also of interest to note that the fouling patterns we find (due to adsorption and pore-blocking) are quite different in nature to those obtained by [33], who model only cake formation on a pleated filter (and in the absence of any permeable support layers). This suggests that the type of fouling can significantly affect how the filtration proceeds, and hence, it is important to know which fouling modes are operational at all stages. Our model is relevant to the many applications in which cake formation occurs only in the very late stages, when the filter is already heavily fouled, and is near the end of its useful life.

To gain insight into the performance of the filter membrane, we plot the graphs of total flux ($q(t)$, defined by (2.35)) versus throughput (defined by $\int_0^t q(t')dt'$). In order to present results that are readily distinguished from one another, and to focus attention to problems of most immediate industrial relevance, we plot these graphs for simulations corresponding to the uniform and decreasing support permeabilities k_1, k_2, k_3 in (2.50) (note also that, given the symmetries observed in Figure 2.4 we anticipate results for k_2 and k_4 to be identical, and results for k_3 and k_5 to be identical). This flux-throughput graph is a commonly-used tool in the filtration literature to

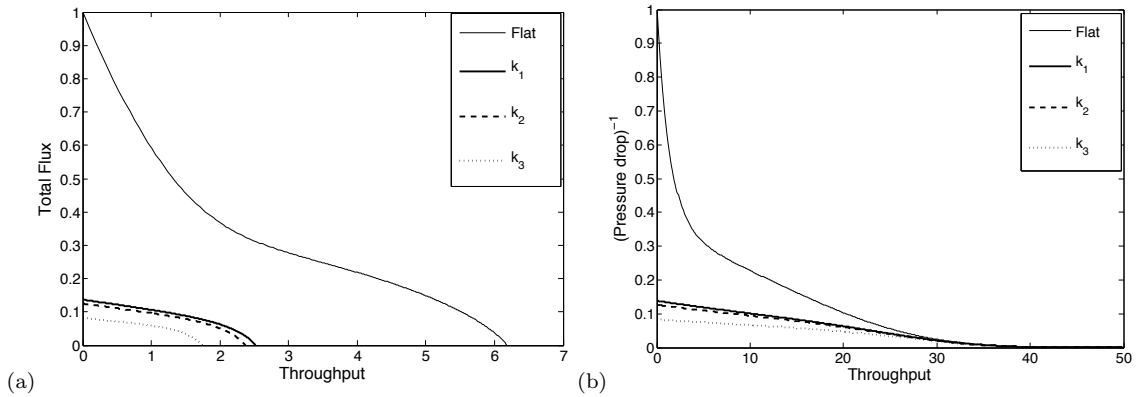

Figure 2.5 (a) Total flux $q(t)$ versus throughput $\int_0^t q(t')dt'$ with imposed constant pressure drop for the pleated membrane with support permeabilities k_1, k_2, k_3 (defined in (2.50)), and for the non-pleated membrane solution of Appendix A (labeled 'Flat' in the legend). (b) Scaled inverse pressure drop versus throughput $\int_0^t q(t')dt'$ for the case of imposed constant total flux, for the pleated membrane with support permeabilities k_1, k_2, k_3 and for the non-pleated membrane solution. Parameter values in both cases are set to the "default" values: $\beta = 0.02$, $\Gamma = 10$, $b = 0.5$, $\rho_b = 2$.

characterize experimentally the performance of filter membranes (see, e.g. [17, 21, 51] among many others). Such curves exemplify the tradeoffs often inherent in membrane performance: high total throughput over a filter lifetime may only be obtained at the expense of low flux (meaning that filtration is slow); or flux may be high over the filter lifetime, but total throughput low (meaning that the filter has a short lifespan). Both scenarios are costly in different ways, and usually in practice some compromise between the two is found.

The results for our pleated filter model are shown in Figure 2.5(a), alongside the corresponding graph for the equivalent non-pleated membrane filter (the solution for which is outlined in Appendix A). The graphs clearly demonstrate the superior performance of the non-pleated membrane, which gives a higher net throughput and higher total flux throughout. Figure 2.5(b) shows results for the case in which total flux through the system, rather than pressure drop across it, is prescribed. In this case, as the membrane is fouled the pressure drop required to maintain the constant flux rises in time, and we demonstrate this by plotting the inverse pressure drop

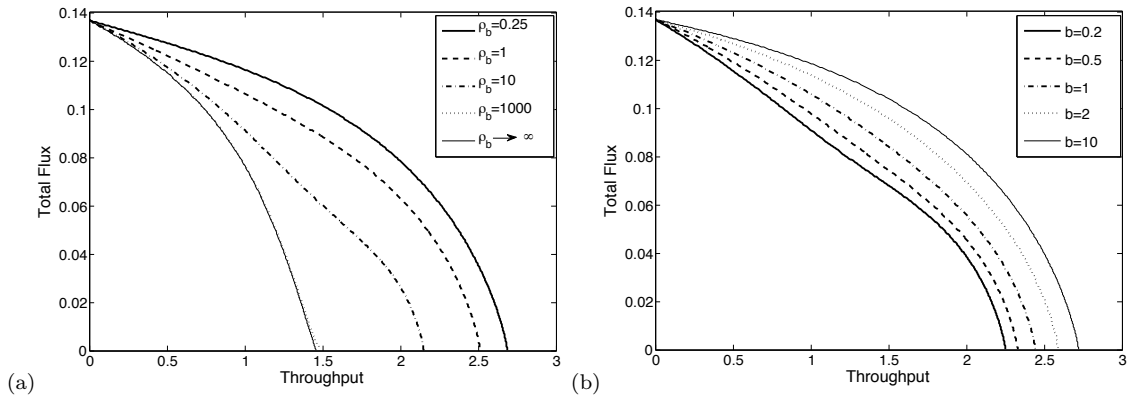

Figure 2.6 Flux-throughput graphs for the uniform support layer permeability $k = k_1 = 1$ (a) for several different values of ρ_b (a measure of the relative increase in pore resistance when a pore is blocked by a large particle), with $b = 0.5$; and (b) for several different values of b, with $\rho_b = 5$. Other parameter values are $\beta = 0.02$, $\Gamma = 10$.

across the system as a function of throughput. The same cases as for Figure 2.5(a) are shown, and once again the superior performance of the equivalent non-pleated filter is apparent: comparing this filter with any of our pleated simulations, the same throughput is achieved at lower pressure drop during the later stages of filtration when blocking becomes significant. The lower pressure drop required for the same throughput is clearly a more efficient scenario, requiring less power to carry out the filtration.

Figure 2.6 briefly demonstrates the effect of varying the parameters ρ_b and b, which measure (respectively) the relative increase in pore resistance when a pore is blocked, and the relative sizes of pores and particles. These results reveal that the pleated filter model retains features qualitatively similar to those observed for "dead end" filtration models (for non-pleated filters). In particular, as ρ_b varies from large to small there is a clear qualitative change in the shape of the flux-throughput performance curves, as the model transitions from blocking-dominated to adsorption-dominated behavior (Figure 2.6(a); this figure also includes the limit $\rho_b \to \infty$, which represents the case in which deposition of a large particle over a pore blocks it entirely). Such qualitative changes have been observed experimentally as the

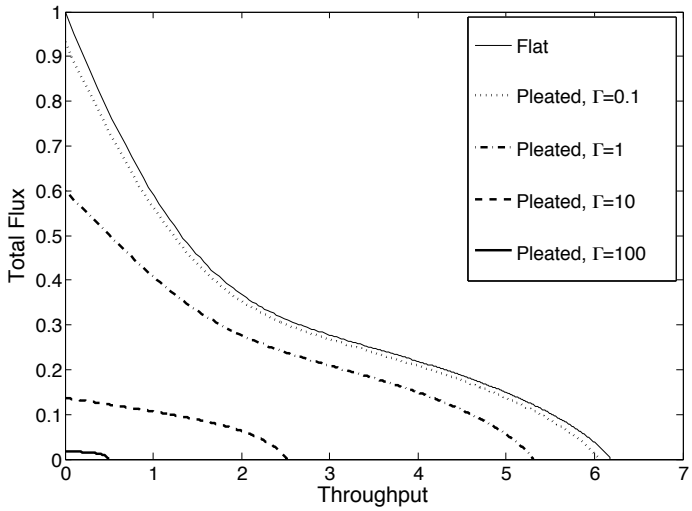

Figure 2.7 Flux-throughput graphs for the uniform support layer permeability $k = k_1 = 1$ for several different values of Γ, with $\beta = 0.02$, $b = 0.5$, $\rho_b = 2$.

membrane type and/or filtrate is varied, see e.g. [21]. Similar qualitative changes are observed as the parameter b is varied (Figure 2.6(b)). Again, this may be attributed to the model transitioning from blocking-dominated (small b; pores smaller than particles) to adsorption-dominated (large b; particles smaller than pores) behavior. Figure 2.6 demonstrates how the flux-throughput graph varies as b is changed for $\rho_b = 5$ (other parameters as before). When a smaller value of ρ_b is used (e.g. $\rho_b = 0.25$), there is less variation in the flux-throughput graphs with b.

Since other parameters remained constant for these simulations of Figure 2.6, overall filter performance deteriorates as ρ_b increases (larger ρ_b means that blocking of individual pores by large particles leads to a greater decrease in system permeability); nonetheless there is a clear and distinct change in the shape of the flux-throughput curves as ρ_b changes, and this is in line with what would be anticipated from the empirical laws commonly assumed in the filtration fouling literature (as described, e.g., by [21]). Similar inferences may be made for the variations with b.

Figure 2.7 shows how the results change as the parameter Γ varies. In line with the asymptotic small-Γ results of Section 2.2.3, we observe convergence of the pleated

filter results to the non-pleated (flat) filter as $\Gamma \to 0$ and the membrane resistance is the dominant contribution to the total system resistance. For very large values of Γ, the support layer adds very significant additional resistance to the system, and overall filter performance is very poor.

2.4 Discussion and Conclusions

We have presented an asymptotically-reduced, first-principles model, that can describe the key features of flow through and fouling of a pleated membrane filter. Our model accounts for the nonuniform flow induced by the pleated geometry, and for fouling by two distinct mechanisms: adsorption and pore-blocking. While essentially predictive, our model contains several parameters that may be difficult to measure for a given system (most notably, the relative importance of blocking to adsorption, ρ_{b}, and the dimensionless adsorption rate, β). In practice, such parameters could be inferred by fitting to a reliable dataset; but even so these parameters will vary from one membrane-filtrate system to another, since they depend on membrane structure, and the chemical interactions between the filtrate particles and the membrane material. In the absence of definitive data, for our simulations we chose what we believe to be plausible parameter values (summarized at the start of Section 2.3 and in Tables 2.1 and 2.2).

The focus in this chapter is on development of a model that can be used to quantify (i) the performance of a pleated filter with known characteristics under given operating conditions, and (ii) the key differences between this and the closest equivalent non-pleated membrane filter in dead-end filtration. There are many different metrics that can be used to quantify filter performance: we focus primarily on optimization of filtrate throughput over the filter lifetime, for fixed filter-membrane characteristics. Though particle capture efficiency is obviously another important performance indicator, we assume that the same filter membrane will do an equally

good (or bad) job of this whether in a pleated or flat configuration, and instead try to elucidate how results depend on cartridge design, and why the comparable unpleated case performs better. We present selected results that bear out the expected performance discrepancy, but we do not, in this part, investigate exhaustively how this discrepancy depends on all model parameters.

One of the suggested hypotheses for the underperformance of pleated filters relative to non-pleated filters is that the presence of the porous support layers in the pleated filter cartridges could be key, due to the increased system resistance they impart. In making our comparisons, we therefore compared our model to a non-pleated filter surrounded by support layers with the same dimensions and permeability as those in our pleated filter (see Appendix A below). A critical performance parameter in our models turns out to be $\Gamma = K_{\mathrm{m0}}L^2/(K_{\mathrm{av}}HD)$ (see Tables 2.1 and 2.2), a scaled dimensionless measure of the ratio of the membrane resistance and the support layer resistance. Recalling the brief analysis of the small-Γ limit presented in Section 2.2.3, we note that this case corresponds, at leading order, to the non-pleated membrane solution. As can be seen from Figure 2.7, the performance of the membrane approaches that of the flat membrane as $\Gamma \to 0$ and furthermore, this is the optimal value of Γ in the sense that it maximizes throughput before the membrane becomes completely fouled. In light of this observation, we briefly consider what steps might be taken to reduce Γ. These could include reducing the length L of the pleat, or increasing the thickness H of the support layer, but both of these act counter to the goal of pleating the membrane in the first place, which is to pack a large amount of membrane into a compact device of small volume. The only realistic way of reducing Γ is therefore to increase the average permeability K_{av} of the surrounding support layers.

Our model can account for spatial variations in permeability of the support layers, which may be present due to the annular geometry of the filter casing, or

could be introduced by choice of support material. These permeabilities were assumed symmetric about the membrane (though the model could be easily adapted to describe the situation when this is not the case); and we investigated primarily how filtration performance varies as this support permeability profile varies with distance x along the pleat. Our results indicate firstly that such variations in support permeability can lead to different fouling patterns within the membrane, at least at intermediate filter lifetimes. More importantly, if variations in support permeability are sufficiently abrupt, they can give rise to a marked decrease in filter performance, as borne out by Figure 2.5(a). It was also noted, however, that variations of support permeability in the y-direction perpendicular to the membrane may be described within the basic modelling framework, provided only that the support permeability is averaged in the y-direction (see (2.30)). This observation suggests that a smaller value of Γ could be obtained simply by adding an additional layer of highly permeable material (*e.g.* mesh, as seen in Figure 2.1) to the existing support, which would increase K_{av} and hence decrease Γ, with an accompanying performance improvement.

The consistency of our results with previous models and literature gives us confidence that our model, based as it is on first principles assumptions about how fouling occurs, is sound, and provides a good basis for predictive simulations. While a more complicated model could provide more accurate predictions, our model has the advantage that it is simple and quick to simulate, offering a useful tool for investigating filter design characteristics.

CHAPTER 3

FLOW AND FOULING IN MEMBRANE FILTERS : EFFECTS OF MEMBRANE MORPHOLOGY

3.1 Introduction

Membrane filters are used in a wide variety of applications to remove particles and undesired impurities of a certain size range from a fluid. Membrane filtration is used in applications as diverse as water purification [30], treatment of radioactive sludge [17], various purification processes in the biotech industry [6, 7, 27, 28], the cleaning of air or other gases [10], and beer clarification [51]. Membrane filters also service the biotech industry in many ways [6, 7, 27, 28]; for example, they are used in artificial kidneys to remove toxic substances by hemodialysis; and as an artificial lung for a bubble-free supply of oxygen in the blood [47]. The type of membrane used depends on the specific application, but an overarching requirement is to have fine control over particle removal from the feed solution, while keeping energy requirements to a minimum. Membrane filters used in microfiltration can have rather varied structure (see, *e.g.,* Figure 3.1), but may generally be understood to be porous media, with characteristic pore size, shape, and void fraction determined by the manufacturer. Separation of particles from the feed solution may occur in two basic ways: (i) particles larger than pores cannot pass through pores and hence are *sieved* out; and (ii) particles smaller than pores may be *adsorbed* within pores and retained within the membrane. With this in mind, the issue of energy requirements for filtration may be understood: a membrane with tiny pores guarantees removal of all particles suspended in the feed solution (by sieving), but provides extremely high resistance to flow, so that a very large pressure drop is required to filter the fluid within a reasonable time frame. In practice therefore, it is desirable that adsorption be responsible for a significant

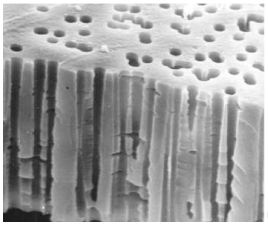
(a)
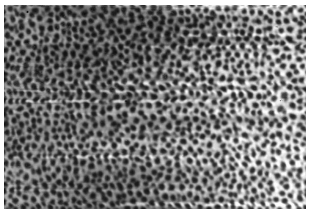
(b)
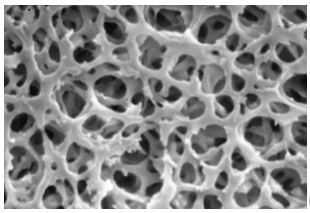
(c)

Figure 3.1 Magnified membranes with various pore distributions and sizes. Photographs (b) and (c) have width 10 μm. *Source: (a) is from [4], (b) and (c) are from [27].*

proportion of the filtration, so that membranes with larger pores operating at lower pressures can be used.

In addition, the system resistance changes significantly during the course of filtration, as the pores of the membrane become fouled with impurities, which are carried by the flow. As discussed before, filter performance thus ultimately deteriorates, via a combination of mechanisms (alluded to above): (i) Particles larger than the pores cannot pass through the membrane. Assuming that such particles follow streamlines (advection-dominated flow with large particle Péclet number), they will be deposited on top of pores, blocking them. (ii) Particles smaller than the membrane pore size are deposited (or adsorbed) within the pores, shrinking the pore diameter and increasing membrane resistance. (iii) Once pores are blocked, other particles can form a *cake* on top of the membrane, adding additional resistance via another porous layer on top. Mathematical models for all three fouling mechanisms have been proposed, based mostly on empirical laws of how membrane resistance relates to total volume of filtrate processed, or net flow-rate through the membrane, in the different fouling regimes (see, for example, [6,17,21,39,51], among many others). In this chapter, we take a different approach, which accounts for the fluid dynamics through idealized pores of specified geometries, and models from first principles the fouling due to adsorption and sieving.

Various models for filtration and fouling, which attempt to address aspects of the effect of the pores' size, geometry and distribution within the membrane, have

been formulated and examined by researchers to date (*e.g.,* [16, 23, 24, 29, 31, 32, 37, 38, 40, 41, 43, 44, 46, 54, 55]). Several models have been proposed for describing the internal stenosis of membrane pores by deposition of small particles (so-called "standard blocking"). Most such models are based on simplifying assumptions such as uniform deposition of particles on pore walls, and round cylindrical pores that traverse the membrane depth. However, as particles deposit on the pore walls, their concentration decreases along the pore depth and therefore the deposition rate, which is necessarily proportional to local particle concentration, decreases as the feed passes towards the pore outlet. In other words, particle deposition is greater at the upstream side of the filter (pore inlet) than at the downstream side (pore outlet). Experimentally, rather steep particle deposition profiles across the depth of the membrane have been observed; see [31] for recent results. To account for such effects, a so called m-model was proposed in [42] and [41], based on the assumption that particles can deposit (uniformly) only over the inlet portion of the pore walls characterized by the parameter m, the ratio of the length of this portion to the whole pore length. This model was further refined in [43] and modified to account for non-uniform deposition of particles within pores. However, this work still assumes an initially uniform pore profile, and takes no account of additional blockage due to sieving of particles larger than pores. Depth-dependent filtration was also considered by [16], using rather different methods to those we use here. These authors use homogenization theory to model a membrane filter as a layered series of spherical obstacles around which the filtered liquid must flow, and which expand as fouling occurs. Griffiths *et al.* [24] also made further contributions to understanding the depth-variation, formulating a discrete "network" model that treats a membrane as a series of layers, each of which contains cylindrical channels that may shrink under the action of adsorption (or be blocked from above by deposition of a large particle).

The goal of the present chapter is to extend the scope of the work outlined above, deriving a continuum model that accounts for membrane internal geometry, and that allows fouling by both particle sieving and particle adsorption to operate simultaneously. We use first-principles modeling to make general predictions about how pore geometry affects filtration performance of a membrane filter. The chapter is laid out as follows: in Section 3.2 we introduce a mathematical model for flow through a single pore of specified geometry. Scenarios where flow is driven by specified pressure drop (Section 3.2.2) and constant flux (Appendix C.1) are considered. Some sample solutions, which demonstrate the features of fouling and separation, are presented in Section 3.3. We also discuss which initial pore profile, in the restricted class of linear pore profiles, gives the best filtration performance (in a sense that we will make precise). Finally, we conclude in Section 3.4 with a discussion of our model and results in the context of real membrane filters.

We acknowledge, of course, that membrane filtration and fouling is a much more complex process than the model assumptions (both of our work and others') allow for. It is clear from Figure 3.1 that many membrane filters are porous media of very complex microstructure, containing many interconnected pores, possibly winding and tortuous, with varying cross-section. Such complexity makes detailed modeling very challenging, We nonetheless believe that reduced models, of the type considered here, can play a valuable role in guiding filter design. We return to this issue in Section 3.3.2 in our discussion of how pore profiles within the membrane might be optimized, and in the Conclusions Section 3.4.

3.2 Darcy Flow Model of Filtration

The modeling throughout this section assumes that the membrane is flat and lies in the (Y, Z)-plane, with unidirectional Darcy flow through the membrane in the positive X-direction (so-called "dead-end" filtration). The membrane properties and

flow are assumed homogeneous in the (Y, Z)-plane, but membrane structure may vary internally in the X-direction (depth-dependent permeability) thus we seek a solution in which properties vary only in X and in time T. Our model may be considered as a representation of the average state (averaged across the (Y, Z)-cross section) of a real membrane in which spatial fluctuations in the plane of the membrane are present. Throughout this section, we use uppercase fonts to denote dimensional quantities; lowercase fonts, introduced subsequently in Section 3.2.2 and Appendix C.1, will be dimensionless.

The superficial Darcy velocity $\mathbf{U} = (U(X,T), 0, 0)$ within the membrane is given in terms of the pressure P by

$$U = -\frac{K(X,T)}{\mu}\frac{\partial P}{\partial X}, \quad \frac{\partial}{\partial X}\big(K(X,T)\frac{\partial P}{\partial X}\big) = 0, \quad 0 \le X \le D, \tag{3.1}$$

where $K(X,T)$ is the membrane permeability at depth X. We consider two driving mechanisms: (i) constant pressure drop across the membrane specified; and (ii) constant flux through the membrane specified. In the former case, the flux will decrease in time as the membrane becomes fouled; in the latter, the pressure drop required to sustain the constant flux will rise as fouling occurs. We will focus primarily on case (i) in this chapter, and so assume this in the following model description; our simulations for the constant flux scenario shown later require minor modifications to the theory (relegated to an Appendix). With constant pressure drop, the conditions applied at the upstream and downstream membrane surfaces are

$$P(0,T) = P_0, \quad P(D,T) = 0. \tag{3.2}$$

The key modeling challenge lies in linking the permeability $K(X,T)$ to measurable membrane characteristics that evolve in time, in order to obtain a predictive model. In this chapter, we consider a simple model in which the membrane consists of a series of identical axisymmetric pores of variable radius $A(X,T)$, which traverse the entire

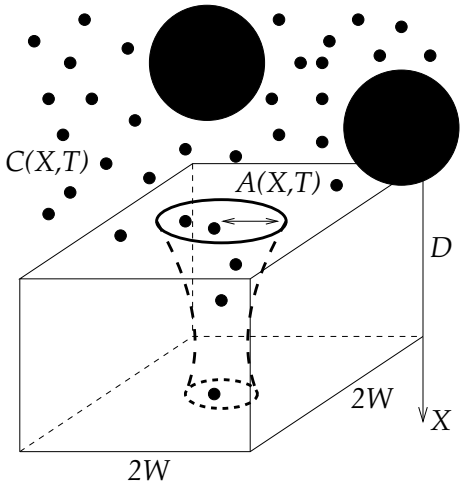

Figure 3.2 Schematic showing the single unit of membrane, assumed repeated in a square lattice. Small particles, at concentration $C(X,T)$, which enter pores and deposit within, are indicated, as are large particles, which block the pore inlet.

membrane. While this may seem a poor approximation to some types of membrane, it is in fact a rather good description of a track-etched membrane filter of the type shown in Figure 3.1(a). We further suppose the pores to be arranged in a square repeating lattice, with period $2W$. The basic setup is schematized in Figure 3.2 (described in more detail below): we consider a feed solution laden with particles, some of which are large and, if larger than the pores, will block them (sieving); and some of which are small, and are transported down the pore and may be deposited on its walls (adsorption, also referred to as "standard blocking" in the literature).

Mass conservation shows that the pore velocity, U_p (the cross-sectionally averaged axial velocity within each pore), satisfies

$$\frac{\partial(\pi A^2 U_\mathrm{p})}{\partial X} = 0, \tag{3.3}$$

while Darcy's law for the averaged superficial velocity U within the pore plus its period-box gives

$$U = -\frac{\phi_\mathrm{m} K_\mathrm{p}(X,T)}{\mu}\frac{\partial P}{\partial X}, \tag{3.4}$$

where $\phi_{\mathrm{m}} = \pi A(X,T)^2/(2W)^2$ is the local membrane porosity at depth X, and $K_{\mathrm{p}}(X,T) = A(X,T)^2/8$ is the local permeability of an isolated pore. The pore and superficial velocities are related by

$$U = \phi_{\mathrm{m}} U_{\mathrm{p}}, \tag{3.5}$$

by a simple flux-balance argument. This flow model is completed by assumptions on how the membrane permeability changes in time due to fouling by particles, discussed below. The key nomenclature used both here and below is summarized for easy reference in Table 3.1.

3.2.1 Fouling Model: Particle Adsorption and Sieving

We consider the effects of fouling by the two primary mechanisms discussed in the Introduction: (i) fouling by pore blocking (sieving of particles too large to pass through membrane pores, which thus deposit on the membrane's upstream surface); and (ii) adsorption of small particles on pore walls. As noted earlier, although cake formation may be an important fouling mechanism in the late stages of the filtration, it is not considered explicitly in this chapter. The "blocking" mechanism that we do model is a necessary preliminary to cake formation, and may be considered as the first step in the caking process. The fouling modeling is similar in spirit to that used in our earlier work on pleated membrane filters [49] (see Chapter 2 as well); however that work focused on the effects of the pleating, and took no account of depth-dependent structure within the membrane (which is the specific focus of the present chapter). To model the two distinct fouling mechanisms, we treat the large blocking and small adsorbing particles as separate populations: a bimodal particle size distribution. The actual dimensions (of both particles and pores) that might be relevant will change from one situation to another, but it is reasonable to think of our "small" particles as having diameter of no more than 0.1 times the pore diameter, while the "large"

particles are around the same diameter as the pore (or larger). We first discuss the pore-blocking mechanism (i).

Fouling by Pore Blocking: As noted above, we assume that pores are slender tubes spanning the membrane, of length D and variable radius $A(X,T)$, arranged in a $2W$-periodic square lattice (see Figure 3.2). Initially all pores have specified radius, $A(X,0) = A_0(X) < W$. Where an individual pore (at time T) is unblocked the total flux through it, $Q_{\mathrm{u,pore}}(T)$, is given (approximately) by

$$Q_{\mathrm{u,pore}} = -\frac{1}{R_{\mathrm{u}}}\frac{\partial P}{\partial X} \quad \text{where} \quad R_{\mathrm{u}} = \frac{8\mu}{\pi A^4}, \tag{3.6}$$

and R_{u} is the pore resistance per unit of the membrane depth. Blocking occurs when a large particle becomes trapped at the entrance to a pore, obstructing the flow. Instead of treating such pores as completely closed, permitting no further flow (as many authors do), we instead assume that the blocking increases the pore's resistance to flow, so that the flux through it is decreased. We model this effect by adding an extra resistance, characterized by the dimensionless parameter ρ_{b}, in series with the resistance R_{u} of the unblocked pore. The flux through a blocked pore, $Q_{\mathrm{b,pore}}(X,T)$, is then given by

$$Q_{\mathrm{b,pore}} = -\frac{1}{R_{\mathrm{b}}}\frac{\partial P}{\partial X} \quad \text{where} \quad R_{\mathrm{b}} = \frac{8\mu}{\pi W^4}\left(\left(\frac{W}{A}\right)^4 + \rho_{\mathrm{b}}\right). \tag{3.7}$$

Here, R_{b} is the resistance per unit length of the blocked pore. The dimensionless parameter ρ_{b} characterizes the tightness of the seal formed when a large particle sits over a pore: for large values of ρ_{b}, pore resistance increases dramatically after blocking (a tight seal, permitting only a small fraction of the original flux through the pore), while for small values resistance is almost unchanged (a poor seal, permitting nearly the same flux as the unblocked pore). We can now relate the number densities of unblocked and blocked pores per unit area, $N(T)$ and $N_0 - N(T)$; respectively

(where $N_0 = N(0)$ and $N_0(2W)^2 = 1$), to the superficial Darcy velocity by noting that the flux of fluid per unit area is

$$N_0(2W)^2 U = N(T)Q_{\mathrm{u,pore}} + (N_0 - N(T))Q_{\mathrm{b,pore}},$$

so that, on substituting for $Q_{\mathrm{u,pore}}$ from (3.6) and for $Q_{\mathrm{b,pore}}$ from (3.7) in the above, we obtain

$$U = -\frac{\pi W^4}{8\mu}\frac{\partial P}{\partial X}\left(\frac{N}{(W/A)^4} + \frac{N_0 - N}{(W/A)^4 + \rho_{\mathrm{b}}}\right), \tag{3.8}$$

an expression in which, comparing with (3.1), the depth-dependent membrane permeability $K(X,T)$ is implicit.

To close the blocking model, we require an equation describing the evolution of $N(T)$, the instantaneous number of unblocked pores. [1] We assume a pore is blocked whenever a particle from the large-particle population, with radius $S > A(0,T)$ is advected to the pore entrance (we assume that large particles follow the streamlines and do not interact with each other). If we assume a cumulative large-particle size distribution function $G(S)$, giving the number of large particles per unit volume of fluid with radius smaller than S, then the concentration of particles of size $S > A(0,T)$ is $G_\infty - G(A)$ (where $G_\infty = \lim_{S\to\infty} G(S)$ is the total large-particle concentration). The probability that a particular pore become blocked (per unit time) is thus $(G_\infty - G(A))$ multiplied by the flux through the pore, $Q_{\mathrm{u,pore}}$:

$$\left[\begin{array}{c}\text{Probability per unit time that}\\ \text{pore of radius } A \text{ is blocked}\end{array}\right] = -\left.\frac{\pi A^4}{8\mu}\frac{\partial P}{\partial X}(G_\infty - G(A))\right|_{X=0}.$$

[1] We use a one-dimensional model in which quantities vary only in the depth of the membrane, X, and time, T, intended to represent a spatial average of a real system in which variation in the plane (Y,Z) of the membrane may be present. A different (much more computationally intensive) approach would be to model individual particles landing on pores at specific (Y,Z) locations, which requires stochastic considerations. Such an approach was used by Griffiths, Kumar & Stewart (2014).

It follows that $N(T)$, the number density of unblocked particles per unit area, evolves according to the equation

$$\frac{\partial N}{\partial T} = N\frac{\pi A^4}{8\mu}\frac{\partial P}{\partial X}(G_\infty - G(A))\bigg|_{X=0}. \tag{3.9}$$

Note that this model predicts that $N \to 0$ as $T \to \infty$, so that eventually all pores will block. This is not unexpected: since blocked pores acquire significant additional resistance, flow will preferentially be diverted to unblocked pores (which admit higher flux), advecting the large blocking particles to those yet-unblocked sites. The model assumes blocking only by large particles, and only at the pore inlet, since terms are evaluated at $X = 0$. Strictly speaking, a pore will be blocked in this way by any particle larger than its narrowest point, so one could argue that the right-hand side should be evaluated at the value $X = X^*(T)$ where $A(X, T)$ achieves its minimum at each instant. We will see however that, due to the adsorption occurring preferentially at the pore inlet, for all parameter sets we consider, $X^*(T) \to 0$ quite quickly. Therefore, we do not anticipate that results would change significantly if we took careful account of this effect.

Another potential deficiency of this blocking model is that any particles from the "large particle" population that are smaller than the pore inlet will not be captured by the membrane, but simply pass through it. This seems possible for particles with significant inertia passing through a simple, track-etched membrane of the type shown in Figure 3.1 (a) and (b), but for membranes of more complex structure a scenario in which a significant proportion of such "large" particles pass through the membrane is likely both unrealistic and undesirable. For this reason, almost all simulations presented in this chapter are for the case where all large particles are bigger than the initial pore inlet radius, $A(0, 0) = A_0(0)$. In this case, the cumulative large-particle

distribution may be taken as

$$G(S) = \begin{cases} G_\infty & \text{if} \quad S > A_0(0), \\ 0 & \text{if} \quad S \leq A_0(0); \end{cases} \tag{3.10}$$

all particles from this distribution will be sieved by the membrane. For comparison, we will also show some results with an exponential cumulative large-particle distribution of the form

$$G(S) = G_\infty(1 - e^{-BS}), \tag{3.11}$$

where B^{-1} is a characteristic particle size in the feed solution. In this case, some of these "large" particles are smaller than the pore inlet radius; as noted above, such particles will escape capture altogether and simply be advected straight through the pore.

Table 3.1 Key Nomenclature Used in the Model

U	Superficial Darcy velocity	U_p	Pore velocity
K	Membrane permeability	K_p	Permeability of pore
P	Pressure	P_0	Pressure drop across membrane
C	Concentration of small particles	C_0	$C_0 = C(0,T)$, specified
A	Pore radius	A_0	$A_0(X) = A(X,0)$, specified
N	Number of unblocked pores	N_0	Number of pores per unit area
$2W$	Length of the square repeating lattice	D	Membrane thickness
G_∞	Total concentration of large particles	B^{-1}	Characteristic large-particle size
$Q_\mathrm{u,pore}$	Flux through an unblocked pore	$Q_\mathrm{b,pore}$	Flux through a blocked pore
R_u	Unblocked pore resistance	R_b	Blocked pore resistance
Λ	Particle-wall attraction coefficient	α	Pore shrinkage parameter

Fouling by Adsorption: To account also for the effects of membrane fouling by particle adsorption, we must specify how the population of small particles

is deposited within pores. As indicated in Figure 3.2, we consider these small particles independently of the large blocking particles discussed above, and track the concentration, $C(X,T)$, of small particles, averaged over the pore cross-section, as the feed passes down the pore. In general, the small particles are advected and diffuse within the flow [18], and adhere to the wall at a rate proportional to their local concentration. The full advection-diffusion model, with dependence on radial coordinate within the pore as well as axial coordinate X down the pore, is nontrivial, and the details of its analysis are relegated to Appendix B. Here, we present just the result that emerges after an asymptotic analysis based on a distinguished limit of the particle Péclet number, and averaging over the pore cross-section: the averaged concentration $C(X,T)$ of small particles satisfies a simple advection model,

$$U_{\mathrm{P}}\frac{\partial C}{\partial X} = -\Lambda\frac{C}{A}, \tag{3.12}$$

to be solved subject to specified particle concentration at the inlet,

$$C(0,T) = C_0. \tag{3.13}$$

The (dimensional) constant Λ is intended to capture the physics of the attraction between particles and pore wall that leads to deposition. More details are provided in Appendix B, but (3.12) models, in a crude way, effects such as van der Waals' interactions between suspended particles and the membrane material, and attractive forces due to electrostatic charge. Inherent in (3.12) is an assumption that all small particles are identical with regard to their deposition dynamics, which may well not be true in practice. In addition, the model assumes that particle adherence to a clean membrane is the same as for a pre-fouled membrane, again a questionable assumption. Nonetheless, for appropriate choices of parameters, we expect our model to provide a reasonable approximation to a real system with sufficiently homogenous feed solution, and to be quite broadly applicable. The pore radius $A(X,T)$ shrinks in response to

the deposition: we propose

$$\frac{\partial A}{\partial T} = -\Lambda \alpha C, \tag{3.14}$$

for some constant α (related to the particle size), which simply assumes that the pore cross-sectional area shrinks at a rate determined by the total area of particles deposited locally at depth X. The initial pore radius is specified throughout the membrane,

$$A(X, 0) = A_0(X). \tag{3.15}$$

Note that particle deposition in our model is permanent and irreversible. It is possible, however, that in the later stages of filtration, as the pores narrow, shear forces become significant enough to lead to some re-dispersion of particles. Such re-dispersal is beyond the scope of our model, though could be incorporated in a more sophisticated treatment. We observe that purely adsorptive fouling can be retrieved by setting $N \equiv N_0$ in (3.8).

3.2.2 Scaling and Nondimensionalization

When filtration is driven by a constant pressure drop P_0 across the upstream and downstream membrane surfaces, we nondimensionalize the modified Darcy model (3.2), (3.3), (3.5)–(3.15), using the scalings

$$P = P_0 p, \quad X = Dx, \quad C = C_0 c, \quad N = N_0 n, \quad (A, S) = W(a, s), \quad B = \frac{b}{W},$$

$$(U, U_{\mathrm{p}}) = \frac{\pi W^2 P_0}{32 \mu D}(u, u_{\mathrm{p}}), \quad G = G_\infty g(s), \quad T = \frac{8 \mu D}{\pi P_0 W^4 G_\infty} t, \tag{3.16}$$

(time here is nondimensionalized on the blocking timescale), giving the following dimensionless model for $u(x,t)$, $u_{\mathrm{p}}(x,t)$, $p(x,t)$, $a(x,t)$, $c(x,t)$, $n(t)$ (dimensionless Darcy velocity, cross-sectionally averaged pore velocity, pressure, pore radius, cross-sectionally averaged particle concentration, and number density of unblocked pores,

respectively):

$$4u = \pi a^2 u_{\mathrm{p}}, \tag{3.17}$$

$$u = -a^4 \frac{\partial p}{\partial x}\left(\frac{1-n}{1+\rho_{\mathrm{b}} a^4} + n\right), \quad \frac{\partial u}{\partial x} = 0, \tag{3.18}$$

$$u_{\mathrm{p}} \frac{\partial c}{\partial x} = -\hat{\lambda}\frac{c}{a}, \quad \hat{\lambda} = \frac{32\Lambda\mu D^2}{\pi P_0 W^3}, \tag{3.19}$$

$$\frac{\partial a}{\partial t} = -\beta c, \quad \beta = \frac{8\mu D\Lambda\alpha C_0}{\pi P_0 W^5 G_\infty}, \tag{3.20}$$

$$\frac{dn}{dt} = n a^4 \frac{\partial p}{\partial x}(1-g(a))\bigg|_{x=0}, \tag{3.21}$$

with boundary and initial conditions

$$p(0,t) = 1, \quad p(1,t) = 0, \quad c(0,t) = 1, \quad a(x,0) = a_0(x), \quad n(0) = 1. \tag{3.22}$$

Equation (3.18) then gives the pressure p as

$$p = u \int_x^1 \frac{dx'}{a^4(\frac{1-n}{1+\rho_{\mathrm{b}} a^4} + n)}, \tag{3.23}$$

and the superficial Darcy velocity in terms of the pore radius $a(x,t)$ as

$$u = \left(\int_0^1 \frac{dx'}{a^4(\frac{1-n}{1+\rho_{\mathrm{b}} a^4} + n)}\right)^{-1}, \quad \text{hence} \quad u_{\mathrm{p}} = 4\left(\pi a^2 \int_0^1 \frac{dx'}{a^4(\frac{1-n}{1+\rho_{\mathrm{b}} a^4} + n)}\right)^{-1}. \tag{3.24}$$

Substituting in (3.19) and (3.21) our final system reduces to equations (3.24), plus

$$\frac{dn}{dt} = -\, n\left(\int_0^1 \frac{dx'}{a^4(\frac{1-n}{1+\rho_{\mathrm{b}} a^4} + n)}\right)^{-1} \big(\frac{1-n}{1+\rho_{\mathrm{b}} a^4} + n\big)^{-1}(1-g(a))\bigg|_{x=0}, \tag{3.25}$$

$$\frac{\partial c}{\partial x} = -\lambda c a \int_0^1 \frac{dx'}{a^4(\frac{1-n}{1+\rho_{\mathrm{b}} a^4} + n)}, \quad \lambda = \frac{8\Lambda\mu D^2}{P_0 W^3}, \quad \frac{\partial a}{\partial t} = -\beta c, \tag{3.26}$$

with β as defined in (3.20) and initial/boundary conditions

$$n(0) = 1, \quad c(0,t) = 1, \quad a(x,0) = a_0(x) < 1. \tag{3.27}$$

In line with (3.10) and (3.11), the two forms considered for the cumulative particle distribution function $g(s)$ are

$$g(s) = \begin{cases} 1 & \text{if } s > a_0(0), \\ 0 & \text{if } s \leq a_0(0), \end{cases} \tag{3.28}$$

and

$$g(s) = 1 - e^{-bs}, \tag{3.29}$$

where $b = BW$ characterizes the ratio of characteristic membrane pore size to typical particle size. Note that for $g(s)$ as specified in (3.28) particles are larger than pores throughout, and $g(a)|_{x=0} = 0$ in equation (3.25).

3.3 Results

In this section, we present some simulations of the model (3.24)–(3.27) described in Section 3.2 above, paying particular attention to how results depend on the pore geometry. Selected results for the case driven by constant flux, Eqs.(C.3)–(C.5), will be presented later in Appendix C.

Our model contains several dimensionless parameters: λ which captures the physics of the attraction between particles and the pore wall; the ratio ρ_{b} of the additional resistance due to pore-blocking to the original resistance of the unblocked pore; and the dimensionless pore shrinkage rate β. For the case in which we consider a distribution of large particle sizes, with cumulative particle size distribution $g(s)$ specified by (3.29), we also need to specify the ratio b of pore size to characteristic particle size in $g(s)$. The values of each of these dimensionless quantities depend on physical dimensional parameters that must be measured for the particular system under investigation, and we lack such detailed experimental data; hence we have to make our best estimate as to the most appropriate values to use in our simulations. The parameters are summarized in Tables 3.2 (dimensional parameters) and 3.3

(dimensionless parameters) along with typical values, where known. Considerable variation is possible from one system to another, as noted in the Tables; nonetheless we believe that our simulations illustrate the predictive potential of our model if detailed data are available. Most of the parameters in Table 3.2 (such as W, D, B, α, G_∞, N_0, P_0 and C_0) depend on physical characteristics of the filter membrane and the feed fluid, therefore in principle could be measured directly or obtained from the manufacturer. Other parameters are harder to measure directly, but indirect methods can be useful. For example, as noted earlier, the particle-wall attraction coefficient Λ may be estimated by comparing solutions of equation (3.12) to experiments that reveal the density of particles absorbed within the filter (as obtained by, *e.g.,* [31] via fluorescence microscopy); but such experiments are nontrivial. Direct estimation of ρ_b for a real membrane system could be more problematic, but if this is the only model parameter for which no data can be inferred then this may be viewed as an overall fitting parameter.

Given the number of parameters, most of them will be fixed throughout our simulations. The value of the dimensionless attraction coefficient between pore wall and particles, λ, is unknown, and could certainly vary widely from one system to another depending on the detailed structure of the filter membrane and on the nature of the feed solution. In the absence of firm data, we take $\lambda = 2$ for most simulations. The dimensionless pore shrinkage rate, β, is unknown but will normally be small (it represents the timescale on which pores close due to adsorption, relative to that on which particles block individual pores from upstream): we set $\beta = 0.1$. We note here that the parameters λ and β are not independent: if we wish to consider the effect of changing membrane thickness D for example, we must keep $\lambda \propto \beta^2$, while if we wish to investigate the effect of the attraction coefficient Λ, we must keep $\lambda \propto \beta$. We expand upon this point later. In the absence of definitive data on ρ_b, assuming that blocking of a pore by a particle increases its resistance by twice the original

Table 3.2 Dimensional Parameter Values ([21, 34])

Parameter	**Description**	**Typical Value**
$2W$	Length of the square repeating lattice	4.5 μm (very variable)
Λ	Particle-wall attraction coefficient	Unknown (depends on characteristics of membrane and feed solution)
D	Membrane thickness	300 μm
A_0	Initial pore radius	2 μm (very variable)
B^{-1}	Characteristic large-particle size for the inhomogeneous particle size distribution (3.11)	4 μm (very variable)
α	Pore shrinkage parameter (see (3.14)) related to particle size	Unknown (depends on characteristics of feed solution)
G_∞	Total concentration of large particles	Depends on application
N_0	Number of pores per unit area	7×10^{10} m^{-2} (very variable)
P_0	Pressure drop	Depends on application 10–100 K Pa used here
Q_{pore}	Flux through a single pore	Depends on application
C_0	Total concentration of small particles in feed solution	Depends on application

resistance of the unblocked pore, we set $\rho_{\text{b}} = 2$ for most simulations. Finally, for those simulations where we allow an exponential distribution of large particle sizes, with $g(s) = 1 - e^{-bs}$ (see equations (3.11) and (3.29)), we consider values of b in the range 0.2 to 10. We briefly demonstrate the effect of changing certain key parameters in Figures 3.4 and 3.5.

As noted in the Introduction Section 3.1, most prior work considers a uniform initial pore profile. While we cannot consider all possible initial pore profiles, we present results for a selection of profiles that allow us to model uniform, increasing, decreasing and non-monotone membrane resistances, as functions of depth. According

Table 3.3 Dimensionless Parameters and Approximate Values

Parameter	**Formula & description**	**Typical value**
λ	$(8\Lambda\mu D^2)/(P_0W^3)$	Unknown; values in
	Dimensionless particle-wall attraction coefficient	range 0.1–10 used
ϕ	$\pi/(4W^2D)\int_0^D A(X,0)^2dX$	Typically $0.5-0.7$,
	Initial average porosity (void fraction)	here values in range
		$0.25-0.75$ used
β	$(8\mu D\Lambda\alpha C_0)/(\pi P_0W^5G_\infty)$	Unknown; values in
	Adsorption rate coefficient	range 0.001–0.2 used
b	BW	0.2–10
	Large-particle size (for inhomogeneous particle size	
	distribution (3.11))	
ρ_{b}	Additional constant resistance when pore blocked	Unknown; values in
		range 0–10 used

to the Darcy model, the local membrane resistance is proportional to $A(X,0)^{-4}$. Using the nondimensionalization of (3.16), one can define a dimensionless averaged membrane resistance, $r(t)$, as

$$r(t)=\int_0^1 \frac{dx}{a(x,t)^4}. \tag{3.30}$$

In order to make a meaningful comparison, we run simulations for pore shapes that give the same initial membrane resistance $r_0 = r(0)$. This means that we are comparing membranes that perform identically when no fouling occurs – they would give identical throughputs when filtering pure water under the same applied pressure

drop. The pore profiles considered are:

$$a(x,0) = \begin{cases} a_1(x,0) = 0.904 & \text{uniform initial pore profile,} \\ a_2(x,0) = 0.16x + 0.83 & \text{linear increasing initial pore profile,} \\ a_3(x,0) = 0.99 - 0.16x & \text{linear decreasing initial pore profile,} \\ a_4(x,0) = 0.874 + 0.39(x-0.5)^2 & \text{convex parabolic initial pore profile,} \\ a_5(x,0) = 0.933 - 0.33(x-0.5)^2 & \text{concave parabolic initial pore profile,} \end{cases} \tag{3.31}$$

all of which correspond to the same initial membrane resistance $r_0 = 1.50$. We note that these initial profiles also happen to have very similar average porosity or void fraction, $\phi_0 = (\pi/4)\int_0^1 a(x,0)^2 dx$ (though this would not be true of all equal-resistance membranes): $\phi_0 = 0.64$ for a_1 and a_5, and $\phi_0 = 0.65$ for a_2, a_3 and a_4. Three of the profiles (a_1, a_4 and a_5) are initially symmetric about the membrane centerline, but we will see that in all cases asymmetry rapidly develops due to the particle adsorption within pores.

We solve the model numerically for each chosen pore profile, until the membrane becomes impermeable and the total flux through it falls to zero at final time $t = t_\mathrm{f}$ (when the pore radius $a \to 0$). Our numerical scheme is straightforward, based on first-order accurate finite difference spatial discretization of the equations, with a simple implicit time step in the pore-blocking equation (3.20) and trapezoidal quadrature to find the integrals in equation (3.24).

3.3.1 Model Simulations

We present results for the model summarized in Section 3.2.2 according to the scenarios discussed above. The main results are shown in Figure 3.3: we simulate the model for each of the initial profiles given in (3.31), with parameters $\lambda = 2$ and $\rho_\mathrm{b} = 2$ characterizing the effects of fouling by adsorption and pore-blocking (sieving). Figure 3.3(a) shows the cross-sectionally averaged pore velocity u_p for the

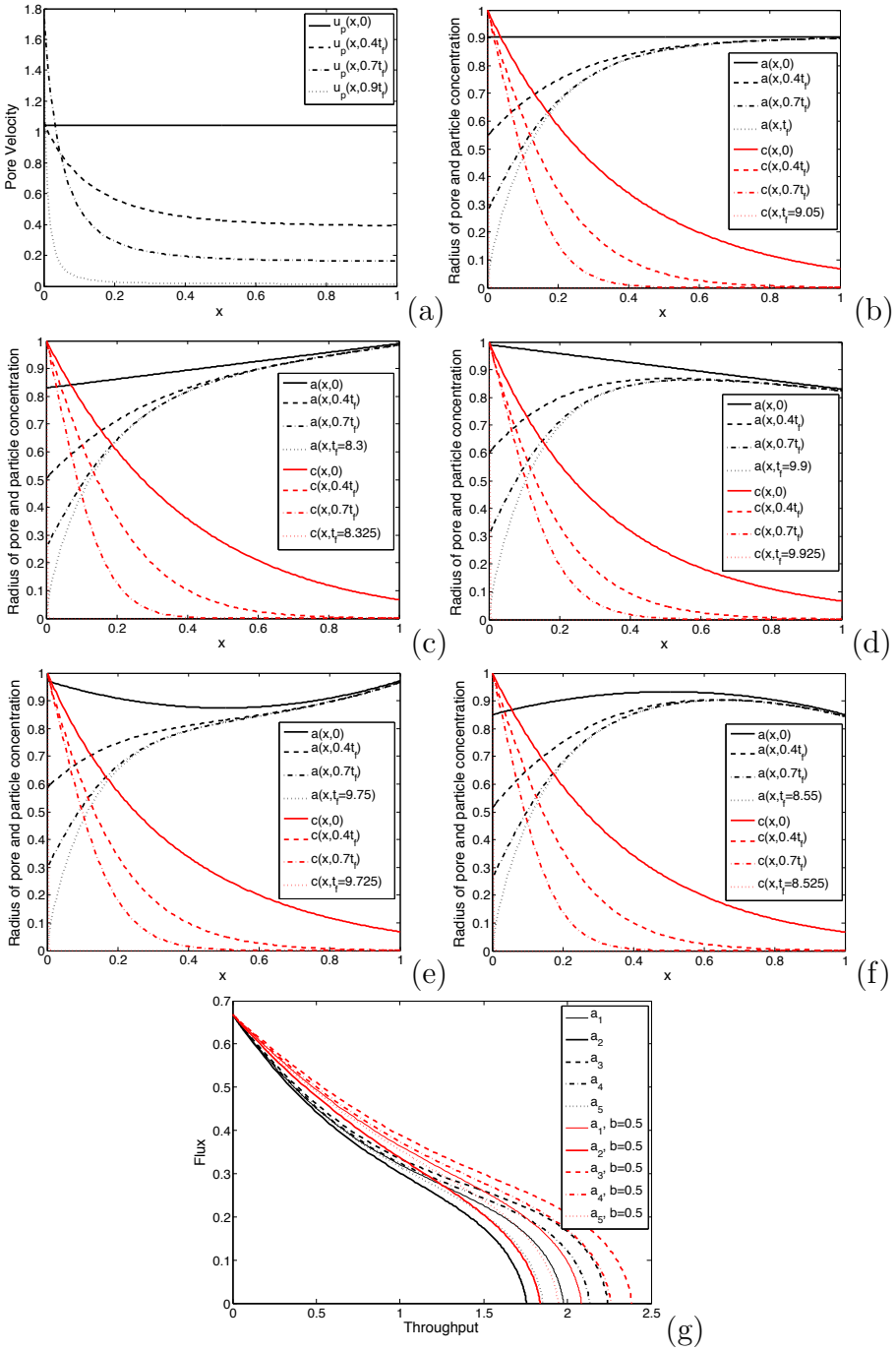

Figure 3.3 Filtration simulations: (a) The cross-sectionally averaged pore velocity $u_{\rm p}$ with uniform initial pore profile $a_1(x,0) = 0.904$; (b)-(f) the pore radius and particle concentration at selected times up to the final blocking time ($t_{\rm f}$, indicated in the legends) for different initial pore radius profiles: (b) $a_1(x,0) = 0.904$, (c) $a_2(x,0) = 0.16x + 0.83$, (d) $a_3(x,0) = 0.99 - 0.16x$, (e) $a_4(x,0) = 0.874 + .39(x-0.5)^2$, (f) $a_5(x,0) = 0.933 - 0.33(x-0.5)^2$; (g) total flux vs throughput for these initial profiles for homogeneous ((3.28), black curves) and exponential ((3.29), red curves) distributions of large particles, with $\lambda = 2$, $\beta = 0.1$, $\rho_{\rm b} = 2$ and $b = 0.5$.

initially uniform pore profile, and Figures 3.3(b)-(f) show the pore radius $a(x,t)$ and the concentration of small particles $c(x,t)$ for each of the five different initial pore profiles, at various times throughout the evolution. Other parameter values are given in the figure caption. The cumulative large-particle size distribution function is as given in (3.28), so that all of the large particles in the feed are bigger than the pore inlet size and are therefore sieved out. A striking feature of these plots is that pore closure (accompanied by cessation of filtration) occurs first at the upstream membrane surface, even for pores that are initially widest on that side. This is consistent with the graph of the pore velocity u_{p} (Figure 3.3(a)), which is initially uniform (for the initially uniform channel) but rapidly becomes nonuniform, becoming much higher at the narrowing pore inlet; and also with the particle concentration graphs, which show that most of the particle deposition occurs at the pore inlet. This effect becomes more pronounced at later times as the pore radius shrinks near the inlet, further enhancing the deposition there. The graphs of $c(x,t)$ in Figure 3.3(b)-(f) demonstrate that the filter membranes are initially capturing more than 90% of small particles (by adsorption) in all cases, with this proportion increasing to nearly 100% at later times. The capture proportion could be adjusted by varying the parameter λ: increasing (decreasing) λ will increase (decrease) the proportion of particles captured. The effect of λ is discussed further below.

As mentioned earlier, a common experimental characterization of membrane filtration performance is the graph of total flux through the membrane at any given time versus the total volume of filtrate processed at that time (throughput); the so-called flux–throughput graph for the membrane. Since the flux is directly proportional to the averaged Darcy velocity, we define our dimensionless flux by $q(t) = u(0,t)$; throughput is then defined by $\int_0^t q(t')dt'$. We plot these curves, for each of the five pore profiles considered, in Figure 3.3(g). This plot also shows the equivalent flux-throughput graphs for the exponential large-particle distribution

function of (3.29), for comparison with the homogeneous case (3.28). The graphs collectively demonstrate that, although all pore profiles give the same initial average membrane resistance (and, to a good approximation, the same initial porosity or void fraction), they exhibit significant differences in performance over time. In particular, membranes whose pores are widest on the upstream side give notably better performance overall according to this performance measure, with more filtrate processed under the same conditions. The membrane with least total throughput is that whose pores are initially narrowest on the upstream side, exhibiting rapid pore closure (pore profile $a_2(x)$ in (3.31)). Furthermore, we see that the flux-throughput curves are initially concave, becoming convex only as total system blockage is approached. This change in curvature has been observed in experimental systems (*e.g.,* [21]) but rarely in model simulations: it seems that only models that incorporate multiple blocking mechanisms simultaneously can exhibit such behavior. It appears to be indicative of the different blocking regimes: in the early stages the pore-blocking is the dominant mechanism responsible for the decrease in flux, while in the latter stages adsorptive blocking dominates (at least for the choice of parameters used here). The differences in performance noted here for homogeneous (3.28) and exponential (3.29) distributions of large-particle sizes are in part due to the fact that for the homogeneous distribution all large particles are sieved, while in the exponential case some are smaller than the pore and pass through the membrane. System resistance therefore increases more rapidly in the former case.

Figure 3.4(a) demonstrates the effect of varying the parameter ρ_{b}, which measures the relative increase in pore resistance when a pore is blocked by a large particle. All of these simulations are performed for the homogeneous large-particle size distribution (3.28). We note that as ρ_{b} varies from large to small there is a clear qualitative change in the shape of the flux–throughput performance curves, as the model transitions from blocking-dominated to adsorption-dominated. A large value of

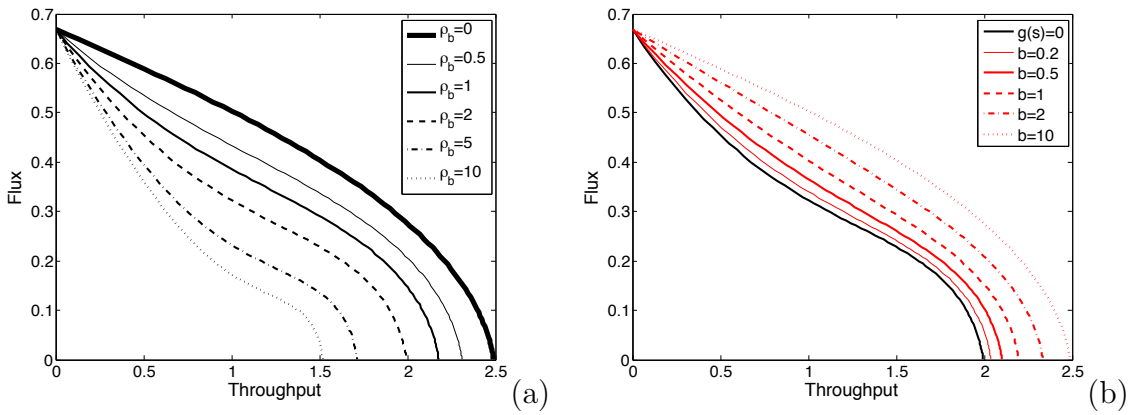

Figure 3.4 Flux-throughput graphs for the uniform initial pore profile $a_1(x,0) = 0.904$, with $\lambda = 2$ and $\beta = 0.1$, (a) for several different values of ρ_b (relative increase in pore resistance when blocked by a large particle) with homogeneous particle size distribution $g(s)$ given by (3.28); and (b) for both homogenous large-particle distribution (3.28), and for several non-homogeneous particle distributions given by (3.29) with different values of b (a measure of the relative sizes of pores and particles), with $\rho_b = 2$.

ρ_b means that blocking of a pore by a large particle leads to a tight seal at the inlet and a significant increase in resistance (blocking-dominated); while a small value means that a blocked pore is very loosely sealed, and offers only marginally more resistance to flow than an unblocked pore (hence fouling will be adsorption-dominated). Again, see the experimental data in, *e.g.,* [21], which reveal similar features as the membrane type and/or filtrate is varied. Since increasing the value of ρ_b adds more total system resistance, the total throughput decreases monotonically as ρ_b increases.

Similar qualitative changes may be observed in the case where we model a feed solution with a distribution of particle sizes, described by the exponential size distribution function $g(s) = 1 - e^{-bs}$ (from (3.29)). In this case, whether or not particles are sieved (and hence block pores) depends on their size relative to the instantaneous pore radius. As the parameter b, measuring the relative characteristic sizes of pores and particles, is varied (Figure 3.4(b)), we again see the transition from blocking-dominated to adsorption-dominated behavior: when b is small, pores are smaller than particles, so pores rapidly become blocked and this is the dominant fouling mode; whereas when b is large pores are larger than

particles, hence little sieving occurs, and adsorption is the dominant fouling mode. A secondary consequence of increasing b ("large" particles becoming increasingly small relative to pores) is that the fouling is slower and net system resistance increases more slowly (large particles that are not sieved pass straight through the membrane), so total throughput increases. It must be remembered, however, that this increased throughput is achieved at the expense of decreased particle removal. For comparison, Figure 3.4(b) also shows the result for the case when the feed solution contains a homogenous distribution of large particles that are larger than the pores ($g(s) = 0$ throughout). As anticipated, this case is close to the small-b simulations, where most particles are larger than pores.

Another key consideration in evaluating membrane performance is the concentration of particles that remain in the filtrate as it exits the membrane, $c(1, t)$: in general, a lower particle concentration at the outflow side of the membrane indicates superior separation efficiency for the filter membrane. Figure 3.5(a) plots $c(1, t)$ versus throughput for each of the initial profiles given in (3.31). The results here are qualitatively consistent with those of the flux–throughput graphs of Figure 3.3(g), in particular, for a given "tolerance" value of the particle concentration at the outlet, membranes with narrow pores on the upstream side always give less total throughput than those whose pores are wide on the upstream side. Note, however, that in Figure 3.5(a), in order to obtain sufficiently distinct graphs, we set the dimensionless membrane-pore attraction coefficient $\lambda = 1$ and the dimensionless pore shrinkage rate $\beta = 0.05$, while values $\lambda = 2$ and $\beta = 0.1$ were used in Figure 3.3.

It is also of interest to study the influence of the membrane-pore attraction coefficient Λ, and of characteristics such as the membrane thickness D. These each appear in two of our dimensionless parameters: $\lambda = 8\Lambda\mu D^2/(P_0 W)$, and $\beta = 8\mu D\Lambda\alpha C_0/(\pi P_0 W^5 G_\infty)$ (see Table 3.3); hence we cannot vary the parameters λ and β in isolation. To study the effect of the attraction coefficient Λ (see (3.12);

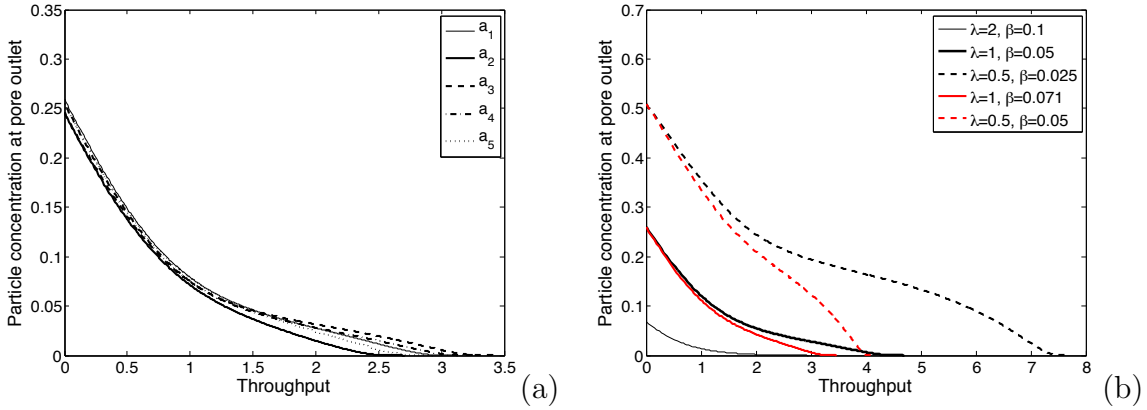

Figure 3.5 (a) Particle concentration at the downstream membrane surface $x = 1$ (pore exit) vs throughput, with $\lambda = 1$, $\beta = 0.05$, $\rho_b = 2$ and $g(s)$ given by (3.28), for several initial pore profiles given in (3.31); and (b) Particle concentration vs throughput graph for several different values of λ, for the uniform initial pore profile $a_1(x, 0) = 0.904$, with $\rho_b = 2$ and $g(s) = 1$. For the black curves we set $\beta \propto \lambda$ (corresponding to varying Λ in (3.12)) and for the red curves $\beta \propto \sqrt{\lambda}$ (corresponding to varying membrane thickness D).

this would be changed by, for example, changing the membrane material, or the type of particles in the feed solution) we consider different values of λ, with β changed in proportion to λ, consistent with the way Λ appears in the definitions of these two parameters. To study the effect of changing the membrane thickness D, we again consider different values of λ, but now take $\beta \propto \sqrt{\lambda}$. In Figure 3.5(b), we plot the particle concentration at the pore outlet, $c(1, t)$, versus throughput for several different values of λ, with $\beta \propto \lambda$ or $\beta \propto \sqrt{\lambda}$, corresponding to these two distinct system changes.

In the former case ($\beta \propto \lambda$), we associate small values of λ with weaker membrane-particle attraction. As anticipated, this is observed to give rise to poor separation of particles from feed, with a significant fraction of the small particles remaining suspended in the flow at the pore outlet. Large values of λ, corresponding to strong membrane-particle attraction, give uniformly low particle concentrations at the outlet. Such strong attraction is, of course, associated with faster total blocking of the membrane pores: if all particles adhere to the pore wall then the pore will close sooner. In the latter case ($\beta \propto \sqrt{\lambda}$), we associate smaller/larger values of λ

with thinner/thicker membranes. As above, we expect worse/better separation in this case (as measured by the particle concentration at the pore outlet), and this is borne out in the simulations. With a thin membrane the feed solution transits too quickly to deposit all of its particles (though the flux-throughput characteristics would look favorable, since a thin membrane affords little resistance to the flow, and poor particle removal corresponds to a slow fouling process). With a thick membrane the feed remains within the membrane long enough to deposit nearly all its particles, so separation is good; but of course the tradeoff is poorer flux-throughput characteristics, the thick membrane providing higher flow resistance and the good separation leading to more rapid fouling. Interestingly though, in comparing these two scenarios, changing the attraction coefficient appears to have a much larger effect on the overall behavior than does changing the membrane thickness, suggesting that membrane chemistry could be a very important consideration affecting overall performance.

In the context of these observations, we emphasize that our model considers all small particles to be identical. It may be the case that the feed contains several populations of small particles, each with a different deposition coefficient. While we do not explicitly model such a scenario, it would be a fairly straightforward extension to our model, and could be useful for an application in which only certain species are to be removed from a feed solution. We note also that λ and β are assumed to be constant throughout the duration of filtration. In reality, it may well be the case that particles adhere differently to the clean membrane than to the fouled membrane, so that the values of λ and β should change as filtration progresses. Such considerations are beyond the scope of this thesis.

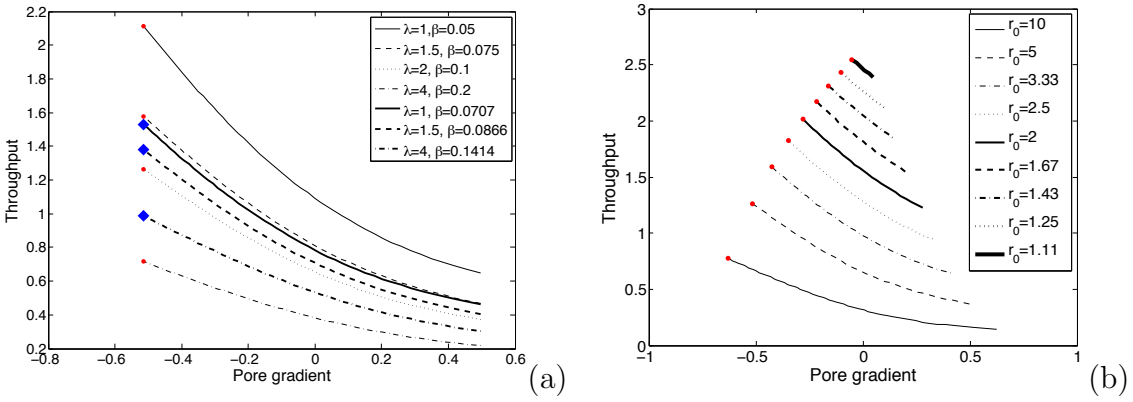

Figure 3.6 (a) Total throughput $\int_0^t q(t')dt'$ versus initial pore gradient b_0, keeping dimensionless initial net resistance, $r_0 = \int_0^1 \frac{dx'}{(a_0+b_0x')^4} = 5$, fixed, for several different values of λ, with homogeneous distribution of large particle sizes (3.28) and $\rho_b = 2$. For the thin curves we set $\beta \propto \lambda$ (corresponding to varying Λ; maximum throughput marked by red dots) and for the thick curves $\beta \propto \sqrt{\lambda}$ (corresponding to varying membrane thickness D; maximum throughput marked by blue diamonds). (b) Total throughput versus initial pore gradient b_0, for several different values of dimensionless initial resistance r_0 with homogeneous distribution of large particle sizes (3.28), $\lambda = 2$, $\beta = 0.1$ and $\rho_b = 2$. The red dots are maximum throughput for each given initial resistance r_0.

3.3.2 Optimal Initial Membrane Pore Profile

One question of interest to manufacturers is: for a membrane of given net (average) resistance, what is the optimum porosity profile as a function of depth through the membrane? For our model this translates to: what is the optimal shape of the filter pores among all filters with the same initial average resistance? To answer this question, we must first decide how to define filtration performance. This definition will vary depending on the user requirements (we have already seen above the tradeoff inherent between maximizing throughput and simultaneously removing as many particles as possible from the feed), but for purposes of illustration we will use the common experimental characterization of performance as the total throughput over the filter lifetime, as introduced earlier, noting that our methods can easily be adapted to give predictions for any other chosen efficiency measure. In our exposition below, we consider optimizing performance while fixing the initial average membrane resistance.

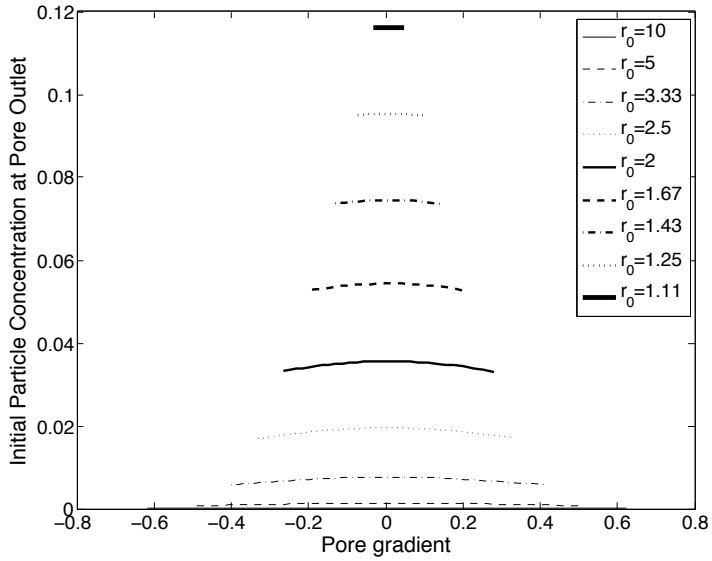

Figure 3.7 Initial total particle concentration at the pore outlet versus initial pore gradient b_0, for several different (small) values of dimensionless initial resistance r_0 with homogeneous distribution of large particle sizes (3.28), $\lambda = 2$, $\beta = 0.1$ and $\rho_{\mathrm{b}} = 2$.

Since the general optimization problem is very challenging, requiring consideration of pores of all possible shapes, we simplify by restricting attention to the class of membranes with pores whose initial radius $A(X, 0)$ varies linearly with membrane depth X. In order to make a meaningful comparison, we consider members of the family of all linear initial pore profiles, $a(x, 0) = a_0 + b_0 x$, with the same initial resistance $r_0 = r(0)$ (as defined by (3.30)). For a given value of the pore profile gradient b_0, the intercept value a_0 is then fixed. Note that, depending on the chosen value of r_0, not all values of b_0 may be possible: for a low-resistance, highly-permeable membrane, the pore occupies a large fraction of the period-box (within which it must be entirely confined), and hence the range of values of b_0 will be limited in such cases to small absolute values.

Figures 3.6(a) and (b) illustrate our results, plotting throughput versus pore gradient for several different scenarios. In Figure 3.6(a), the dimensionless initial resistance is fixed at $r_0 = 5$ (a value chosen large enough that a wide range of pore gradients are available), and throughput is plotted as a function of pore gradient for

several different values of the deposition coefficient λ. Recalling the discussion at the end of Section 3.3.1 above, we cannot change λ in isolation; here we consider the two cases discussed there: (i) we change β proportionally to λ, modeling changes in the dimensional particle-membrane attraction coefficient Λ (the thin curves), and (ii) we change β proportionally to $\sqrt{\lambda}$, modeling changes in the membrane thickness D (the thick curves).[2] In Figure 3.6(b), total throughput is again plotted versus slope of the initial pore profile, for several different values of the membrane resistance r_0. As noted above, only a limited range of pore gradients are realizable at low resistances.

In all cases shown in Figure 3.6, the optimum (as measured by maximal total throughput) is achieved at the most negative value of the pore profile gradient, in other words, the pore profile giving maximal total throughput is always that which is as wide as possible at the upstream membrane surface. This result is perhaps unsurprising given our previous simulation results of Figure 3.3 showing the rapid pore closure at the upstream surface: maximum throughput will be achieved by delaying this closure as long as possible.

Note that Figure 3.6 tells us nothing about the proportion of small particles captured in each filtration scenario (though they assume capture by sieving of all large particles). In Figure 3.7, we plot the (initial) total small-particle concentration at the pore outlet, for each case shown in Figure 3.6(b). It is evident from Figure 3.7 that (i) the net capture of small particles depends only weakly on the pore gradient; and (ii) in any case, the most negative pore gradient is favorable to improved net particle capture, leading to a slightly lower concentration of particles at the outlet compared with most other pore gradients.

[2]We note that there are many ways in which this study could be extended to give a more general optimization: we could for example allow both pore gradient and membrane thickness, and/or the size of the period box, to vary simultaneously while keeping initial membrane resistance fixed, which would involve a sweep through a larger parameter space. However, viewing the present work as a preliminary study, we defer a more general investigation to a future publication.

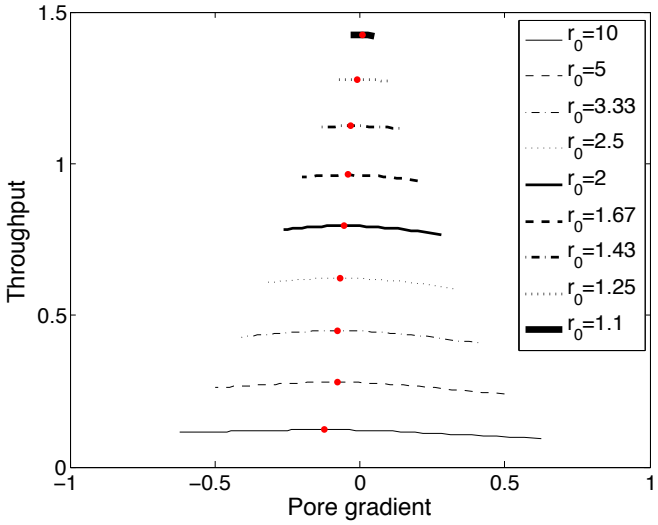

Figure 3.8 Total throughput versus initial pore gradient b_0, for several different (small) values of dimensionless initial resistance r_0 with homogeneous distribution of large particle sizes (3.28), $\lambda = 0.01$, $\beta = 0.1$ and $\rho_b = 2$. The red dots are maximum throughput for each case: note that in contrast to Figure 3.6 maximal throughput now occurs at some intermediate value of the pore gradient, and not the most negative value.

If we set such concerns aside then we might suspect that a different optimal result would be obtained for very low values of the deposition coefficient, where pore closure might in fact occur at an internal point for pores of decreasing radius. Figure 3.8 confirms this expectation: for $\lambda = 0.01$ and $\beta = 0.1$ the optimum profile is no longer the widest possible at the upstream side. A more uniform profile is now favored, but it should be noted that (i) gains in total throughput are only marginal in this situation; and (ii) in such small-λ simulations, only a very small fraction of the small particles is removed by the membrane.

Though we show results here only for the class of linear pore profiles, we note that preliminary investigations of other classes of pore shape (quadratic, cubic and simple exponential profiles) suggest very similar findings. In particular, although the actual optimal pore shapes obtained are somewhat different in each case, the maximal throughput in all cases is very similar, with only marginal improvements over the linear case.

3.4 Conclusions

We have presented a model that can describe the key effects of membrane morphology on separation efficiency and fouling of a membrane filter. Our model accounts for Darcy flow through the membrane, and for fouling by two distinct mechanisms: pore-blocking (sieving) by large particles, and adsorption of small particles within pores. While essentially predictive, our model contains several parameters that may be difficult to measure for a given system – most notably, the relative increase in pore resistance due to a blocking event, ρ_{b}; the dimensionless attraction coefficient between the membrane pore wall and particles, λ; and the dimensionless pore shrinkage rate, β. In practice, such parameters could be inferred by fitting to a reliable dataset; but even so these parameters will vary from one membrane-feed system to another, since they depend on membrane structure, on the type and size of the particles carried by the feed, and on the chemical interactions between the particles in the feed and the membrane material. The model as presented here implicitly assumes that all of the "small" particles comprising the concentration C are identical, but it would not (we think) be difficult to extend the modeling to account for several different types of small particles, each with its own concentration and its own sticking parameter.

In the absence of firm data on model parameters, we have chosen what we believe to be plausible parameter values (summarized at the start of Section 3.3) for most of our simulations. The focus in this chapter is on development of a model that can be used to quantify the effects of membrane morphology on separation efficiency, in terms of the performance (flux-throughput) curve of a membrane filter with known characteristics under given operating conditions, and by the graphs of particle concentration at pore outlet.

Our model accounts, in the simplest possible way, for variations in membrane pore profiles. The pore profile variation in real membranes is undoubtedly highly complex: here we restrict attention to simple axisymmetric pore profiles characterized

by depth-dependent initial radius $a(x, 0)$, which span the entire membrane depth, and we investigate how filtration performance varies as these initial pore profiles change. Our results simulating filtration at constant pressure drop indicate that such variations in pore profile lead to different fouling patterns within the membrane. More importantly, if the initial pore radius at the top of membrane is small (pore profile $a_2(x)$ in (3.31)), it can give rise to a marked decrease in filter performance as quantified by the total amount of filtrate processed under the same operating conditions, as shown by Figure 3.3(g). This figure, which summarizes results for five distinct (equal resistance) initial pore profiles, shows that the case where the initial pore profile is linear decreasing across the membrane, given by $a(x, 0) = a_3(x)$ (see equation (3.31)), gives significantly higher total throughput when compared with the other cases considered (initial pore profile uniform, linear increasing, concave/convex parabolic across the membrane).

Similar differences in performance, though less pronounced, are observed for the case where the total flux is prescribed (rather than the pressure drop), as shown in Figure C.1(f) in Appendix C. Maintaining the same flux requires a significantly higher pressure drop for the linear increasing case $a(x, 0) = a_2(x)$ than for all other cases, while the case $a(x, 0) = a_3(x)$, linear decreasing pore profile in (3.31), shows the best performance, requiring the lowest pressure drop to sustain the desired flux.

When studying the influence of the deposition (or particle-pore attraction) parameter $\lambda = 8\Lambda\mu D^2/(P_0 W)$, care must be taken to track the concentration of small particles, both within the membrane and in particular at the downstream edge of the membrane (Figures 3.5 and 3.6). A naive interpretation of Figure 3.6(a) would suggest that smaller values of λ are preferable, since these lead to greater total throughput. However, a glance at Figure 3.5(b) confirms that if λ is too small then a large concentration of small particles remain in the filtrate, which is likely undesirable. From the definition of λ, this could stem from several causes; *e.g.,* there

may be insufficiently strong attractive forces between particles and membrane (Λ); the filter membrane may be too thin (D); or the pressure drop may be too high (P_0) so filtration is too fast to give good deposition.

This brings us to another major performance requirement of filtration: to achieve the desired level of particle separation from the feed solution. This separation level may vary from one application to another (sometimes a filtrate should be as clean as possible, with all impurities removed; at other times a threshold level of impurities may be tolerated, or it may be desirable to remove only a certain type of particles from the feed) and hence the best choice of filter may depend on the application. If we consider the simplest scenario in which the filtrate should be as clean as possible, while simultaneously maximizing throughput, then for a given tolerance level of impurities (maximum allowable concentration $c(1,t)$ at pore outlet), the more throughput the filter gives, the better performance it has. Figure 3.5(a) shows that among all the initial pore profiles given in (3.31), $a_2(x)$ and $a_3(x)$ have the worst and the best performance respectively, under these criteria.

We note that the flux-throughput curves generated by our model are in good qualitative agreement with experimental data from the literature, as seen in, *e.g.,* [23, 36] and many other works. This consistency between our model results and the experimental data gives us further confidence that our model, based as it is on first principles assumptions about how fouling occurs, is sound, and provides a good basis for predictive simulations. While a more complicated model could perhaps provide more accurate predictions, our model has the advantage that it is simple and quick to simulate, offering a useful tool for investigating filter design characteristics.

Our predictive model leads naturally to questions of how membrane structure may be optimized. Defining optimal performance is very application-dependent, and in this chapter we consider only a simple optimization, maximizing total throughput of filtrate over the filter lifetime as the pore profile is varied. We do not explicitly

optimize also for particle removal efficiency, which is of course important; but we compare performance only of membranes with the same initial net resistance, assuming that particle removal is comparable for such membranes (as is borne out by the simulations shown in Figures 3.5(a) and 3.7). We optimize only within a restricted class of pore profiles, presenting detailed results for linear pore profiles (preliminary work suggests that considering a larger class of profiles yields only marginal improvements). We note that our findings here are remarkably consistent with those of [24], despite the many differences in approach. Collaborative work is ongoing to reach quantitative agreement between these different models.

There are of course many alternative approaches to optimization that could be considered, and a full investigation is beyond the scope of this thesis. One could, as noted in Section 3.3.2 above, extend the investigation to sweep through a larger parameter space in which the membrane thickness D and the size of the period-box $2W$ are varied while keeping membrane resistance fixed. Another approach that could be interesting is to reverse time in the problem: if one assumes that the "optimal" filtration scenario is that in which pore closure occurs uniformly along the length of the pore (such a scenario would maximize the time for which the pore is open), then one could run the model backwards to simulate the opening of an infinitesimally thin, parallel-sided pore. Stopping the simulation when the net resistance reaches a chosen value would then provide the optimal pore shape for that chosen resistance (of course, there are still other optimization questions here relating to varying the membrane thickness and the period-box size).

Finally, though our model represents an important first step in systematically accounting for internal membrane complexity, it must be emphasized that real membranes are much more complicated in structure than our simple assumptions allow, as is evident from a glance at Figure 3.1. They may consist of many randomly oriented pores, which branch and reconnect, so that the feed solution takes a winding

and tortuous path through the membrane rather than the simple flow assumed here. In Chapter 5, we will describe more sophisticated models, with branching and reconnecting pores, to better account for such internal membrane complexity.

CHAPTER 4

MODELING MEMBRANE FILTRATION WITH MULTIPLE FOULING MECHANISMS: THE EFFECT OF PERMEABILITY VARIATIONS

4.1 Introduction

In Chapter 3, we developed a model that can describe the key effects of membrane morphology on separation efficiency and fouling of a membrane filter. Our model accounts for Darcy flow through the membrane, and two distinct mechanisms of fouling: adsorption of small particles within pores, and pore-blocking (sieving) by large particles. In this chapter, we propose a novel model for the formation and growth of a cake layer on the upstream side of the filter, and couple this to our earlier model, to allow all fouling modes to operate simultaneously. We present several simulations of our model, with an emphasis on how each type of fouling affects results, and how changes in membrane structure (modeled by different choices of pore profile within the membrane) impact the outcome. In particular, we discuss how our model (properly calibrated) could be used to calculate the optimum pore profile, within the limitations of our modeling. We conclude with a discussion of our model and results in the context of real membrane filters.

4.2 Darcy Flow and Fouling Model

As discussed in Chapter 3, again we consider dead-end filtration through a planar membrane that lies parallel to the (Y, Z)-plane, with unidirectional Darcy flow through the membrane in the positive X-direction. The membrane properties and flow are assumed homogeneous in the (Y, Z)-plane, but the membrane has depth-dependent permeability (even if permeability is initially uniform, fouling will lead to nonuniformities over time), which we denote by $K_{\mathrm{m}}(X, T)$. We use uppercase

fonts to denote dimensional quantities, and in the following will introduce subscripts "m" and "c" to distinguish (where necessary) between quantities in the membrane and in the cake layer.

The superficial Darcy velocity $\mathbf{U} = (U(X,T), 0, 0)$ within the membrane is given in terms of the pressure $P_{\rm m}$ by

$$U = -\frac{K_{\rm m}(X,T)}{\mu}\frac{\partial P_{\rm m}}{\partial X}, \quad \frac{\partial}{\partial X}\big(K_{\rm m}(X,T)\frac{\partial P_{\rm m}}{\partial X}\big) = 0, \quad 0 \le X \le D, \tag{4.1}$$

where μ is the viscosity of the feed solution, D is the membrane thickness and μ is the viscosity of Newtonian feed solution. The modeling challenge is to link the permeability $K_{\rm m}(X,T)$ to membrane characteristics, which evolve in time due to fouling, to obtain a predictive model. Within our model, membrane permeability decreases in time (*i.e.*, membrane resistance increases in time) due to fouling by three mechanisms: (i) pores become blocked from above by particles too large to pass through pores; (ii) pore radius decreases in time due to adsorption of tiny particles within the pores; and (iii) at a late stage, particles deposited on the filter upstream form a cake layer. This cake layer is assumed to occupy the region $-I(T) \le X \le 0$, so that $I(T)$ is the cake thickness, with $I(0) = 0$.

We consider a simple model in which the membrane consists of a series of identical axisymmetric slender pores of variable radius $A(X,T)$, which traverse the membrane thickness (Figure 3.2). Pores are arranged in a square repeating lattice, with period $2W$, and a filtrate, carrying *small* particles (at concentration $C(X,T)$) and *large* particles (larger than pores; discussed below), which are deposited within the membrane and on top of the membrane, respectively, is driven through the filter. In Chapters 2 and 3 ([48, 49]), we considered two driving mechanisms: (i) constant pressure drop across the membrane specified; and (ii) constant flux through the membrane specified. In the former case, the flux will decrease in time as the membrane becomes fouled; in the latter case, the pressure drop required to sustain

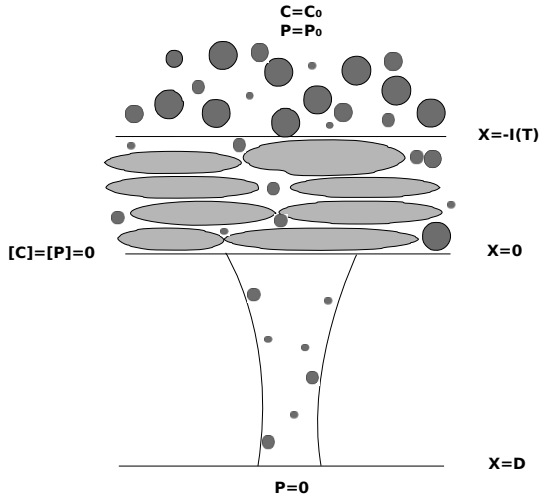

Figure 4.1 Schematic showing the pore and cake layer.

the constant flux will rise as fouling occurs. In this chapter, we will consider only case (i), which is the most common in practice. With constant pressure drop P_0, the conditions applied above and below the membrane are

$$P_{\mathrm{c}}(-I(T), T) = P_0, \quad P_{\mathrm{m}}(D, T) = 0, \tag{4.2}$$

where P_{c} is the pressure within the cake, and $X = -I(T)$ is the top of the cake (see Figure 4.1). Initially all pores have specified radius, $A(X, 0) = A_0(X)$. Where an individual pore (at time T) is unblocked the total flux through it $Q_{\mathrm{u,pore}}(T)$ is given (approximately) by

$$Q_{\mathrm{u,pore}} = -\frac{1}{R_{\mathrm{u}}}\frac{\partial P_{\mathrm{m}}}{\partial X} \quad \text{where} \quad R_{\mathrm{u}} = \frac{8\mu}{\pi A^4}, \tag{4.3}$$

and R_{u} is the pore resistance per unit of the membrane depth.

4.2.1 Pore Blocking by Large Particles

Blocking occurs when a particle from population of large particles becomes trapped at the entrance to a pore, obstructing the flow. We follow our earlier approach in

Chapters 2 and 3 to model this effect by adding an extra resistance of magnitude $8\mu\rho_{\rm b}/(\pi A_0^4)$ (again per unit of the membrane depth), where $\rho_{\rm b}$ is a dimensionless number, in series with the resistance $R_{\rm u}$. The flux through a blocked pore, $Q_{\rm b,pore}(X,T)$, is then given by

$$Q_{\rm b,pore} = -\frac{1}{R_{\rm b}}\frac{\partial P_{\rm m}}{\partial X} \quad \text{where} \quad R_{\rm b} = \frac{8\mu}{\pi A_0^4}\left(\left(\frac{A_0}{A}\right)^4 + \rho_{\rm b}\right). \tag{4.4}$$

The parameter $\rho_{\rm b}$ characterizes blocking strength: for large values of $\rho_{\rm b}$ pore resistance increases dramatically after blocking, while for small values resistance is almost unchanged. Total pore blocking is retrieved as $\rho_{\rm b} \to \infty$. We can now relate the superficial Darcy velocity U to the number densities of unblocked and blocked pores per unit area, $N(T)$ and $N_0 - N(T)$, respectively (where $N_0 = N(0)$ and $N_0(2W)^2 = 1$) by noting that the flux of fluid per unit area of membrane is

$$N_0(2W)^2 U = N(T)Q_{\rm u,pore} + (N_0 - N(T))Q_{\rm b,pore},$$

hence, substituting for $Q_{\rm u,pore}$ from (4.3) and for $Q_{\rm b,pore}$ from (4.4) in the above, we obtain

$$U = -\frac{\pi A_0^4}{8\mu}\frac{\partial P_{\rm m}}{\partial X}\left(\frac{N}{(A_0/A)^4} + \frac{N_0 - N}{(A_0/A)^4 + \rho_{\rm b}}\right). \tag{4.5}$$

The instantaneous number density of unblocked pores, $N(T)$, decreases as pores become blocked. We assume blockage occurs whenever a particle with radius $S > A(0,T)$ is advected to the pore entrance. For simplicity, here we assume that our large-particle population consists entirely of particles larger than $A(0,T)$, while our small-particle population (discussed below) consists of particles that are smaller than $A(X,T)$ throughout (in Chapter 3, we proposed how to deal with a distribution of large-particle sizes where some are smaller than pores). If G is the concentration of the large particles then the probability that a particular pore is blocked (per unit time) is $GQ_{\rm u,pore}$:

$$\left[\begin{array}{c}\text{Probability per unit time that}\\ \text{pore of radius } A \text{ is blocked}\end{array}\right] = -G\,\frac{\pi A^4}{8\mu}\frac{\partial P_{\rm m}}{\partial X}\bigg|_{X=0}.$$

It follows that $N(T)$ evolves according to

$$\frac{\partial N}{\partial T} = NG\frac{\pi A^4}{8\mu}\frac{\partial P_{\rm m}}{\partial X}\bigg|_{X=0}. \tag{4.6}$$

4.2.2 Pore Blocking by Adsorption

To model adsorptive fouling requires consideration of how the small particles are advected and deposited within the pores of the membrane. Following Chapter 3, we propose a simple advection model for the concentration of small particles, $C_{\rm m}$, within the membrane, which assumes that particles are deposited on the wall at a rate proportional to both the local particle concentration, and to the available wall circumference:

$$U_{\rm pm}\frac{\partial C_{\rm m}}{\partial X} = -\Lambda_{\rm m}\frac{C_{\rm m}}{A}, \quad 0 \le X \le D, \tag{4.7}$$

where $U_{\rm pm}$ is the pore velocity within the membrane (the cross-sectionally averaged axial velocity within each pore) and $\Lambda_{\rm m}$ is a constant that captures the physics of the attraction between particles and wall that is causing the deposition (a derivation is given in Appendix B). The pore velocity $U_{\rm pm}$ satisfies

$$\frac{\partial\left(\pi A^2 U_{\rm pm}\right)}{\partial X} = 0, \quad 4W^2U = \pi A^2 U_{\rm pm}, \tag{4.8}$$

by simple mass conservation arguments. The pore radius shrinks in response to the deposition; we propose

$$\frac{\partial A}{\partial T} = -\Lambda_{\rm m}\alpha C_{\rm m}, \quad 0 \le X \le D, \tag{4.9}$$

for some constant α (related to the particle size). The initial pore radius is specified throughout the membrane,

$$A(X,0) = A_0(X), \quad 0 \le X \le D. \tag{4.10}$$

4.2.3 Cake Formation

In the later stages of filtration, particles may accumulate on the upstream side of the membrane, forming a *cake* layer as shown in Figure 4.1. This new layer in turn increases the system resistance and becomes thicker in time. To have a realistic late-stage filtration model, we wish to consider the effects of this cake layer.

Following blocking of pores by large particles on top of them, we assume that this creates new "membrane" area available for formation of a caking layer. If we assume that material (comprising large particles) is deposited on available membrane at a rate proportional to the flux and number of blocked pores, then we may propose a model for how the cake layer thickness $I(T)$ increases in time,

$$\frac{dI}{dT} = (N_0 - N)(2W)^2(G\Delta_\mathrm{p})U, \quad I(0) = 0, \tag{4.11}$$

where G is the total particle concentration defined earlier, U is the feed solution flux (the superficial Darcy velocity), defined in (4.5), and Δ_p is the effective particle volume within the cake layer. This model says that the thickness of cake layer increases at a rate proportional to the membrane area available for caking, the concentration of large particles that form the cake, the volume of those particles, and the fluid flux. At the cake's upper surface, we have specified pressure and small-particle concentration

$$P_\mathrm{c}(-I(T),T) = P_0, \quad C_\mathrm{c}(-I(T),T) = C_0.$$

The cake layer itself behaves like a secondary filter membrane, with some permeability $K_\mathrm{c}(X,T)$ (a function of the characteristics of the particles suspended

in the feed solution), which decreases in time due to deposition of small particles within it. We can therefore again use the Darcy model to describe flow across the cake:

$$U = -\frac{K_\mathrm{c}}{\mu}\frac{\partial P_\mathrm{c}}{\partial X}, \quad -I(T) \le X \le 0, \quad P_\mathrm{c}(-I(T), T) = P_0. \tag{4.12}$$

Since the cake is composed of particles, we use the Kozeny-Carman equation (see, *e.g.* [45]) to relate its permeability K_c to its void fraction ϕ_c:

$$K_\mathrm{c} = \frac{\phi_\mathrm{c}^3}{K_\mathrm{oz} S_\mathrm{cp}^2 (1-\phi_\mathrm{c})^2}, \tag{4.13}$$

where $\phi_\mathrm{c}(T)$ is the void fraction or porosity of the cake ($\phi_\mathrm{c} \in (0,1)$; for randomly-packed spherical particles for example, $\phi_\mathrm{c} \approx 0.37$); S_cp is the specific area (the ratio of the surface area to the volume of the solid fraction of the porous medium); and K_oz is the Kozeny constant (Carman proposed a value of 5 in [45]).

The model for the cake layer is completed by making assumptions about how small particles are deposited within the cake, increasing its resistance. In the spirit of our membrane fouling model (4.7), we propose a simple advection model for the small particles:

$$U_\mathrm{pc}\frac{\partial C_\mathrm{c}}{\partial X} = -\Lambda_\mathrm{c}\frac{C_\mathrm{c}}{(\phi_\mathrm{c}\Delta_\mathrm{p})^{1/3}}. \tag{4.14}$$

Here the pore velocity U_pc within the cake is related to the superficial Darcy velocity U by

$$U_\mathrm{pc} = \frac{U}{\phi_\mathrm{c}}. \tag{4.15}$$

As before, the model assumes that small particles are deposited at a rate proportional to the local particle concentration. The constant Λ_c captures the physics of the attraction between the large particles (which constitute the cake) and the small particles. The cake structure is, of course, very complicated in reality; but in essence the pores of the cake consist of the spaces between particles of volume Δ_p, therefore we

assume that $(\phi_c\Delta_p)^{1/3}$ will be proportional to the cake pore radius (whence the term in the denominator on the right-hand side of (4.14)). The cake porosity ϕ_c decreases in response to the particle deposition: consistent with our earlier membrane deposition model (see (4.9) with $A \propto (\phi_c\Delta_p)^{1/3}$) we propose

$$\frac{\partial \phi_c}{\partial T} = -\Lambda_c(\phi_c\Delta_p)^{2/3}C_c. \tag{4.16}$$

These last two equations (4.14), (4.16) are analogous to equations (4.7) and (4.9) in the membrane model, respectively. We must also have continuity of particle concentration and pressure at the interface between the cake layer and the membrane,

$$C_c(0,T) = C_m(0,T), \quad P_c(0,T) = P_m(0,T). \tag{4.17}$$

For future reference, we note the simple pressure drop equation

$$\triangle P|_{-I(T)}^{D} = \triangle P_m|_0^D + \triangle P_c|_{-I(T)}^0, \tag{4.18}$$

or, in integral form,

$$\int_{-I(T)}^{D} \frac{\partial P}{\partial X}dX = \int_0^D \frac{\partial P_m}{\partial X}dX + \int_{-I(T)}^{0} \frac{\partial P_c}{\partial X}dX. \tag{4.19}$$

4.3 Scaling and Nondimensionalization

We nondimensionalize the model presented above using the scalings

$$(X,I) = D(x,i), \quad A = Wa, \quad T = \frac{8\mu D}{\pi P_0 W^4 G}t, \quad (U, U_{pm}, U_{pc}) = \frac{\pi P_0 W^2}{32\mu D}(u, u_{pm}, u_{pc}),$$

$$(P_m, P_c) = P_0(p_m, p_c), \quad (C_m, C_c) = C_0(c_m, c_c), \quad N = N_0 n, \quad K_c = \frac{\pi W^2}{32}k_c, \tag{4.20}$$

giving a dimensionless model for $u(x,t)$, $u_{pm}(x,t)$, $u_{pc}(x,t)$, $p_m(x,t)$, $p_c(x,t)$, $a(x,t)$, $c_m(x,t)$, $c_c(x,t)$, $i(t)$, $k_c(t)$, $\phi_c(t)$ and $n(t)$. The dimensionless governing equations in the membrane layer $0 \le x \le 1$ become

$$4u = \pi a^2 u_{pm}, \tag{4.21}$$

$$u = -a^4 \frac{\partial p_\mathrm{m}}{\partial x}\left(\frac{1-n}{1+\rho_\mathrm{b} a^4} + n\right), \quad \frac{\partial u}{\partial x} = 0, \tag{4.22}$$

$$u_\mathrm{pm}\frac{\partial c_\mathrm{m}}{\partial x} = -\lambda \frac{c_\mathrm{m}}{a}, \quad \lambda = \frac{32\Lambda_\mathrm{m}\mu D^2}{\pi P_0 W^3}, \tag{4.23}$$

$$\frac{\partial a}{\partial t} = -\beta_\mathrm{m} c_\mathrm{m}, \quad \beta_\mathrm{m} = \frac{8\mu D\Lambda_\mathrm{m}\alpha C_0}{\pi P_0 W^5 G}, \tag{4.24}$$

$$\frac{dn}{dt} = n a^4 \left.\frac{\partial p_\mathrm{m}}{\partial x}\right|_{x=0}, \tag{4.25}$$

with boundary and initial conditions

$$p_\mathrm{m}(1,t) = 0, \quad a(x,0) = a_0(x), \tag{4.26}$$

where $a_0(x) < 1$ is a specified function.

The governing equations in the cake layer $-i(t) \le x \le 0$ are:

$$u_\mathrm{pc} = \frac{u}{\phi_\mathrm{c}}, \tag{4.27}$$

$$u = -k_\mathrm{c}\frac{\partial p_\mathrm{c}}{\partial x}, \quad \frac{\partial u}{\partial x} = 0, \tag{4.28}$$

$$k_\mathrm{c} = \kappa_\mathrm{c}\frac{\phi_\mathrm{c}^3}{(1-\phi_\mathrm{c})^2}, \quad \kappa_\mathrm{c} = \frac{32}{\pi W^2 K_\mathrm{oz} S_\mathrm{cp}^2}, \tag{4.29}$$

$$\frac{\partial \phi_\mathrm{c}}{\partial t} = -\beta_\mathrm{c} c_\mathrm{c} {\phi_\mathrm{c}}^{2/3}, \quad \beta_\mathrm{c} = \frac{8\mu D\Lambda_\mathrm{c}{\Delta_p}^{2/3} C_0}{\pi P_0 W^4 G}, \tag{4.30}$$

$$u_\mathrm{pc}\frac{\partial c_\mathrm{c}}{\partial x} = -\lambda_\mathrm{c}\frac{c_\mathrm{c}}{\phi_\mathrm{c}^{1/3}}, \quad \lambda_\mathrm{c} = \frac{32\Lambda_\mathrm{c}\mu D^2}{\pi P_0 W^2 {\Delta_p}^{1/3}}, \tag{4.31}$$

$$\frac{di}{dt} = \eta(1-n)u, \quad \eta = \frac{\Delta_p}{4W^2 D}, \tag{4.32}$$

with boundary and initial conditions

$$p_{\mathrm{c}}(-i(t),t)=1, \quad c_{\mathrm{c}}(-i(t),t)=1. \tag{4.33}$$

The above implicitly assumes that the specific area, S_{cp}, is constant throughout. This will not quite be true, but we believe it is reasonable to neglect its evolution due to fouling. The model is closed by continuity conditions at the interface between the membrane and the cake,

$$c_{\mathrm{c}}(0,t)=c_{\mathrm{m}}(0,t), \quad p_{\mathrm{c}}(0,t)=p_{\mathrm{m}}(0,t), \tag{4.34}$$

and by the flux balance equations

$$4\phi_{\mathrm{c}}u_{\mathrm{pc}}=4u=\pi a^2 u_{\mathrm{pm}}. \tag{4.35}$$

Significant analytical progress may be made with this model. Equations (4.22) with the boundary condition at the pore outlet, $p_{\mathrm{m}}(1,t)=0$, give the pressure within the pore, $p_{\mathrm{m}}(x,t)$, as

$$p_{\mathrm{m}}(x,t)=u\int_x^1 \frac{dx'}{a^4(\frac{1-n}{1+\rho_{\mathrm{b}}a^4}+n)}, \tag{4.36}$$

while equations (4.28) and (4.33) give the pressure in the cake layer as

$$p_c(x,t)=1-u\int_{-i(t)}^{x}\frac{dx'}{k_{\mathrm{c}}}. \tag{4.37}$$

By using the continuity condition (4.34) for the pressure, we find the dimensionless Darcy velocity as

$$u=\left(\int_{-i(t)}^{0}\frac{dx'}{k_{\mathrm{c}}}+\int_0^1\frac{dx'}{a^4(\frac{1-n}{1+\rho_{\mathrm{b}}a^4}+n)}\right)^{-1}. \tag{4.38}$$

From equation (4.25) the number of unblocked pores satisfies

$$\frac{dn}{dt}=-\,n\left(\int_{-i(t)}^{0}\frac{dx'}{k_{\mathrm{c}}}+\int_0^1\frac{dx'}{a^4(\frac{1-n}{1+\rho_{\mathrm{b}}a^4}+n)}\right)^{-1}\Big(\frac{1-n}{1+\rho_{\mathrm{b}}a^4}+n\Big)^{-1}\Bigg|_{x=0}, \tag{4.39}$$

and the cake layer thickness can be easily found from equation (4.4)

$$\frac{di}{dt} = \eta(1-n)\left(\int_{-i(t)}^{0} \frac{dx'}{k_{\mathrm{c}}} + \int_{0}^{1} \frac{dx'}{a^4(\frac{1-n}{1+\rho_{\mathrm{b}}a^4}+n)}\right)^{-1}. \tag{4.40}$$

Finally we simplify the equations for particle concentration within the membrane and the cake layer ((4.23) and (4.31)) as

$$\frac{\partial c_{\mathrm{m}}}{\partial x} = -\lambda_{\mathrm{m}} c_{\mathrm{m}} a\left(\int_{-i(t)}^{0} \frac{dx'}{k_{\mathrm{c}}} + \int_{0}^{1} \frac{dx'}{a^4(\frac{1-n}{1+\rho_{\mathrm{b}}a^4}+n)}\right),\ c_{\mathrm{m}}(0,t) = c_{\mathrm{c}}(0,t),\ \lambda_{\mathrm{m}} = \frac{8\Lambda_{\mathrm{m}}\mu D^2}{P_0 W^3}, \tag{4.41}$$

$$\frac{\partial c_{\mathrm{c}}}{\partial x} = -\lambda_{\mathrm{c}}\phi_{\mathrm{c}}^{2/3} c_{\mathrm{c}}\left(\int_{-i(t)}^{0} \frac{dx'}{k_{\mathrm{c}}} + \int_{0}^{1} \frac{dx'}{a^4(\frac{1-n}{1+\rho_{\mathrm{b}}a^4}+n)}\right), \quad c_{\mathrm{c}}(-i(t),t) = 1, \tag{4.42}$$

and we have the pore shrinkage equation

$$\frac{\partial a}{\partial t} = -\beta_{\mathrm{m}} c_{\mathrm{m}}, \tag{4.43}$$

where β_{m} is given in (4.24).

4.4 Optimizing for the Membrane Pore Profile

A question of interest to manufacturers is: for a membrane of given net resistance, what is the optimum permeability profile as a function of depth through the membrane? For our model this translates into asking: what is the optimal shape of the filter pores? In order to answer this question, we must first choose a measure of filtration performance. This measure will vary depending on the user requirements, but for purposes of illustration, we consider the common experimental characterization of performance as the total volume of filtrate over the filter lifetime (total throughput), defined by $\int_0^{t_{\mathrm{f}}} q(t')dt'$, where $q(t) = u(0,t)$ is our dimensionless flux at any given time and t_{f} is the final time of filtration.

The general optimization problem is very challenging, requiring consideration of pores of all possible shapes, so we simplify by restricting attention to the class of membranes with pores whose initial radius $a(x,0)$ is polynomial in the depth of the

membrane x,

$$a(x,0) = a_0(x) = \sum_{i=0}^{n} b_i x^i. \tag{4.44}$$

To make a meaningful comparison, we should compare performance of membranes that are similar in some quantifiable way. In our earlier work [49], we compared membranes with linear pore profiles and with the same initial net resistance, $r(0)$, defined as

$$r(0) = \int_0^1 a^{-4}(x,0)dx. \tag{4.45}$$

While tractable for the small class of linear pores, this approach becomes very costly to implement for the wider class of polynomial pore profiles. However, for quite a range of different pore shapes and sizes, we have observed that membranes of the same initial net porosity, defined as

$$\bar{\phi}_{\mathrm{m}}(0) = \frac{\pi}{4}\int_0^1 a^2(x,0)dx, \tag{4.46}$$

(the factor of $1/4$ because with our nondimensionalization each pore is confined within a box of area 4 units) have very nearly the same net resistance (this appears to be true to within about 8% for porosities $\bar{\phi}_{\mathrm{m}}(0) \in (0.6, \pi/4)$). We may, therefore, compare instead filter membranes with polynomial initial pore profile, and with the same net initial void fraction or porosity $\bar{\phi}_{\mathrm{m}}(0) = \bar{\phi}_{\mathrm{m}_0}$, As we shall see, this is an easier problem.

We write the initial pore profile in terms of an orthogonal basis. Let $\tilde{P}_n(x)$ be the nth Legendre polynomial, an nth degree polynomial defined on $[-1,1]$ that can be expressed via Rodrigues' formula [3]

$$\tilde{P}_n(x) = \frac{1}{2^n n!}\frac{d^n}{dx^n}[(x^2-1)^n]. \tag{4.47}$$

The $\tilde{P}_n(x)$ also satisfy the recursive formula

$$(n+1)\tilde{P}_{n+1}(x) = (2n+1)x\tilde{P}_n(x) - n\tilde{P}_{n-1}(x), \quad \text{where} \quad \tilde{P}_0(x) = 1, \quad \tilde{P}_1(x) = x. \tag{4.48}$$

An important property of the Legendre polynomials is that they are orthogonal with respect to the L^2 inner product on the interval $[-1, 1]$,

$$\int_{-1}^{1} \tilde{P}_n(x)\tilde{P}_m(x)dx = \frac{2}{2n+1}\delta_{mn}. \tag{4.49}$$

This property underlies the advantage of using porosity rather than resistance in order to tackle the problem easily. Note that the initial pore profile, $a_0(x)$ is defined on the interval $[0, 1]$, so we use an affine transformation to introduce the shifted Legendre polynomials as $P_n(x) = \tilde{P}_n(2x-1)$, which can be calculated either from (4.47) or (4.48). These shifted Legendre polynomials are also orthogonal, with

$$< P_i(x), P_j(x) >_{L^2} = \int_0^1 P_i(x)P_j(x)dx = \frac{1}{2i+1}\delta_{ij}, \tag{4.50}$$

(this follows trivially from (4.49)). Next we write the initial pore profiles as

$$a_0(x) = \sum_{i=0}^{n} b_i P_i(x), \quad \text{where} \quad b_i = (2i+1)\int_0^1 a_0(x)P_i(x)dx, \tag{4.51}$$

where $P_i(x)$ is the ith degree shifted Legendre polynomial. Combining (4.46) and (4.50) gives us the initial void fraction or porosity $\bar{\phi}_{\mathrm{m}_0} = \bar{\phi}_{\mathrm{m}}(0)$ as

$$\bar{\phi}_{\mathrm{m}_0} = \frac{\pi}{4}\sum_{i=0}^{n} \frac{b_i^2}{2i+1}. \tag{4.52}$$

This approach may be generalized to more general initial pore profiles, as we discuss later.

4.5 Results

In this section, we present some sample simulations of the model summarized in Section 4.3 showing how results depend on the pore features and parameters. Our

Table 4.1 Approximate Dimensional Parameter Values [34]

Parameter	**Description**	**Typical Value**
$2W$	Length of the square repeating lattice	4.5 μm (very variable)
Λ_{m}	Particle-wall attraction coefficient	Unknown (depends on characteristics of membrane and feed solution)
Λ_{c}	Small particle-large particle attraction coefficient	Unknown (depends on feed solution)
D	Membrane thickness	300 μm
A_0	Initial pore radius	2 μm (very variable)
α	Pore shrinkage parameter (see (4.9)) related to particle size	Depends on application
G	Total concentration of large particles in feed	Depends on application
N_0	Number of pores per unit area	7×10^{10} m^{-2} (very variable)
P_0	Pressure drop	Depends on application
Q_{pore}	Flux through a single pore	Depends on application
C_0	Total concentration of small particles in feed	Depends on application
K_{oz}	Kozeny constant	5
S_{cp}	Specific area; the ratio of surface area to the volume of the solid fraction in the cake	Depends on application
Δ_{p}	Effective particle volume within the cake layer	Depends on application

model contains several dimensionless parameters and functional inputs, which must be specified: λ_{m}, which captures the physics of the attraction between small particles and the membrane pore wall, leading to adsorptive fouling; λ_{c}, which captures the attraction between small and large particles that leads to adsorption of small particles within the cake; β_{m}, the dimensionless pore shrinkage rate; β_{c}, the rate of decreasing pore porosity in the cake layer; ρ_{b}, the ratio of the additional resistance due to pore-blocking to the original resistance of the unblocked pore; κ_{c}, the cake

permeability; and the rate of increasing cake layer thickness; η. An exhaustive investigation of the effects of each of these parameters is clearly impractical. Their values depend on physical dimensional parameters that must be measured for the particular system under investigation, and we lack such detailed experimental data; hence we have to make our best guess as to the most appropriate values to use in our simulations. The parameters are summarized in Tables 4.1 (dimensional parameters) and 4.2 (dimensionless parameters) along with typical values, where known.

Given the number of parameters, most of them will be fixed throughout our simulations. The value of the dimensionless attraction coefficients between pore wall and particles, and also between large and small particles in the cake layer, λ_{m} and λ_{c}, respectively, are unknown, and could certainly vary quite widely from one system to another depending on the detailed structure of the filter membrane. In the absence of firm data on their values, we take $\lambda_{\mathrm{m}} = 2$ and $\lambda_{\mathrm{c}} = 0.5$ for most simulations. The dimensionless membrane and cake pore shrinkage rates, β_{m} and β_{c}, respectively, are unknown but will normally be small (these represent the ratios of the timescales of adsorptive pore closure to pore blocking in membrane and cake): we set $\beta_{\mathrm{m}} = \beta_{\mathrm{c}} = 0.1$. Assuming that blocking of a pore by a particle increases its resistance by twice the original resistance of the unblocked pore, we set $\rho_{\mathrm{b}} = 2$ for most simulations. Finally, in the absence of firm data, η is set to 0.05, while the dimensionless cake permeability constant κ_{c} is set to 1. We briefly demonstrate the effect of changing parameters λ_{c}, β_{c} and η later.

For the pore radius function, $a(x,t)$, we investigate several different initial pore profiles to see how this affects the outcome. Recalling the discussion of Section 4.4, we first run some sample simulations for pore shapes that give the same initial membrane resistance $r_0 = r(0)$. This means that we are comparing membranes that perform identically when no fouling occurs – they give identical throughputs when filtering

Table 4.2 Dimensionless Parameters and Approximate Values

Parameter	**Formula & description**	**Typical value**
λ_{m}	$(8\Lambda_{\mathrm{m}}\mu D^2)/(P_0W^3)$	Unknown; values in
	Dimensionless particle-wall attraction coefficient	range 0.1–10 used
λ_{c}	$(32\Lambda_{\mathrm{c}}\mu D^2)/(\pi P_0W^2{\Delta_p}^{1/3})$	Unknown; values in
	Dimensionless cake attraction coefficient	range 0.1–10 used
$\bar{\phi}_{\mathrm{m}}$	$\pi/(4W^2)\int_0^D A^2dX = \pi/4\int_0^1 a^2dx$	Varies in range $0.5-0.7$,
	Membrane averaged void fraction	
β_{m}	$(8\mu D\Lambda_{\mathrm{m}}\alpha C_0)/(\pi P_0W^5G)$	Unknown; values in
	Adsorption rate coefficient	range 0.001–0.1 used
β_{c}	$(8\mu D\Lambda_{\mathrm{c}}\Delta_{\mathrm{p}}^{2/3}C_0)/(\pi P_0W^4G)$	Unknown; values in
	Cake pore shrinkage	range 0.01–1 used
ρ_{b}	Additional constant resistance when pore blocked	Unknown; values in
		range 0.2–10 used
η	$\Delta_{\mathrm{p}}/(4W^2D)$	Unknown; values in
	Cake layer thickness rate	range 0.01–1 used
κ_{c}	$32/(\pi W^2K_{\mathrm{oz}}S_{\mathrm{cp}}^2)$	Unknown; values in
	Cake permeability coefficient	range 0.1–1 used

pure water under the same applied pressure drop. The pore profiles considered are:

$$a(x,0) = \begin{cases} a_1(x,0) = 0.904 & \text{uniform initial pore profile} \\ a_2(x,0) = 0.16x + 0.83 & \text{linear increasing} \\ a_3(x,0) = 0.99 - 0.16x & \text{linear decreasing} \\ a_4(x,0) = 0.874 + .39(x-0.5)^2 & \text{convex parabola} \\ a_5(x,0) = 0.933 - 0.33(x-0.5)^2 & \text{concave parabola} \end{cases} \tag{4.53}$$

all of which correspond to the same initial net membrane resistance, $r_0 = 1.5$. In line with the discussion of Section 4.4, we note that these initial profiles also have very nearly the same initial net porosity or void fraction, $\bar{\phi}_{\mathrm{m}_0}$ (see (4.46); the

values of $\bar{\phi}_{\mathrm{m}_0}$ for each of these profiles differ by a maximum of 1.5%). We solve the model numerically for each chosen permeability profile, until the membrane becomes impermeable and the total flux through it falls to zero at final time $t = t_f$ (which happens, when the pore radius $a \to 0$ somewhere within the membrane). Our numerical scheme is straightforward, based on first-order accurate finite difference spatial discretization of the equations, with a simple implicit time step in the pore-blocking equation (4.24). We use trapezoidal quadrature in order to evaluate the necessary integrals.

Figures 4.2(a)-(e) show the pore radius $a(x,t)$, and concentrations of small particles within the membrane and the cake layer, $c_{\mathrm{m}}(x,t)$ and $c_{\mathrm{c}}(x,t)$, respectively, for each of the initial profiles given in (4.53) at various times throughout the evolution, with parameter values as given in the figure caption. A striking feature of these plots is that pore closure (accompanied by cessation of filtration) always occurs first at the upstream membrane surface, even for pores that are initially widest on that side. This phenomenon is also suggested by the particle concentration graphs, which show that most of the deposition occurs at the pore inlet. This effect becomes more pronounced at later times as the pore radius shrinks near the inlet, further enhancing the deposition there. This is consistent with the results found in Chapter 3, which did not include the effects of the cake layer. For the filtration scenarios modeled here, all large particles in the feed are captured by sieving (and later, form the cake). The graphs of $c_{\mathrm{m}}(x,t)$ and $c_{\mathrm{c}}(x,t)$ in Figure 4.2(a)-(e) demonstrate that the filter membranes are initially capturing more than 90% of small particles (by adsorption) in all cases, with this proportion increasing to nearly 100% at later times. Meanwhile, the cake layer grows to almost 10% of the membrane thickness by the end of the filtration process in all cases. The capture proportion of small particles could be adjusted by varying the parameters λ_{m} and λ_{c}: increasing them will increase the

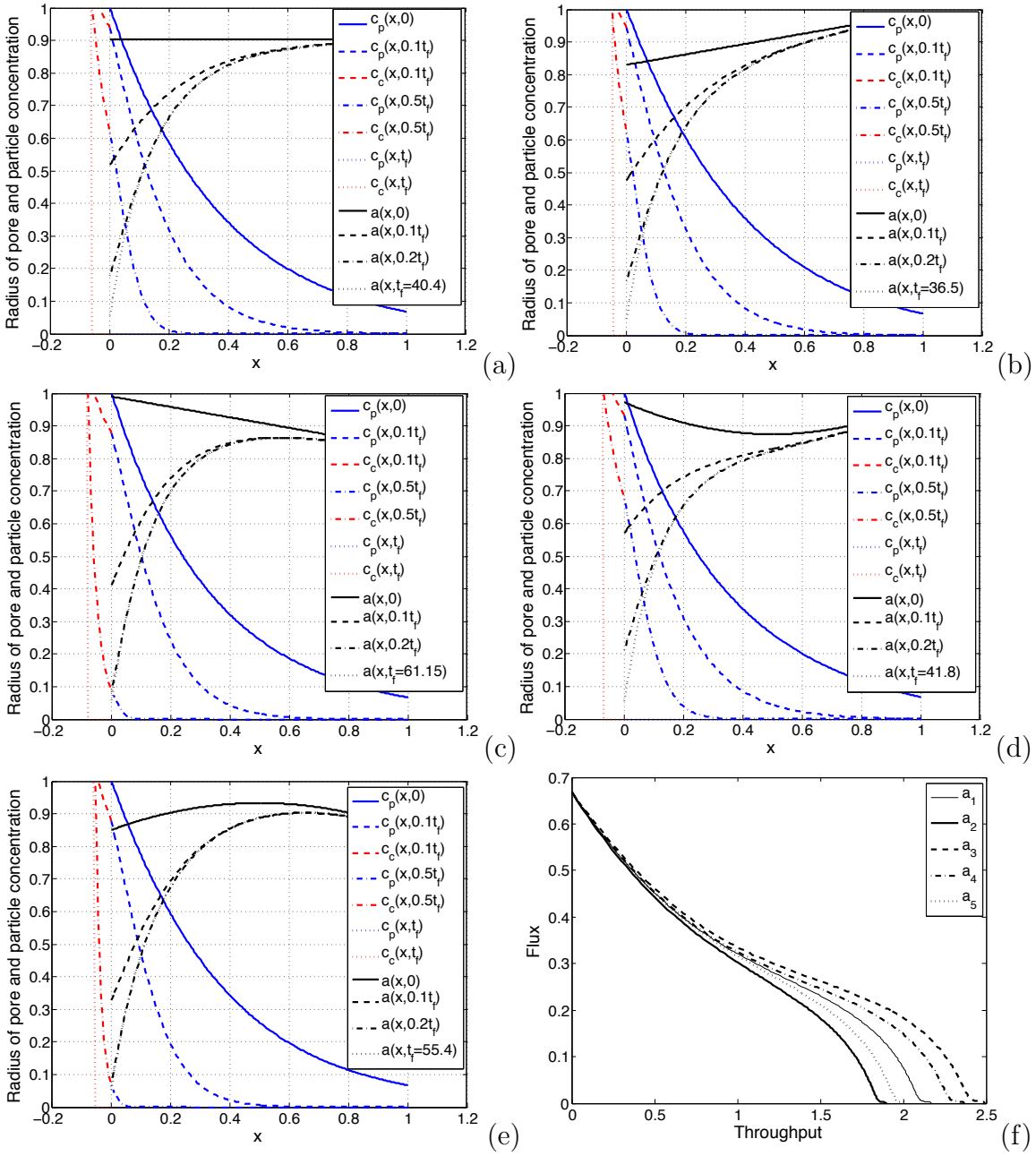

Figure 4.2 The pore radius and particle concentration at several different times up to the final blocking time (t_{f}, indicated in the legends) for different initial pore radius profiles (a-e). Figure (a) $a_1(x,0) = 0.904$, (b) $a_2(x,0) = 0.16x + 0.82$, (c) $a_3(x,0) = 0.98 - 0.16x$, (d) $a_4(x,0) = 0.87 + .39(x-0.5)^2$, (e) $a_5(x,0) = 0.93 - 0.33(x-0.5)^2$. (f) shows total flux vs throughput for those initial pore radius profiles with $\lambda_{\mathrm{m}} = 2$, $\lambda_{\mathrm{c}} = 0.5$, $\beta_{\mathrm{m}} = 0.1$, $\beta_{\mathrm{c}} = 0.1$, $\rho_{\mathrm{b}} = 2$, $\kappa_{\mathrm{c}} = 1$ and $\eta = 0.05$.

proportion of small particles captured in the membrane and cake layers, respectively, and vice-versa. These effects are discussed further below.

A common experimental characterization of membrane filtration performance is to plot a graph of total flux through the membrane at any given time ($q(t) = \int_0^1 u(x,t)dx$) versus the total volume of filtrate processed at that time (throughput, defined by $\int_0^t q(t')dt'$); the so-called flux–throughput graph for the membrane. We plot these curves, for each of the five pore profiles considered, in Figure 4.2(f). Our results are broadly consistent with those of Chapter 3 ([48]), which accounts for only blocking and adsorptive fouling. The graphs demonstrate that, although all pore profiles compared have the same initial average membrane resistance (and almost the same porosity or void fraction), they exhibit significant differences in performance. In particular, membranes whose pores are widest on the upstream side give notably better performance overall according to this performance measure, with more volume processed under the same conditions. The membrane with the least total throughput is that whose pores are initially narrowest on the upstream side (pore profile $a_2(x)$ in (4.53)). Furthermore, we see that the flux-throughput curves are initially concave, becoming convex only as total system blockage is approached as observed in Chapter 3 and also in [21]. With a careful look at the very late stages of filtration for all initial pore profiles, we see that the cake layer effects a final change of the flux-throughput curve to concave again, seen as a gradual asymptote of the flux to zero, as discussed by Griffiths *et al.* [23].

It is of interest to study the effects of cake layer model parameters (parameters associated with the other two fouling mechanisms were investigated in detail in Chapter 3), on membrane filter performance. In Figure 4.3(a), the influence of the dimensional particle-particle attraction coefficient Λ_c (while other parameters are fixed) is shown for the uniform initial pore profile $a_1(x,0) = 0.904$. According to Table 4.2, the dimensionless cake pore shrinkage rate $\beta_c = 8\mu D\Lambda_c\Delta_p^{2/3}C_0/(\pi P_0 W^4 G)$ and

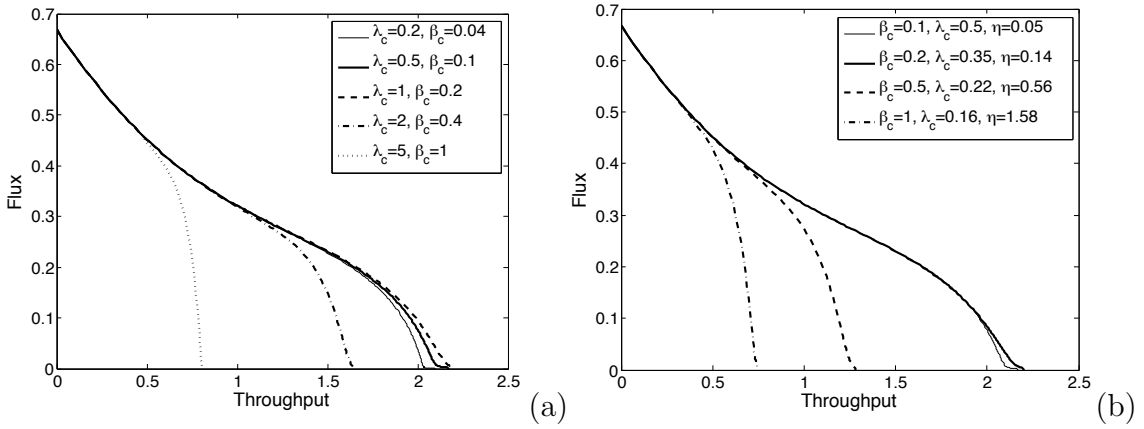

Figure 4.3 Flux versus throughput for uniform initial pore profile $a_1(x,0) = 0.904$, (a) for several different values of λ_c and β_c, we set $\lambda_c \propto \beta_c$ (corresponding to varying the dimensional particles attraction coefficient Λ_c), with $\lambda_m = 2$, $\beta_m = 0.1$, $\rho_b = 2$ and $\kappa_c = 1$. and (b) for several different values of β_c, η and λ_c , we set $\beta_c \propto \lambda_c^{-2} \propto \eta^{2/3}$ (corresponding to varying the dimensional effective particle concentration Δ_p, see (4.30), (4.31) and (4.4)), with $\lambda_m = 2$, $\beta_m = 0.1$, $\rho_b = 2$ and $\kappa_c = 1$.

the dimensionless particle-particle attraction coefficient $\lambda_c = 32\Lambda_c\mu D^2/(\pi P_0 W^2 \Delta_p^{1/3})$ both depend on Λ_c, therefore β_c and λ_c must each be changed proportional to Λ_c as it varies. Our results illustrate that filter throughput initially increases as β_c and λ_c but will decreases for larger values of β_c and λ_c. Furthermore, Figure 4.3(b) demonstrates the significance of the non-dimensional cake pore shrinkage rate β_c on filter membrane performance for the same uniform initial pore profile $a_1(x,0) = 0.904$, when another dimensional model parameter changes. Here we consider the membrane features fixed and focus on the influence of the solvent on the filtration process by changing the dimensional effective large-particle size Δ_p. Again as shown in Table 4.2, variation of Δ_p does not affect only β_c; the dimensionless small/large particle attraction coefficient λ_c, and the dimensionless cake growth coefficient $\eta = \Delta_p/(4W^2D)$ also change. The results simply show that the filter performance decreases as Δ_p increases.

Figure 4.4(a) demonstrates the evolution of the cake layer until flux through the membrane falls to zero for all initial pore profile given in (4.53). Our results here generally show that cake layer grows at a steady rate in its initial stages of

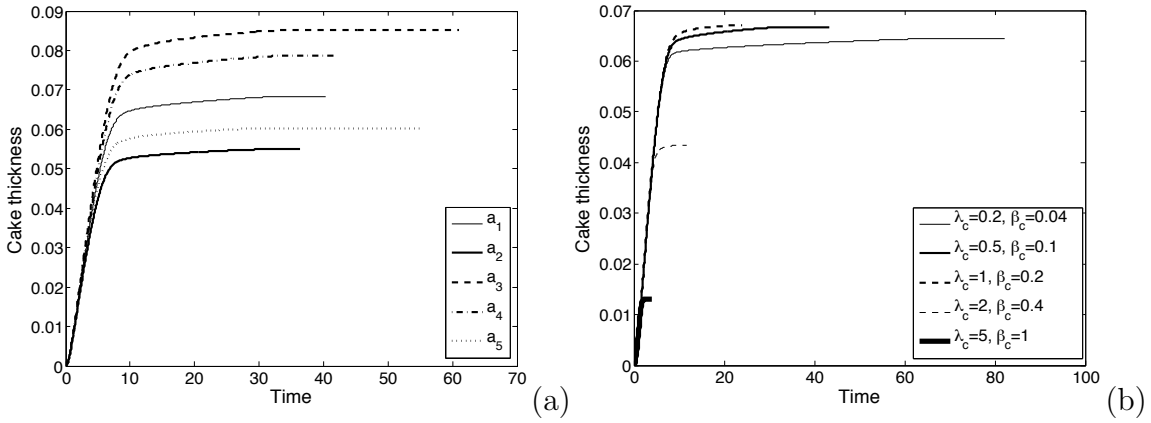

Figure 4.4 (a) Cake thickness versus time for all five initial pore profiles in (4.53), with $\lambda_{\rm m} = 2$, $\lambda_{\rm c} = 0.5$, $\beta_{\rm m} = 0.1$, $\beta_{\rm c} = 0.1$, $\rho_{\rm b} = 2$, $\kappa_{\rm c} = 1$ and $\eta = 0.05$; and (b) cake thickness versus time, for the uniform initial pore profile $a_1(x, 0) = 0.904$ for several different values of $\lambda_{\rm c}$ and $\beta_{\rm c}$ ($\lambda_{\rm c} \propto \beta_{\rm c}$), with $\lambda_{\rm m} = 2$, $\beta_{\rm m} = 0.1$, $\rho_{\rm b} = 2$, $\kappa_{\rm c} = 1$ and $\eta = 0.05$.

formation, but at the late stages, as the flux through the membrane decreases (due to the significant fouling) the rate of growth of the cake layer thickness decreases, until the membrane clogs completely. (Note that in practice a filter would be discarded well before this final, very slow (low flux), stage leading to total clogging.) As shown in Figure 4.4(a), the final time of filtration process varies with the initial pore profile and among the profiles in (4.53), the maximum and minimum belong to a_3 and a_2; respectively (in other words, the total filtration process is longer/shorter for the membrane with wider/narrower pores at the upstream). Furthermore, our results show that the thickness of cake layer for membranes with initial pore profiles given in (4.53) is less than 10% of membrane thickness, which is consistent with our observation in Figures 4.2(a-e).

Figure 4.4(b) shows effects of variation of dimensional particles attraction coefficient $\Lambda_{\rm c}$, on the cake layer thickness for the uniform initial pore profile $a_1(x, 0) = 0.904$. Again as shown in Table 4.2, both $\lambda_{\rm c}$ and $\beta_{\rm c}$ change proportional to $\Lambda_{\rm c}$. The results show that the cake layer thickness initially increases as $\Lambda_{\rm c}$ increases but eventually decreases for larger values of $\lambda_{\rm c}$ and $\beta_{\rm c}$.

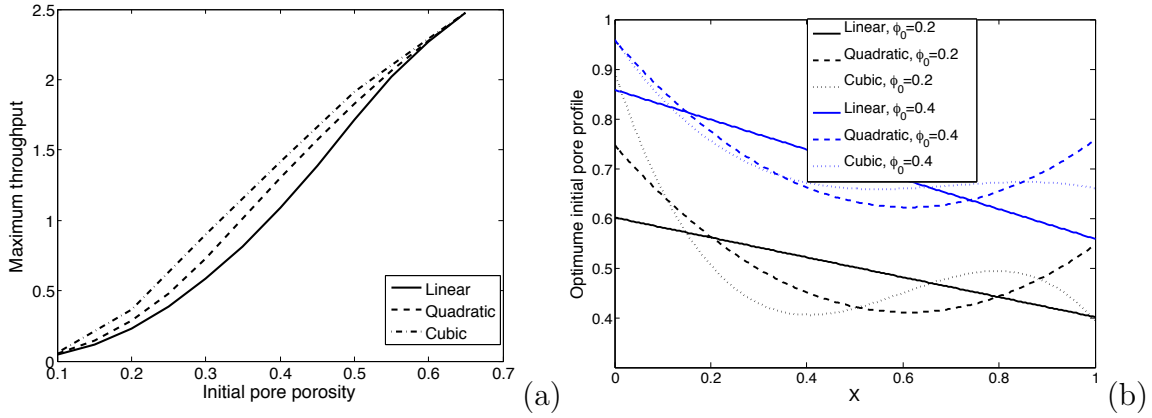

Figure 4.5 (a) Maximum throughput versus initial pore porosity with linear, quadratic and cubic initial pore profiles, and (b) optimum linear, quadratic and cubic pore profile for initial pore porosities $\bar{\phi}_{\mathrm{m}_0} = 0.2$ and 0.4 (defined in (4.46)), with $\lambda_{\mathrm{m}} = 2$, $\lambda_{\mathrm{c}} = 0.5$, $\beta_{\mathrm{m}} = 0.1$, $\beta_{\mathrm{c}} = 0.1$, $\rho_{\mathrm{b}} = 2$, $\kappa_{\mathrm{c}} = 1$ and $\eta = 0.05$.

Pore profile optimization study

As discussed in Section 4.4, manufacturers are interested to find the optimal pore profile as a function of depth through the membrane. Here we present a brief study on how to approach this general optimization problem, focusing on the class of polynomial membrane pore profiles. As was mentioned earlier in Section 4.4, membranes of the same initial net porosity have very nearly the same net resistance, therefore we present our results here versus net porosity rather than net resistance. Figure 4.5(a) illustrates our results, plotting maximum throughput versus initial pore porosity $\bar{\phi}_{\mathrm{m}_0} = \pi/4 \int_0^1 a(x,0)^2 dx$ for linear, quadratic and cubic initial pore profiles. Though we here consider only low-order polynomials, our results indicate that in the intermediate porosity range, increasing the order of the polynomial describing the pore shape can lead to a reasonable increase (over 10%) in total throughput. (Total throughput can only increase as the degree of the polynomial is increased, as a polynomial of degree n is a special case of a polynomial of degree $n+1$). It is observed, however, that when initial pore porosity is small (close to zero) or large (close to $\pi/4$) the performance is almost independent of the polynomial degree. In addition, for fixed initial porosity, the difference between maximum throughput for

quadratic and cubic initial pore profiles is slightly less than the difference between the maximum throughput for linear and quadratic initial pore profiles, hinting (as would be expected) at a convergence of performance to some global optimum as the degree of the approximating polynomial is increased.

The shapes of some optimum initial pore profiles in the class of linear, quadratic and cubic polynomials are shown in Figure 4.5(b) for selected initial pore porosities $\bar{\phi}_{\mathrm{m}_0} = 0.2$ and 0.4 (we chose these values in order to distinguish the graphs easily). Consistent with the observations of Figure 4.2(f), the optimal profile among all of the three initial profiles, is widest at the upstream membrane surface (the cubic profile). Note that as the initial dimensionless porosity increases, the shape of the optimal initial pore profile converges to the linear one. Since most membranes in widespread use are rather permeable, these results suggest that, even though membrane pore morphology is very complex in reality, optimizing only within the restricted class of linear pore profiles should provide a reasonable guide: consideration of a larger class of pore profiles yields only marginal improvements.

CHAPTER 5

MEMBRANE FILTRATION WITH COMPLEX BRANCHING PORE MORPHOLOGY

5.1 Introduction

The goal of the present chapter is to extend the scope of the work outlined in Chapter 3, deriving a general pore branching model that accounts for a wide range of membrane internal geometries, and that allows for fouling by particle adsorption within pores. The chapter is laid out as follows: in Section 5.2, we introduce a mathematical model for flow through a membrane with internal branching structure, and propose the adsorptive fouling model (a semi-discrete version of our earlier continuum model in Chapter 3 ([48])). In Section 5.3, we introduce appropriate scalings and nondimensionalize the model. Sample simulations, which demonstrate the important effects of pore geometry and branching features, are presented in Section 5.4. Finally, we conclude in Section 5.5 with a discussion of our model and results in the context of real membrane filters.

5.2 Mathematical Modeling

The modeling throughout this chapter (as in Chapter 3) assumes that the membrane is flat and lies in the (Y, Z)-plane, with unidirectional Darcy flow through the membrane in the positive X-direction. The membrane properties and flow are assumed homogeneous in the (Y, Z)-plane, but membrane structure may vary internally in the X-direction (depth-dependent permeability) thus we seek a solution in which properties vary only in X and in time T. Throughout this section, we use uppercase fonts to denote dimensional quantities; lowercase fonts, introduced in Section 5.3, will be dimensionless.

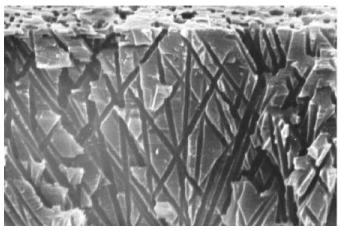
(a)
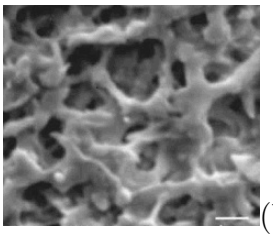
(b)

Figure 5.1 Magnified membranes with various pore distributions and sizes ((a) is from [4], (b) is from [27]). Photograph (b) has width 10 μm.

As discussed in Chapter 3, the superficial Darcy velocity $\mathbf{U} = (U(X,T), 0, 0)$ within the membrane is given in terms of the pressure P by

$$U = -\frac{K(X,T)}{\mu}\frac{\partial P}{\partial X}, \quad \frac{\partial}{\partial X}\big(K(X,T)\frac{\partial P}{\partial X}\big) = 0, \quad 0 \le X \le D, \tag{5.1}$$

where $K(X,T)$ is the membrane permeability at depth X and D is the thickness of membrane. Two driving mechanisms are used in applications: (i) constant pressure drop across the membrane specified; and (ii) constant flux through the membrane specified. In the former case, the flux will decrease in time as the membrane becomes fouled; in the latter, the pressure drop required to sustain the constant flux will rise as fouling occurs. We will focus on case (i) in this chapter, and so assume this in the following model description. With constant pressure drop P_0, the boundary conditions on the pressure are

$$P(0,T) = P_0, \quad P(D,T) = 0. \tag{5.2}$$

In this chapter, we consider only one of the three fouling mechanisms described earlier: fouling due to particle adsorption within the membrane pores (also known as "standard blocking"). Though pore-blocking and cake formation are not difficult to incorporate in our model, including them here will make it harder to draw firm conclusions about the effects of pore branching, hence we leave these for a future study. We consider a feed solution containing small particles (much smaller than the pore diameter), which are transported down pores and may be deposited on the internal

pore walls. In Chapter 3 (also see [48]), we modeled the filter membrane as a periodic lattice of identical axisymmetric pores, which traverse the membrane from upstream to downstream side, with radius varying in the depth of the membrane. In reality, as noted before, most membranes have a much more complex structure: Figure 5.1 shows just two examples of filter membrane cross-sections. Many membranes have depth structure that varies from large pores on the upstream side to much smaller pores on the downstream side, and large pores may branch into several smaller pores as the membrane is traversed. To begin to address this type of complexity, we will construct a simplified model in which a membrane consists of units that repeat periodically in the plane of the membrane in a square lattice pattern, with period $2W$. Within each lattice unit, we assume that the membrane has a layered structure, exemplified by the sketch in Figure 5.2: here the period-unit consists of a single circularly-cylindrical pore on the upstream side which, after a distance D_1, bifurcates into smaller tubes (pores). Each of these then undergoes further bifurcation after distance D_2, and so on. This sequence of divisions generates a membrane with m layers, each layer containing twice as many pores as the previous layer. Clearly, many possible variants on this basic scenario could be imagined, including pores that recombine downstream: our model will readily generalize to other cases. We will consider two scenarios in this chapter: (i) a symmetric branching model, in which the pores within each layer are identical; and (ii) an asymmetric branching model. We will focus primarily on case (i) in this chapter and outline the model in detail in Section 5.2.1 below; our description for the asymmetric branching model requires minor modifications, shown in Section 5.2.2.

5.2.1 Symmetric Branching Model

In this case, we consider all pores within a given layer to be identical, circularly-cylindrical, and perpendicular to the plane of the membrane. A simple case with 3

layers is schematized in Figure 5.2: each branching unit is assumed to stem from a single pore on the upstream surface. Ignoring the effect of the short pore regions that are not perpendicular to the membrane, this layered structure can be modeled using the Hagen-Poiseuille model: an individual pore in layer i of radius A_i has resistance per unit length $R_i = 8/(\pi A_i^4)$. Within a branching unit the mth layer contains M_i pores, and has depth D_i (for the case where only bifurcations of pores are allowed, $M_i = 2^{i-1}$). Mass conservation shows that the averaged pore velocity in the ith layer, $\bar{U}_{\mathrm{p},i}$ (the cross-sectionally averaged axial velocity within each pore in layer i), satisfies

$$\frac{\partial(\pi A_i^2 \bar{U}_{\mathrm{p},i})}{\partial X} = 0. \tag{5.3}$$

Assuming a uniform pressure gradient across each layer (equivalent to the assumption that pores have uniform radius within each layer), the Darcy velocity U_i in the ith layer satisfies, approximately (defining $D_0 = 0$ for convenience),

$$(2W)^2 U_i(X) = -\frac{M_i}{\mu R_i}\frac{P_i - P_{i-1}}{D_i}, \quad \sum_{j=0}^{i-1} D_j \le X \le \sum_{j=1}^{i} D_j,\ 1 \le i \le m, \tag{5.4}$$

where P_i ($1 \le i \le m-1$) are the unknown inter-layer pressures within the membrane (P_0 is the specified driving pressure and $P_m = 0$). By continuity, all U_i must be equal to the global Darcy velocity U, hence (5.4) represents m equations for U and the unknown P_i. Solving successively for P_i we obtain

$$(2W)^2 U = \frac{P_0}{\mu R}, \quad \text{where} \quad R = \sum_{i=1}^{m} \frac{D_i R_i}{M_i} \quad \text{and} \quad R_i = \frac{8}{\pi A_i^4}. \tag{5.5}$$

Equation (5.5) is an expression that captures the net resistance R of the microstructured membrane. Note that the superficial Darcy and cross sectionally averaged pore velocities for each layer are related by

$$(2W)^2 U = \pi M_i A_i^2 \bar{U}_{\mathrm{p},i}, \quad 1 \le i \le m, \tag{5.6}$$

by a simple flux-balance argument, consistent with (5.1) and (5.3).

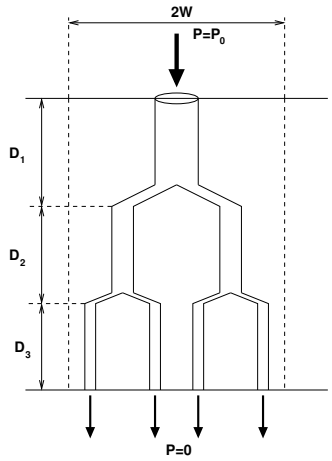

Figure 5.2 Symmetric branching structure with 3 layers ($m = 3$), of thicknesses D_1, D_2, D_3 and specified pressure drop $P = P_0$.

The model outlined above gives a reasonable description of Darcy flow through a membrane with the specified microstructure, but says nothing about fouling of such a membrane. Our fouling model is similar in spirit to some of Chapter 3 (also see [48]), which used careful averaging over the pore cross-section to derive an advection equation for the concentration of small particles within the pores, with a sink term modeling the adsorption at the pore wall (details are provided in Chapter 3). The direct analog of that model for pores in each sub-layer of the membrane is

$$\bar{U}_{\mathrm{p,i}} \frac{\partial C_i}{\partial X} = -\Lambda \frac{C_i}{A_i}, \quad \sum_{j=0}^{i-1} D_j \leq X \leq \sum_{j=1}^{i} D_j,\ 1 \leq i \leq m, \tag{5.7}$$

where C_i is the particle concentration in the pores of the ith layer, to be solved subject to specified particle concentration at the inlet,

$$C_0(T) = C_0, \tag{5.8}$$

and continuity of particle concentration from one layer to the next, $C_i(T) = C_{i+1}(T)$. The (dimensional) constant Λ captures the physics of the attraction between particles and wall that is causing the deposition (for details see Appendix B). The pore radius

in each layer shrinks in response to the deposition according to

$$\frac{\partial A_i}{\partial T} = -\Lambda \alpha C_i, \quad 1 \leq i \leq m, \tag{5.9}$$

for some constant α (related to the particle size), which simply assumes that the pore cross-sectional area shrinks at a rate given by the total area of particles deposited locally. The initial pore radii are specified throughout the membrane,

$$A_i(X,0) = A_{i,0}, \quad \sum_{j=0}^{i-1} D_j \leq X \leq \sum_{j=1}^{i} D_j, \quad 1 \leq i \leq m, \tag{5.10}$$

where $A_{i,0}$ is the (constant, specified) initial radius of the pore in the ith layer.

In a membrane with many layers, the above system can be time consuming to solve numerically. However, in such situations we anticipate that the length of pores between successive bifurcations is short relative to the typical lengthscale of gradients in C_i (estimated from (5.7)), corresponding to an assumption that $32\Lambda\mu D^2/(\pi P_0 W^3) \ll 1$. We thus propose a simplified model using (5.7), in which C_i is piecewise constant in X, changing its value only at pore bifurcations (so we no longer enforce continuity at the boundary between adjacent layers). This assumption also implies that A_i will be independent of X (see (5.9)). A simple finite-difference approximation of (5.7) gives

$$\bar{U}_{\mathrm{p,i}} \frac{C_i - C_{i-1}}{D_i} = -\Lambda \frac{C_i}{A_i}, \quad 1 \leq i \leq m, \tag{5.11}$$

where the cross-sectionally averaged axial velocity within each pore in layer i, $\bar{U}_{\mathrm{p},i}$, is given by (5.5) and (5.6) as

$$\bar{U}_{\mathrm{p},i} = \frac{P_0}{\pi \mu M_i A_i^2 R}, \quad 1 \leq i \leq m. \tag{5.12}$$

This allows the particle concentration C_i in the pores of the ith layer to be expressed in terms of the concentration in the previous layer as

$$C_i = \frac{\bar{U}_{\mathrm{p},i} C_{i-1}}{\bar{U}_{\mathrm{p},i} + \Lambda D_i / A_i}, \quad 1 \leq i \leq m. \tag{5.13}$$

As noted previously, this model describes the case of fouling by standard blocking (particle adsorption) only.

5.2.2 Asymmetric Branching Model

The model above has the simplifying feature that all pores in a given layer are identical initially and thus, given the deterministic nature of our fouling model, remain so at later times. Real membranes do not possess such symmetry, hence we now formulate a more realistic model in which pores in the same layer are non-identical. The same basic layered structure is assumed however, in which a single pore at the upstream surface bifurcates into two smaller (non-identical) tubes after distance D_1, and so on. The sequence of divisions generates a membrane with m layers, each containing twice as many pores as the previous one; thus there are again $M_i = 2^{i-1}$ pores in layer i. These pores in general all have different radii, which we denote by A_{ij}, $1 \leq j \leq 2^{i-1}$ (the radius of the jth pore in layer i). The pressures at either end of this pore will be P_{ij} at the downstream end, and $P_{i-1,[j+1/2]}$ [1] at the upstream end (see Figure 5.3 for a simple schematic in the case of 3 layers). In the first layer $i = 1$, there is just one pore of radius A_{11}, with upstream pressure $P_{01} = P_0$ specified. $\bar{U}_{p,ij}$ represents the cross sectionally averaged velocity of the fluid in the jth pore in layer i, and satisfies, approximately,

$$\pi A_{ij}^2 \bar{U}_{\mathrm{p},ij} = -\frac{1}{\mu R_{ij}} \frac{P_{ij} - P_{i-1,[\frac{j+1}{2}]}}{D_i}, \quad 1 \leq i \leq m, \quad 1 \leq j \leq 2^{i-1}, \tag{5.14}$$

[1] The floor function $[x]$ is the greatest integer less than or equal to x.

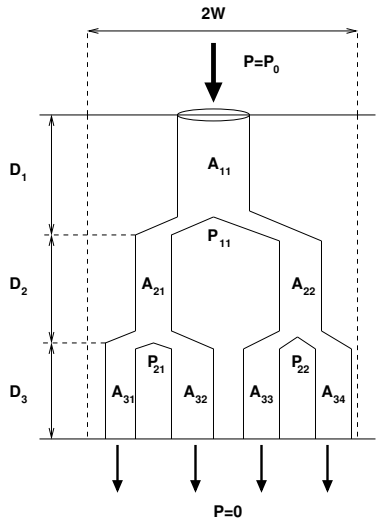

Figure 5.3 Asymmetric branching structure with 3 layers ($m = 3$), thicknesses D_1, D_2, D_3, and specified pressure drop $P = P_0$. The radius of the jth pore in layer i and the pressure at the downstream end of this pore are A_{ij} and P_{ij}, respectively.

where $R_{ij} = 8/(\pi A_{ij}^4)$ is the resistance per unit length of the jth pore in layer i. By a simple flux balance argument, the superficial Darcy velocity, U, across the membrane is related to the pore velocities in each layer by

$$(2W)^2 U = \pi A_{11}^2 \bar{U}_{\mathrm{p},11},$$

$$\pi A_{ij}^2 \bar{U}_{\mathrm{p},ij} = \pi A_{i+1,2j-1}^2 \bar{U}_{\mathrm{p},i+1,2j-1} + \pi A_{i+1,2j}^2 \bar{U}_{\mathrm{p},i+1,2j}, \quad 1 \le i \le m-1,\, 1 \le j \le 2^{i-1}. \tag{5.15}$$

If the pore radii are specified then equations (5.14), (5.15) represent $2^m + 2^{m-1} - 1$ equations in $2^m + 2^{m-1} - 1$ unknowns, consisting of U, $\bar{U}_{\mathrm{p},ij}$ $(1 \le i \le m,\, 1 \le j \le 2^{i-1})$ and P_{ij} $(1 \le i \le m-1,\, 1 \le j \le 2^{i-1})$, hence they can be solved. Consistent with the adsorption fouling model proposed in (5.13) we now have

$$C_{ij} = \frac{\bar{U}_{\mathrm{p},ij} C_{i-1,[\frac{j+1}{2}]}}{\bar{U}_{\mathrm{p},ij} + \Lambda D_i / A_{ij}}, \quad \frac{\partial A_{ij}}{\partial T} = -\Lambda \alpha C_{ij}, \quad 1 \le i \le m, \quad 1 \le j \le 2^{i-1}, \tag{5.16}$$

where C_{ij} is the average particle concentration of the jth pore in layer i. We solve the model (5.14), (5.15) and (5.16) subject to $C_{01} = C_0$, $P_{01} = P_0$, $P_{mj} = 0$ for $1 \le j \le 2^{m-1}$, with $A_{ij}(0)$ for $1 \le i \le m$, $1 \le j \le 2^{i-1}$ all specified.

5.3 Scaling and Nondimensionalization

Symmetric Branching Model:

We nondimensionalize the model (5.2)–(5.12), using the scalings

$$P_i = P_0 p_i, \quad (X, D_i) = D(x, d_i), \quad C_i = C_0 c_i, \quad A_i = W a_i,$$
$$(U, \bar{U}_{\mathrm{p},i}) = \tfrac{\pi W^2 P_0}{32\mu D}(\hat{u}, \hat{\bar{u}}_{\mathrm{p},i}), \quad T = \tfrac{W}{\Lambda \alpha C_0} t, \tag{5.17}$$

where $D = \sum_{i=1}^{m} D_i$ is the membrane thickness. This gives the following dimensionless model for $\hat{u}(t)$, $\hat{\bar{u}}_{\mathrm{p},i}(t)$, $p_i(t)$, $a_i(t)$, $c_i(t)$ (dimensionless Darcy velocity, cross-sectionally averaged pore velocity, inter-layer pressures, pore radii and cross-sectionally averaged particle concentration in the ith layer, respectively):

$$\hat{u} = \frac{1}{\sum_{i=1}^{m} d_i/(M_i a_i^4)}, \quad \hat{u} = \frac{\pi}{4} M_i a_i^2 \hat{\bar{u}}_{\mathrm{p},i}, \tag{5.18}$$

$$c_i = \frac{\hat{\bar{u}}_{\mathrm{p},i} c_{i-1}}{\hat{\bar{u}}_{\mathrm{p},i} + \hat{\lambda} d_i / a_i}, \quad \hat{\lambda} = \frac{32 \Lambda \mu D^2}{\pi P_0 W^3}, \tag{5.19}$$

$$\frac{\partial a_i}{\partial t} = -c_i, \tag{5.20}$$

with boundary and initial conditions

$$c_0(t) = 1, \quad a_i(0) = a_{0i}, \quad p_0(t) = 1, \quad p_m(t) = 0, \tag{5.21}$$

where $1 \le i \le m$, and $a_{0i} \in (0, 1)$ are specified.

Using equation (5.18), one can define a dimensionless membrane resistance $\hat{r}(t)$ consistent with (5.5), as

$$\hat{r}(t) = \sum_{i=1}^{m} \frac{d_i}{M_i a_i^4(t)}, \tag{5.22}$$

Note that, while this definition is in a sense "natural", typically it leads to very large values for $\hat{r}$ and as a consequence, very small values for $\hat{u} = 1/\hat{r}$, specifically in the membrane with many layers and tiny branches in the downstream. Our initial choice for the scalings in (5.17) makes sense based on a single pore (see Chapter 3 ([48])) but is not appropriate for a system with multiple layers and branching. Hence, we make a further rescaling based on a typical value, $\hat{r}_0$, of the resistance as defined in (5.22). In most cases we may take $\hat{r}_0$ to be the initial dimensionless resistance, since we will often compare equal resistance systems (see Section 5.4 later). Therefore, we define

$$r = \frac{\hat{r}}{\hat{r}_0}, \quad u = \hat{r}_0 \hat{u}, \quad \lambda = \hat{\lambda} \hat{r}_0, \tag{5.23}$$

where r, u and λ are the new dimensionless resistance, Darcy velocity and particle-wall attraction coefficient, respectively. Using these new scalings, (5.18), (5.19) and (5.22) give

$$r(t) = \frac{1}{\hat{r}_0} \sum_{i=1}^{m} \frac{d_i}{M_i a_i^4(t)}, \tag{5.24}$$

$$u = \frac{1}{r}, \quad u = \frac{\pi}{4} M_i a_i^2 \bar{u}_{\mathrm{p},i}, \tag{5.25}$$

$$c_i = \frac{\bar{u}_{\mathrm{p},i} c_{i-1}}{\bar{u}_{\mathrm{p},i} + \lambda d_i / a_i}, \quad \lambda = \frac{32 \Lambda \mu D^2 \hat{r}_0}{\pi P_0 W^3}, \tag{5.26}$$

while (5.20) and (5.21) still hold.

Asymmetric Branching Model:

We nondimensionalize the model (5.14)–(5.16), using the same scalings in (5.17) and (5.23), giving the following dimensionless model for $u(t)$, $\bar{u}_{\mathrm{p},ij}(t)$, $p_{ij}(t)$, $a_{ij}(t)$, $c_{ij}(t)$ (dimensionless Darcy velocity, cross-sectionally averaged pore velocity, inter-layer pressures, pore radii and cross-sectionally averaged particle concentration within the jth pore in layer i, respectively):

$$4u = \pi a_{11}^2 \bar{u}_{\mathrm{p},11}, \quad a_{ij}^2 \bar{u}_{\mathrm{p},ij} = a_{i+1,2j-1}^2 \bar{u}_{\mathrm{p},i+1,2j-1} + a_{i+1,2j}^2 \bar{u}_{\mathrm{p},i+1,2j}, \tag{5.27}$$

$$\bar{u}_{\mathrm{p},ij} = -\frac{4}{\pi} a_{ij}^2 \frac{p_{ij} - p_{i-1,[\frac{j+1}{2}]}}{d_i}, \tag{5.28}$$

$$c_{ij} = \frac{\bar{u}_{\mathrm{p},ij} c_{i-1,j}}{\bar{u}_{\mathrm{p},ij} + \lambda d_i / a_{ij}}, \quad \lambda = \frac{32 \Lambda \mu D^2 \hat{r}_0}{\pi P_0 W^3}, \tag{5.29}$$

$$\frac{\partial a_{ij}}{\partial t} = -c_{ij}, \tag{5.30}$$

where $1 \le i \le m$, $1 \le j \le 2^{i-1}$. We solve the model (5.27)–(5.30) subject to boundary and initial conditions

$$c_{01}(t) = 1, \quad a_{ij}(0) = a_{0ij}, \quad p_{01}(t) = 1, \quad p_{mj} = 0 \quad \text{for} \quad 1 \le j \le 2^{m-1}, \tag{5.31}$$

where $0 < a_{0ij} < 1$ are specified.

5.4 Results

In this section, we present some simulations of the models (5.20), (5.21), (5.24)–(5.26) and (5.27)–(5.31) described in Section 5.3 above, paying particular attention to how results depend on the branch configuration. Our model contains only one dimensionless parameter, λ, which captures the physics of the attraction between particles and the pore wall. The value of this parameter is unknown, and may vary

widely between systems depending on the detailed structure of the filter membrane and on the nature of the feed solution. In the absence of firm data we take $\lambda = 30$ for most simulations, and briefly investigate the effect of varying λ later in Figure 5.6.

We present results first for the case of symmetric branching (model (5.20), (5.21), (5.24)–(5.26)) before turning our attention to the more complex asymmetric branching model (equations (5.27)–(5.31)).

5.4.1 Symmetric Branching Model Results

For simplicity, we consider all of the layers to be equally spaced, therefore $d_i = 1/m$. As noted previously, for the simple "bifurcating pore" model $M_i = 2^{i-1}$ for $1 \leq i \leq m$, therefore (5.24) gives

$$r(t) = \sum_{i=1}^{m} \frac{1}{m 2^{i-1} a_i^4(t)}. \tag{5.32}$$

In order to make a meaningful comparison, we run simulations for pore structures that have the same initial membrane resistance $r_0 = r(0)$. This means that we are comparing membranes that perform identically when no fouling occurs – they would give identical performances when filtering pure water under the same applied pressure drop.

Furthermore, in order to keep the number of variable parameters small, we assume that initial pore radius decreases geometrically in the depth of membrane; that is, we take $a_{0i} = a_1(0)\kappa^{i-1}$ to be the radius of the pores in the ith layer, where $a_1(0)$ is the initial radius of the pore in the first layer and κ is the geometric ratio. Therefore, by fixing the initial resistance r_0 (as defined by (5.32)) and varying the geometric coefficient κ, we can investigate a wide range of membrane morphologies (the radius of the pore in the top layer will be fixed for each κ-value chosen, since $r(0) = r_0$ is specified; specifically, as κ increases, the initial pore radius in the top

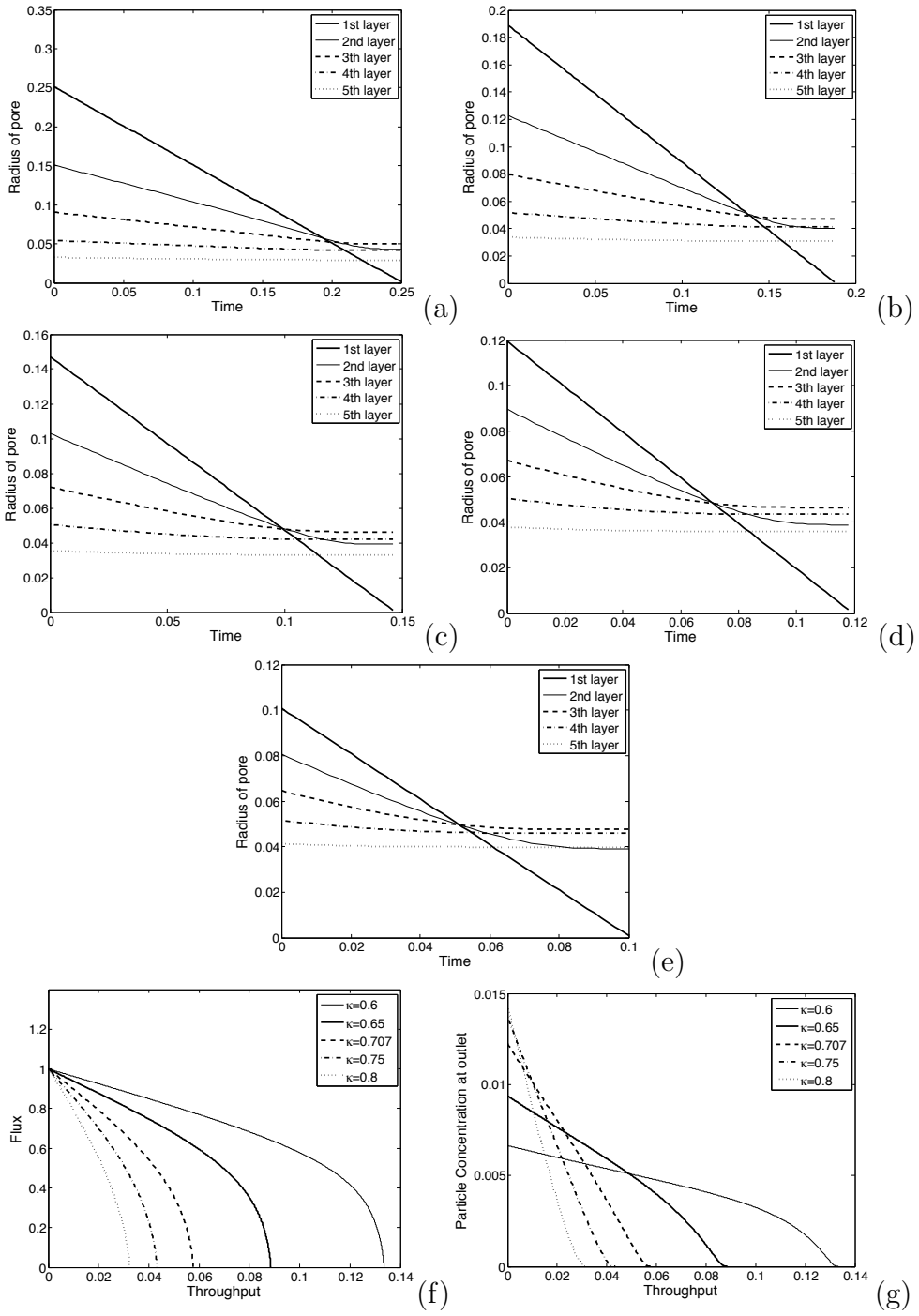

Figure 5.4 Symmetric branching model: The pore radius evolution in each layer (indicated in the legends) with the same initial resistance $r_0 = 1$, when the initial radius of the pores in the layers are geometrically decreasing, for different geometric coefficient κ: (a) 0.6, (b) 0.65, (c) 0.707, (d) 0.75, (e) 0.8. (f) and (g) show total flux and particle concentration at outlet vs throughput; respectively, for these geometric coefficients with $\lambda = 30$ and $m = 5$.

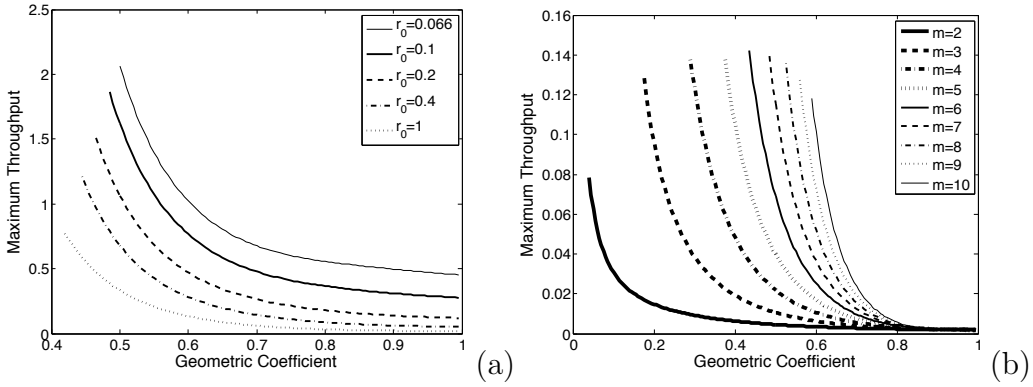

Figure 5.5 Maximum throughput versus geometric coefficient κ with $\lambda = 30$, (a) for several different values of dimensionless initial resistance r_0 with number of layers $m = 5$ (b) for several different number of layers m in symmetric branching configurations with $r_0 = 6.66$.

layer must decrease and vice-versa, in order to keep the total membrane resistance fixed).

The main results are shown in Figure 5.4: we simulate the model (5.20), (5.21), (5.24)–(5.26) for several different values of the geometric coefficient ($\kappa = 0.6$, 0.65, 0.7, 0.75 and 0.8), with parameter $\lambda = 30$, number of layers $m = 5$, and initial membrane resistance $r_0 = 1$. Figures 5.4 (a)-(e) show the pore radius $a_i(t)$ in each layer versus time. A striking feature of these plots is that pore closure occurs first at the upstream membrane surface layer, at least for the model parameters considered here. In addition, the closure time, which is the time at which the membrane no longer permits flow and filtration ceases (here, the time at which the first layer pore radius becomes zero), varies with the geometric coefficient. Our model predicts that the smaller the geometric coefficient, the larger the closure time; this appears to be primarily because the pore radius in the first layer is wider for a branch with a smaller geometric coefficient, and this is always the pore that closes first.

Figure 5.4 (f) shows flux-throughput graphs for the membrane structures of Figures 5.4 (a)-(e). The flux-throughput graph plots the instantaneous flux through the membrane at any given time versus the total volume of filtrate processed at that

time (throughput), and is a common experimental characterization of membrane filter performance. Since the flux is directly proportional to the averaged Darcy velocity, we define dimensionless flux for our model by $q(t) = u(0, t)$; throughput is then defined by $\int_0^t q(t')dt'$. We plot these curves, for each of the five chosen values of the geometric coefficient, in Figure 5.4(f). The graphs collectively demonstrate that, although all branch structures give the same initial average membrane resistance, they exhibit significant differences in performance over time. In particular, for the chosen model parameters, branch structures with wider pores in the top layer (upstream side) give notably better performance overall according to this performance measure, with more filtrate processed under the same conditions. The minimum total throughput is given by the branch structure with the narrowest pore on the upstream side, exhibiting rapid pore closure ($\kappa = 0.8$; this is most uniformly permeable membrane of those considered). Our results here are broadly consistent with our findings in our previous non-branching pore model in Chapter 3 (also see [48]). In Chapter 3, we also found that, with the same initial average membrane resistance, membranes whose pores are widest on the upstream side give notably better performance overall (more filtrate processed under the same conditions) and the membrane with least total throughput is that whose pores are initially narrowest on the upstream side.

Another key consideration in evaluating membrane performance is the concentration of particles remaining in the filtrate as it exits the membrane, $c_m(t) = c(1, t)$: in general a lower particle concentration at the outflow side of the membrane indicates superior separation efficiency for the filter membrane. Figure 5.4(g) plots $c_m(t)$ versus throughput for each of the given geometric coefficients. The results here are qualitatively consistent with those of the flux–throughput graphs of Figure 5.4(f); in particular, for a given "tolerance" value of the particle concentration at the outlet, membranes with narrow pores in the first layer of the branching network (or with larger geometric coeficient κ) always give less total throughput than those whose

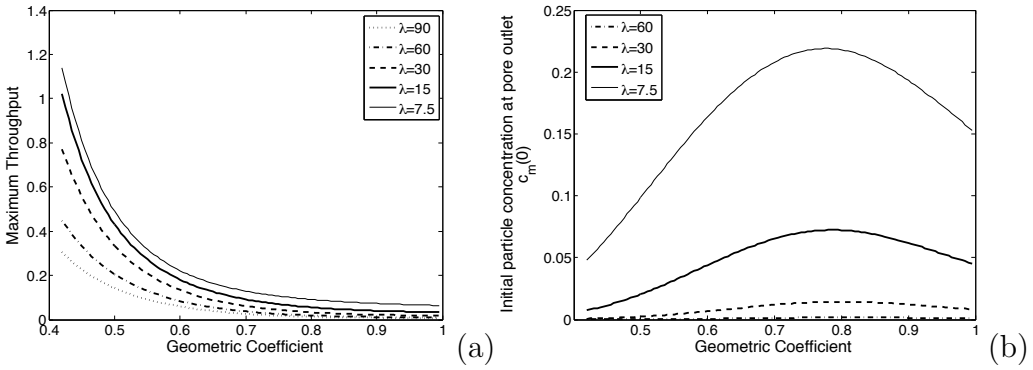

Figure 5.6 Maximum throughput (a) and initial particle concentration at pore outlet $c_m(0)$ (b) versus geometric coefficient κ for several different values of λ in symmetric branching configurations with $m = 5$ and $r_0 = 1$.

pores are wider on the upstream side (again, initial resistance is the same for all membranes compared).

Figures 5.5(a) and (b) further illustrate our results, plotting throughput versus the geometric coefficient for several different scenarios. In Figure 5.5(a) the number of layers is fixed, $m = 5$, and total throughput is plotted versus the geometric coefficient, for several different values of the membrane resistance r_0. Note that at low membrane resistance, where pores must be large, the range of realizable geometric coefficients is limited. Needless to say, as initial membrane resistance increases, the performance of the filter (as measured by total throughput) decreases. Consistent with our results in Figure 5.4 for fixed initial resistance, a larger geometric coefficient results in less total throughput.

In Figure 5.5(b), the dimensionless initial resistance is fixed at $r_0 = 6.66$, and throughput is again plotted as a function of geometric coefficient for several different values of m (the number of layers in the structure). Note that, with the assumed form of the branching geometry, a structure with more layers tends to have a higher resistance (for a given geometric coefficient κ, pores in the lower layers become very small). Therefore, in order to access a wide range of geometric coefficients with a many layered structure, we ensure that the value of the dimensionless resistance r_0

is chosen sufficiently large (see (5.32)). Our results here indicate that for a fixed geometric coefficient and fixed resistance, better performance is obtained by the branch configuration with more layers. (Note that in order to fix both the geometric coefficient and the resistance while increasing the number of layers, the size of the pore in layer 1, $a_1(0)$, must increase.)

It is also of interest to study the influence of the dimensional deposition coefficient Λ on results. This coefficient appears in our choice of timescale: $T = W/(\Lambda\alpha C_0)t$, as well as in the dimensionless parameter $\lambda = 32\Lambda\mu D^2\hat{r}_0/(\pi P_0 W^3)$ (see (5.17) and (5.29)), therefore when we change Λ, we must also rescale time in simulations. Figure 5.6(a) illustrates the effect of changing λ, plotting throughput versus the geometric coefficient for several different values of the deposition coefficient λ, while the dimensionless initial resistance is fixed at $r_0 = 1$ for a symmetric branching configuration with $m = 5$ layers. Here again, our results show that for all values of λ considered, the maximal total throughput is achieved at the smallest geometric coefficient; equivalently, at fixed initial resistance the optimum throughput is obtained for the branch configuration with pores as wide as possible in the first layer (the highest permeability gradient). Figure 5.6 (b) shows the initial particle concentration at the pore outlet, $c_m(0) = c(1, 0)$, versus the geometric coefficient, for several different values of λ with $m = 5$ and $r_0 = 1$. As shown, for larger values of λ there is little variation in $c_m(0)$, but at smaller values of λ, the geometric coefficient κ can have a significant effect on the proportion of particles removed. A common observation among all graphs in Figure 5.6(b) is the existence of a local maximum in $c_m(0)$ as κ is increased, located somewhere between 0.7 and 0.8. We note that the value $\kappa = 1/\sqrt{2}$ corresponds to a membrane of uniform porosity in the depth of the filter, suggesting that filters with either decreasing *or* increasing porosity in the membrane depth are preferable to those of uniform porosity as regards particle removal.

5.4.2 Asymmetric Branching Model Results

Since the symmetric branching geometry is highly idealized, we also briefly study asymmetric branching pore structures in a simple sub-case, where the same layered structure is assumed, but the pores in the second layer are non identical, and in subsequent layers the whole structure divides into two sub-branches, left and right, with pores decreasing geometrically in the depth of membrane with geometrical coefficients κ_L and κ_R, respectively. Consequently the total dimensionless membrane resistance is given by

$$r(t) = r_1(t) + \left(\frac{1}{r_R(t)} + \frac{1}{r_L(t)} \right)^{-1}, \tag{5.33}$$

where $r_1(t)$, $r_R(t)$ and $r_L(t)$ are resistances of the first layer, right and left sub-branches respectively, and can be obtained as

$$r_1(t) = \frac{1}{m a_1^4(t)}, \quad r_R(t) = \frac{1}{m} \sum_{i=2}^{m} \frac{1}{2^{i-2} a_{R_i}^4(t)}, \quad r_L(t) = \frac{1}{m} \sum_{i=2}^{m} \frac{1}{2^{i-2} a_{L_i}^4(t)}, \tag{5.34}$$

with

$$a_{Ri}(0) = a_1(0)\kappa_R^{i-1}, \quad a_{Li}(0) = a_1(0)\kappa_L^{i-1}, \quad \text{for} \quad 2 \le i \le m, \tag{5.35}$$

where a_1 is the radius of pore in the first layer, a_{Ri} and a_{Li} are the ith layer pore radii in the left and right sub-branches, respectively. Equation (5.33) is analogous to Kirchhoff's circuit laws and can be easily obtained using our basic flow model plus appropriate continuity equations (see (5.4)).

In Figures 5.7 (a)–(e), we present simulations where the ratio of right and left branch geometric is fixed as $\kappa_R/\kappa_L = 0.8$, and vary the radius of the top pore as for the symmetric branching model results of Figures 5.4 (a)-(e). The dimensionless deposition coefficient is set to $\lambda = 30$, the number of layers is fixed at $m = 5$, and the initial dimensionless membrane resistance (defined in (5.33)) is $r(0) = r_0 = 1$. Similar to the symmetric branching model, pore closure occurs first in the top layer

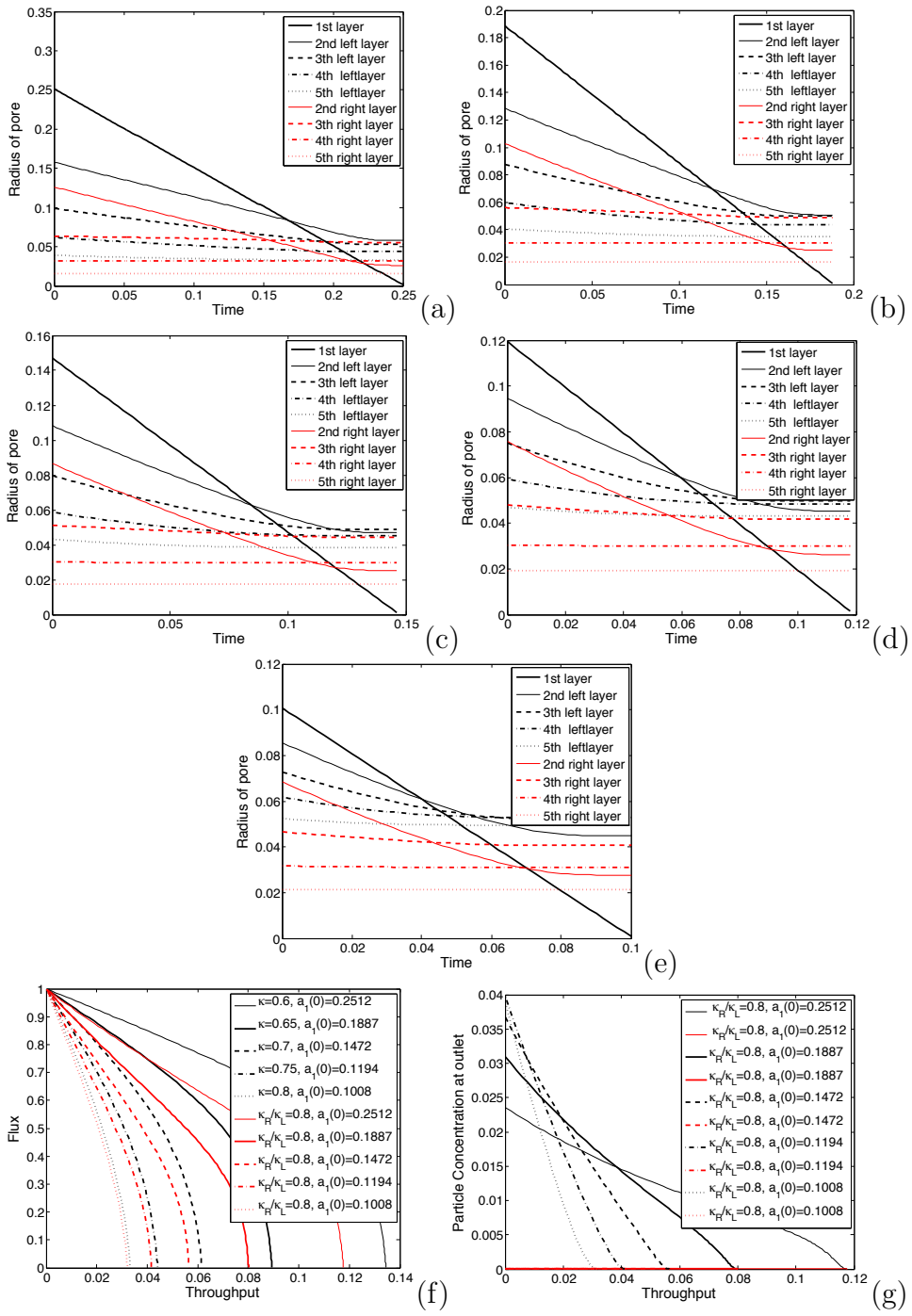

Figure 5.7 Asymmetric branching model: The pore radius evolution in each layer (indicated in the legends) with the same initial dimensionless resistance $r_0 = 1$ for the asymmetric case with the ratio of right and left branch geometric coefficients $\kappa_R/\kappa_L = 0.8$. Results are shown for different values of the first layer pore initial radius $a_1(0)$: (a) 0.2512, (b) 0.1887, (c) 0.1472, (d) 0.1194, (e) 0.1008. (f) shows total flux vs throughput for these first layer initial pore radii (red curves) and also for the corresponding symmetric cases of Figure 5.4(a)-(e) (same initial values of top pore radius and net membrane resistance). (g) shows particle concentration at outlet $c_m(t)$ versus throughput for the left (black curves) and right (red curves) sub-branches, respectively, with $\lambda = 30$ and $m = 5$.

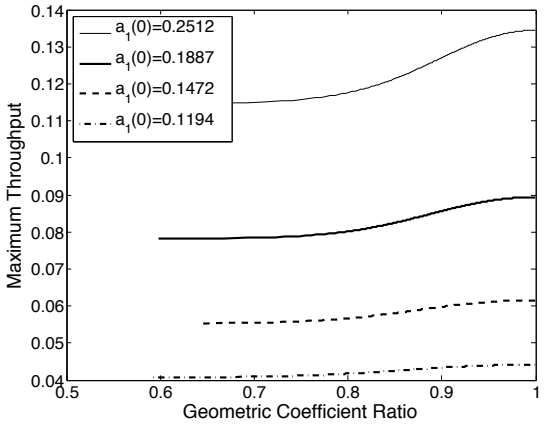

Figure 5.8 Asymmetric case: maximum throughput versus geometric coefficient ratio κ_R/κ_L, for several branching structures with different initial top pore radius and the same $r_0 = 1$, $\lambda = 30$ and $m = 5$.

for all cases, at least for the parameters used here. Furthermore, in all cases shown, the time to total blockage (the duration of the filtration process) is the same as the symmetric branching structure, since the blocking first happen in the first layer.

Figure 5.7 (f) illustrates the flux-throuput characteristics for this asymmetric case and comparing to the corresponding symmetric case (with the same initial values for the top pore radius and net resistance; see Figure 5.4(f)). Our results here indicate that breaking symmetry reduces efficiency: all asymmetric cases considered lead to less total throughput than the corresponding symmetric case. Figure 5.7 (g) shows particle concentration at outlet $c_m(t)$ versus throughput for the left (black curves) and right (red curves) sub-branches; respectively, for the above given parameters. As shown here, the particle concentration downstream in the narrower (right) sub-branch is much less than that in the left sub-branch.

To attempt to characterize the effect of breaking symmetry on filtration performance, we plot maximum throughput versus geometric coefficient ratio κ_R/κ_L in Figure (5.8) for branching structures with $m = 5$ layers, the deposition coefficient $\lambda = 30$ and the total initial resistance $r(0) = r_0 = 1$. The geometric coefficient ratio $\kappa_R/\kappa_L \in (0, 1]$ (with no loss of generality, $\kappa_R \leq \kappa_L$) characterizes the degree

of asymmetry, with a value of 1 being the symmetric case, and asymmetry increases as the ratio approaches zero. For each of the graphs in Figure (5.8), we fixed the first layer initial pore radius (as presented in the legend) then varied the value of κ_R/κ_L while keeping initial total resistance fixed at $r_0 = 1$. The results confirm the hypothesis suggested by the previous simulations: as the degree of asymmetry increases, filtration efficiency (as measured by total throughput over the filter lifetime) decreases. This effect is more prominent for those branching structures with larger pores in the top layer. Breaking the symmetry for those structures with smaller pores on top does not affect the performance very much.

5.5 Conclusions

We have presented a simple model to quantify the effects of membrane morphology on separation efficiency and fouling of a membrane filter. Our model accounts for Darcy flow through a simple bifurcating pore structure within the membrane, and for fouling by particle adsorption within pores. Our model contains one parameter that may be difficult to measure for a given system: the dimensionless attraction coefficient, λ, between the membrane-pore wall, and the particles carried by the feed solution. In principle, this could be estimated by fitting to a reliable dataset, but since it depends on properties of both membrane and feed solution, it will vary from one membrane-feed system to another.

The focus in this chapter is on development of a model that can be used to quantify the performance of a membrane filter in terms of its pore-branching characteristics. The internal morphology of real membranes is undoubtedly highly complex: here we focus mainly on a simple symmetric branching pore structure characterized by a geometric coefficient κ (which quantifies how pore size changes in the depth of the membrane) and by initial total membrane resistance r_0 (once κ and r_0 are fixed for a symmetric bifurcating pore structure, the radii of all pores

are determined). We briefly consider the effect of introducing a restricted type of asymmetry in Section 5.3, where the same layered structure (as described in symmetric branching structure) is assumed, but the pores in the second layer are non identical, and in subsequent layers the whole structure divides into two sub-branches, left and right, with pores decreasing geometrically in the depth of membrane.

Our results simulating filtration at constant pressure drop indicate that such variations in branching structure lead to different fouling patterns within the membrane. More importantly, if the initial pore radius at the top of membrane is large, it can give rise to a marked improvement in filter performance, as quantified by the total amount of filtrate processed under the same operating conditions. This is true for both symmetric and asymmetric branching structures, as shown by Figures 5.4(f) and 5.7(f), respectively while the total initial membrane resistance for all of configurations is identical. Our model also illustrates how results change as the degree of asymmetry changes, which is characterized by introducing the geometric coefficients ratio κ_R/κ_L, for right and left sub-branches, respectively. Our results in Figures 5.7(f) and 5.8 show how, as symmetry is broken, the filter performance (described above) deteriorates.

All simulations are carried out for constant pressure drop across the membrane. Our results for the symmetric membrane case indicate that smaller values of the geometric coefficient, corresponding to greater variation in pore size in the depth of the membrane (with larger pores always on top) lead to superior outcomes in terms of both total throughput and particle capture. Preliminary results for asymmetric branching structures suggest that any asymmetry will lead to decreased filtration performance as measured by total throughput over the filter lifetime.

CHAPTER 6

FUTURE WORK

In this chapter, we discuss our ongoing and future work plans, outlining the modeling directions currently being pursued, as well as possible future modeling ideas. In general, future works focus on (i) calibrating and testing the present model against reliable experimental data; (ii) exploring reasonable model parameter space to identify optimum performance within industrial constraints; (iii) considering stochasticity, such as particle interactions in our modeling; and (iv) refining the models presented in Chapters 2, 3, 4 and 5. Model refinement will follow several directions as discussed below:

6.1 Pleated Filter Membrane

Model refinement for pleated filter membranes will follow several directions: (a) improving the description of the membrane, from its current characterization in terms of identical cylindrical pores by adding the work described in Chapter 3 to the model of Chapter 2; (b) improving the model for particle adsorption within pores; (c) expanding the model to allow for *caking*, which occurs in the late stages of membrane fouling (such work, at least in the pleated filter application, can draw on the modeling and ideas of [33]); (d) quantifying membrane performance also in terms of proportion of impurities removed from the feed solution; and (e) using a more realistic (if still idealized) representation of the cartridge geometry.

6.2 Effects of Particle Diffusion

During our earlier investigations in Chapters 3 and 4, we simplified our modeling by ignoring the role of diffusion in the particle concentration equation, assuming that its effect is negligible compared with that of particle advection, and that of

the interactions between membrane pores and particles which cause the particles to adhere to the membrane. It is possible that in certain situations diffusion could play an important role (*e.g.,* in a very slow filtration process, or during the late stages of filtration when the flow rate is naturally very low due to high levels of fouling). Therefore, another avenue for future work is investigating the possible effects that particle diffusivity can have on the filtration process.

6.3 Branching Model

Though our model represents an important first step in systematically accounting for internal membrane complexity, it must be emphasized that real membranes have much more complex structure than that considered here; and that in reality multiple fouling modes are operating simultaneously (our model neglects *blocking* of pores by particles larger than them, and the *caking* that occurs in the late stages of filtration). In future work, we plan to address more complicated pore morphologies, and scenarios with multiple fouling modes operating simultaneously.

APPENDIX A

NON-PLEATED MEMBRANE MODEL

In our simulations, we compared the performance of our pleated filter model to that of the closest equivalent non-pleated membrane filter. The scenario we consider for the unpleated membrane is a three-layer sandwich (support layer in $H \geq Y \geq D/2$; filter membrane in $D/2 \geq Y \geq -D/2$; support layer in $-D/2 \geq Y \geq -H$) through which unidirectional flow is driven by an imposed pressure drop, with $P^+(X, H) = P_0$ and $P^-(X, -H) = 0$ (all notation here is as introduced in Section 2.2.2). The support layer permeability is here considered constant, $K = K_{\text{av}}$, and flow is perpendicular to the membrane ("dead end" filtration). Due to the uniformity of conditions along the X-axis, the problem is independent of X, so the support layer permeability K_{m} will vary only in time. We again assume Darcy flow through both support layers, with continuity of flux across the membrane, which sustains a pressure drop according to its permeability.

We introduce the same scalings and nondimensionalization as in Section 2.2.3, which leads to the following problems in upper and lower support layers,

$$\frac{d^2 p^{\pm}}{dy^2} = 0 \quad \text{with} \quad p^+(1) = 1, \quad p^-(-1) = 0. \tag{A.1}$$

Additional conditions matching the flow across the membrane must be imposed as in Section 2.2.3, giving

$$\frac{dp^+}{dy}(\delta/2) = \frac{dp^-}{dy}(-\delta/2) = \frac{K_{\text{m}}}{K_{\text{av}}\delta}\left[p^+(\delta/2) - p^-(-\delta/2)\right]. \tag{A.2}$$

We assume, as before, that the membrane and support layer permeabilities satisfy a certain balance: $K_{\text{m0}}/(K_{\text{av}}\delta) = \epsilon^2\Gamma$, where the measure of the resistance of the

packing material to that of the membrane, Γ, is order-one with respect to both ϵ and δ (see Eq. (2.20); note that, in this problem where the X lengthscale L does not enter the problem, this balance of permeabilities may be considered as the definition of ϵ). This allows us to seek a perturbation expansion for the pressure as $p^{\pm} = p_0^{\pm} + \epsilon^2 p_1^{\pm} + \cdots$. Using equations (A.1) and (A.2) together, we obtain

$$p^{+} = 1 + \epsilon^2 \Gamma \frac{k_{\mathrm{m}}}{k}(y-1) + O(\epsilon^4)$$
$$p^{-} = \epsilon^2 \Gamma \frac{k_{\mathrm{m}}}{k}(y+1) + O(\epsilon^4),$$

representing the fact that, as we would anticipate for a membrane whose permeability is low compared to that of the surrounding layers, the pressure is constant to leading order in each surrounding layer, with the pressure drop taking place across the membrane. To close the model, we need to couple it to the fouling model developed in Sections 2.2.2 and 2.2.3 for adsorption within pores (represented by pore radius $a(t)$; equation (2.42)) and occlusion of pores by large particles (represented by $n(t)$; equation (2.41)). For the simple 1D model here, this reduces to

$$k_{\mathrm{m}}(t) = a(t)^4 \left[n(t) + \frac{(1-n(t))}{(1+\rho_{\mathrm{b}} a(t)^4)} \right]$$
$$\text{where} \quad a(t) = 1 - \beta t, \quad \beta = \frac{8\mu E D}{\pi A_0^5 P_0 G_\infty},$$
$$\frac{dn(t)}{dt} = -a^4(t) e^{-b a(t)} n(t), \quad n(0) = 1,$$

and ρ_{b} is again a dimensionless number characterizing the additional resistance induced when a large particle blocks a pore (see Eq.(2.9)).

APPENDIX B

DERIVATION OF THE ADVECTION MODEL FOR SMALL PARTICLES

In this Appendix, we justify the advection model for the concentration of small particles presented in Chapter 3 (3.19), which in dimensionless form is equation (3.12). We begin from first principles, considering the flow of a suspension of small particles through a periodic array of identical channels (see Figure 3.2). We seek solutions for the flow and particle concentration within a single channel of radius $A(X,T)$, in cylindrical coordinates (R,θ,X) in which properties vary only in the axial direction X, the radial direction R, and time T. Throughout this appendix, unstarred dependent variables are radially-averaged over the pore cross-section, while the starred equivalents have radial dependence. Though the pore geometry changes due to the particle deposition, this occurs on a timescale much longer than that of the flow, hence we use a quasistatic model in which the flow domain $0 \leq R \leq A$ may be regarded as fixed. The pore velocity vector $\mathbf{V_p^*} = (V_p^*, 0, U_p^*)$ and the pressure P^* satisfy the Stokes equations, inertia being negligible in all scenarios of interest:

$$\nabla P^* = \mu \nabla^2 \mathbf{V_p^*}, \quad \nabla \cdot \mathbf{V_p^*} = 0, \quad 0 \leq X \leq D, \quad 0 \leq R \leq A, \tag{B.1}$$

subject to

$$P^*|_{X=0} = P_0, \quad P^*|_{X=D} = 0, \quad \mathbf{V_p^*} = 0 \quad \text{at } R = A. \tag{B.2}$$

The full advection-diffusion equation satisfied by the small-particle concentration $C^*(R,X,T)$ is:

$$\frac{\partial C^*}{\partial T} = \nabla \cdot \mathbf{Q_c^*}, \quad \mathbf{Q_c^*} = -\Xi \nabla C^* + \mathbf{V_p^*} C^* + F^* C^* \mathbf{e_r}, \tag{B.3}$$

where $\mathbf{Q_c^*}$ is the total particle flux, Ξ is the diffusion coefficient of the small particles in the feed solution and F^* is the radial particle drift speed induced by interaction with the pore wall. This term is intended to describe any forces, such as electrostatic interactions and perhaps van der Waals' forces, that act to attract particles towards the wall where they can adhere. It could be argued that this attraction force should act in the direction locally perpendicular to the wall rather than radially, requiring a more careful analysis using the normal vector; but since the pore is slender the normal direction is very close to the radial direction and, to the order we consider in our asymptotics, the end result may be shown to be the same with the purely radial term in (B.3). The boundary conditions are

$$C^*(R,0,T) = C_0, \quad \left.\frac{\partial C^*}{\partial R}\right|_{R=0} = 0, \quad \mathbf{Q_c^*}\cdot\mathbf{n} = \frac{\Lambda}{2}C^* \quad \text{at } R = A \text{ (wall deposition)}, \tag{B.4}$$

for some constant Λ. Consistent with our quasi-static assumption we solve the steady-state version of (B.3),

$$\Xi\left(\frac{1}{R}\frac{\partial}{\partial R}(R\frac{\partial C^*}{\partial R}) + \frac{\partial^2 C^*}{\partial X^2}\right) = V_p^*\frac{\partial C^*}{\partial R} + U_p^*\frac{\partial C^*}{\partial X} + \frac{1}{R}\frac{\partial (RF^*C^*)}{\partial R}, \tag{B.5}$$

where we have used the continuity equation, $\nabla\cdot\mathbf{V_p^*} = 0$. Furthermore the wall deposition boundary condition in (B.4), by use of the zero-velocity boundary condition in (B.2) and calculation of $\mathbf{n} \parallel \nabla(R-A)$, becomes

$$-\Xi\frac{\partial C^*}{\partial R} + \Xi\frac{\partial C^*}{\partial X}\frac{\partial A}{\partial X} + F^*C^* = \frac{\Lambda}{2}C^* \quad \text{at } R = A \text{ (wall deposition)}. \tag{B.6}$$

We nondimensionalize using the scalings

$$\mathbf{V}_{\mathrm{p}}^* = \frac{\pi P_0 W^2}{32\mu D}(\epsilon v_{\mathrm{p}}^*, 0, u_{\mathrm{p}}^*),\ X = Dx,\ (A,R) = W(a,r),$$
$$P^* = P_0 p^*,\ C^* = C_0 c^*,\ F^* = \frac{\pi P_0 W^2}{32\mu D}\epsilon f^*, \tag{B.7}$$

where $\epsilon = W/D \ll 1$. This gives the dimensionless form of (B.1), (B.2), (B.4), (B.5) and (B.6) as

$$\frac{32}{\pi\epsilon^2}\frac{\partial p^*}{\partial r} = \frac{1}{r}\frac{\partial}{\partial r}(r\frac{\partial v_p^*}{\partial r}) - \frac{v_p^*}{r^2} + \epsilon^2\frac{\partial^2 v_p^*}{\partial x^2}, \tag{B.8}$$

$$\frac{32}{\pi}\frac{\partial p^*}{\partial x} = \frac{1}{r}\frac{\partial}{\partial r}(r\frac{\partial u_p^*}{\partial r}) + \epsilon^2\frac{\partial^2 u_p^*}{\partial x^2}, \tag{B.9}$$

$$\frac{1}{r}\frac{\partial (r v_p^*)}{\partial r} + \frac{\partial u_p^*}{\partial x} = 0, \tag{B.10}$$

$$p^*|_{x=0} = 1, \quad p^*|_{x=1} = 0, \quad u_p^* = v_p^* = 0 \quad \text{at} \quad r = a(x), \tag{B.11}$$

$$\mathrm{Pe}\left(\frac{1}{r}\frac{\partial}{\partial r}(r\frac{\partial c^*}{\partial r}) + \epsilon^2\frac{\partial^2 c^*}{\partial x^2}\right) = v_p^*\frac{\partial c^*}{\partial r} + u_p^*\frac{\partial c^*}{\partial x} + \frac{1}{r}\frac{\partial (r f^* c^*)}{\partial r}, \quad \text{where} \quad \mathrm{Pe} = \frac{32\Xi\mu}{\epsilon^2\pi P_0 W^2}, \tag{B.12}$$

$$c^*(r,0,t) = 1, \quad \left.\frac{\partial c^*}{\partial r}\right|_{r=0} = 0, \quad -\mathrm{Pe}\frac{\partial c^*}{\partial r} + \epsilon^2\mathrm{Pe}\frac{\partial c^*}{\partial x}\frac{\partial a}{\partial x} + f^* c^* = \lambda_1 c^*, \quad \text{at } r = a, \tag{B.13}$$

where $\lambda_1 = \frac{16\Lambda\mu D^2}{\pi P_0 W^3}$. We exploit asymptotic analysis of this model, based on the assumption $\epsilon = W/D \ll 1$ and in the distinguished limit $\hat{\mathrm{Pe}} = \epsilon\mathrm{Pe} = O(1)$, representing a specific balance between advective and diffusive particle transport. We expand the dependent variables in powers of ϵ, *e.g.*:

$$\begin{aligned} c^*(r,x,t) &= c_0^*(r,x,t) + \epsilon c_1^*(r,x,t) + \epsilon^2 c_2^*(r,x,t) + \cdots, \\ f^*(r) &= f_0^*(r) + \epsilon f_1^*(r) + \epsilon^2 f_2^*(r) + \cdots, \end{aligned} \tag{B.14}$$

etc. Solving Eqs.(B.8)–(B.11) gives the pore velocity and pressure at leading order ($u_{\mathrm{p}0}^*$, $v_{\mathrm{p}0}^*$ and p_0, respectively) as

$$u_{\mathrm{p}0}^* = \frac{8}{\pi}\frac{\partial p_0^*}{\partial x}(r^2 - a^2), \quad v_{\mathrm{p}0}^* = \frac{2}{\pi}\frac{\partial}{\partial x}\big(\frac{\partial p_0^*}{\partial x}(r^3 - 2a^2 r)\big), \quad p_0^* = \frac{\int_x^1 \frac{dx'}{a^4}}{\int_0^1 \frac{dx'}{a^4}}. \tag{B.15}$$

At leading order equation (B.12) reduces to $c_0^*(r,x,t) = c(x,t)$, consistent with leading order in the boundary conditions (B.13). At order-one, we obtain

$$\frac{\hat{\mathrm{Pe}}}{r}\frac{\partial}{\partial r}(r\frac{\partial c_1^*}{\partial r}) = u_{\mathrm{p}0}^*\frac{\partial c}{\partial x} + \frac{c}{r}\frac{\partial (r f_0^*)}{\partial r}, \tag{B.16}$$

where $u_{\mathrm{p}0}^*$ is the leading-order dimensionless axial pore velocity. Using the operator $\frac{1}{\pi a^2}\int_0^{2\pi}\int_0^a \cdot\, r dr d\theta$ to take the cross sectional average of (B.16), we obtain

$$\frac{2\hat{\mathrm{Pe}}}{a}\frac{\partial c_1^*}{\partial r}\bigg|_{r=a} = u_{\mathrm{p}}\frac{\partial c}{\partial x} + \frac{2c}{a}f_0^*(a), \tag{B.17}$$

where u_{p} denotes the cross-sectional average of $u_{\mathrm{p}0}^*$, obtained from (B.15)

$$u_p = -\frac{4}{\pi}a^2\frac{\partial p}{\partial x}, \tag{B.18}$$

where, in line with our notation, p is the cross-sectional average of p_0^* (note that here $p \equiv p_0^*$). In addition the second boundary condition in (B.13) gives, at $O(1)$

$$-\hat{\mathrm{Pe}}\frac{\partial c_1^*}{\partial r} + c f_0^* = \lambda_1 c, \quad \text{at} \quad r = a. \tag{B.19}$$

Combining (B.17) and (B.19) gives the desired result (equation (3.19))

$$u_{\mathrm{p}}\frac{\partial c}{\partial x} = -\hat{\lambda}\frac{c}{a}, \quad \hat{\lambda} = \frac{32\Lambda\mu D^2}{\pi P_0 W^3}, \quad c_0(0,t) = 1. \tag{B.20}$$

APPENDIX C

THE MODEL FOR SPECIFIED FLUX

Here, we briefly outline how the results of Chapter 3 change if conditions of constant flux, rather than constant pressure drop, are applied. We first outline the modifications to the model, then present a sample simulation.

C.1 Model Summary

The original model (3.2)–(3.15) still holds, but now P_0 in (3.2) must be considered a function of time, $P_0(T)$, while equation (3.3) integrates directly to give

$$\pi A^2 U_{\mathrm{p}} = Q_{\mathrm{pore}}, \tag{C.1}$$

where Q_{pore} is the constant flux per pore. We nondimensionalize the model using the same scalings as in (3.16), except for

$$P = \frac{8\mu D Q_{\mathrm{pore}}}{\pi W^4} p, \quad (U, U_{\mathrm{p}}) = \frac{Q_{\mathrm{pore}}}{4W^2}(1, u_p). \tag{C.2}$$

The resulting model is easily reduced to:

$$\frac{dn}{dt} = -\, n\left(\frac{1-n}{1+\rho_{\mathrm{b}} a^4} + n\right)^{-1} (1 - g(a))\bigg|_{x=0}, \quad \frac{\partial c}{\partial x} = -\tilde{\lambda} c a, \quad \frac{\partial a}{\partial t} = -\tilde{\beta} c, \tag{C.3}$$

where

$$\tilde{\beta} = \frac{1}{Q_{\mathrm{pore}} G_\infty}, \quad \tilde{\lambda} = \frac{\pi \Lambda W D}{Q_{\mathrm{pore}}}, \tag{C.4}$$

with modified Darcy pressure p within the membrane given by

$$p = \int_x^1 \frac{dx'}{a^4(\frac{1-n}{1+\rho_{\mathrm{b}} a^4} + n)}. \tag{C.5}$$

The model (C.3) must be solved subject to the same boundary and initial conditions (3.27). Note that equation (C.5) allows the pressure $p(0,t)$ at the membrane inlet (the dimensionless pressure drop in this constant flux case) to be evaluated.

C.2 Results

Figures C.1 (a)-(e) show results for the same initial pore profiles given in (3.31). Figure C.1(f) shows the inverse pressure drop versus throughput for each of those pore profiles.

The results differ quite significantly from those for the constant pressure case. In contrast to those simulations, the pore radius evolution is now much more uniform along the pore length. Pore closure still always occurs first at the upstream end of the pores for the cases shown here, but with a smaller value of $\tilde{\lambda}$ this is not inevitable. Since the total flux through the system is held constant, the flux-throughput graph gives no characterization of the system in these simulations, hence we instead plot how the pressure drop rises over time as blocking occurs in order to maintain the specified flow rate (Fig. C.1(e)). Mathematically, the pressure must go to infinity within finite time to sustain the same flux as total blockage is reached, but this is of course not practical. In reality, the driving pressure is increased until some specified maximum value (based on practical constraints of the system under consideration) is reached. Following this, the system then reverts to the fixed pressure drop operation, with the pressure fixed at this maximal value, and the subsequent behavior can then be modeled as discussed in Section 3.3.1. As with the constant pressure simulations, the best overall performance (in terms of efficiency) is provided by the pores of monotone decreasing radius (profile $a_3(x)$ in (3.31)), and the worst performance by pores of monotone increasing radius (profile $a_2(x)$). However, the differences in performance are less pronounced than for the constant pressure case.

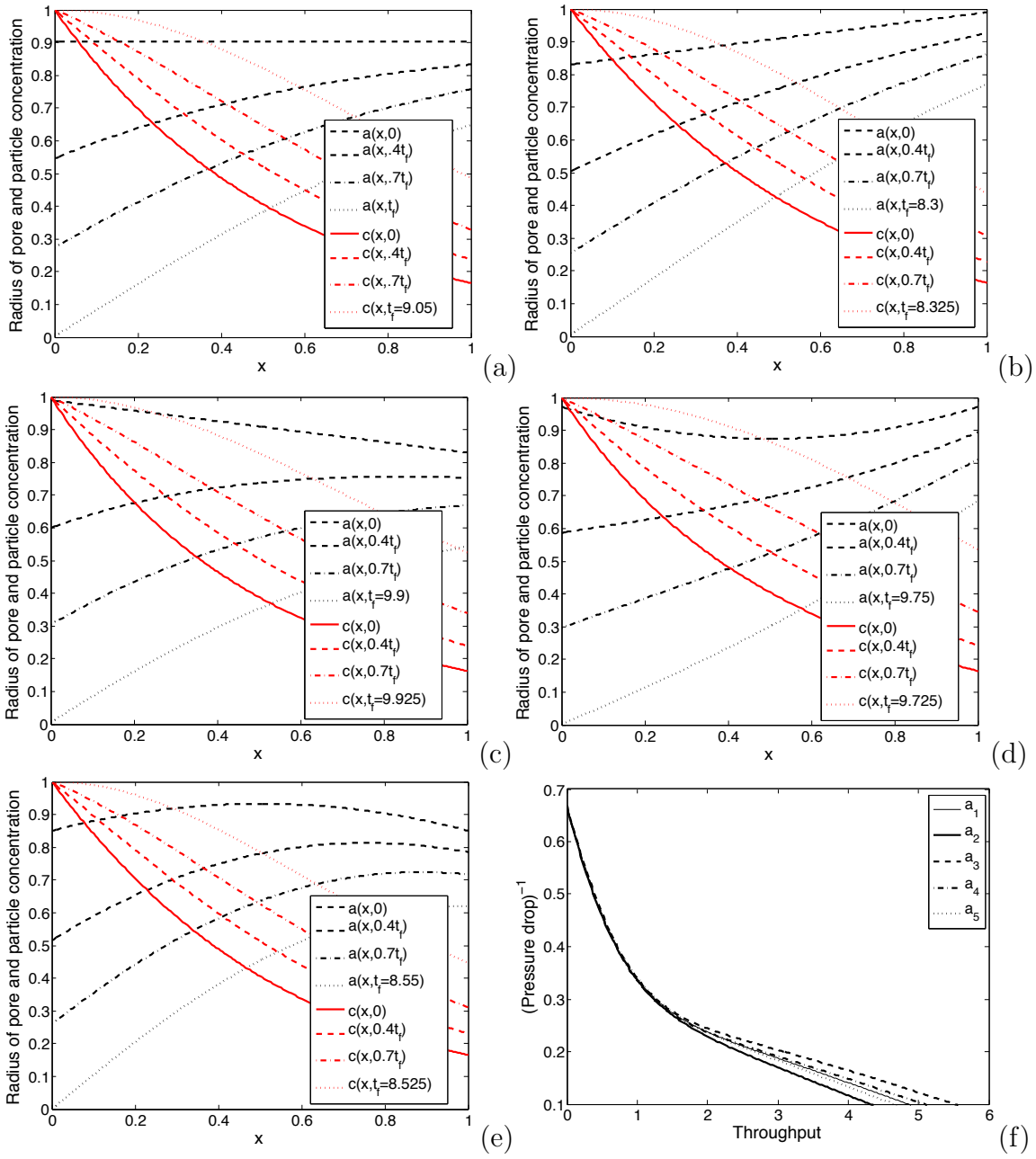

Figure C.1 Simulations at constant flux: The pore radius at several different times at different final blocking times (t_{f}, indicated in the legends) for different initial pore radius profiles: (a) $a_1(x,0) = 0.904$, (b) $a_2(x,0) = 0.16x + 0.83$, (c) $a_3(x,0) = 0.99 - 0.16x$, (d) $a_4(x,0) = 0.874 + 0.39(x-0.5)^2$, (e) $a_5(x,0) = 0.933 - 0.33(x-0.5)^2$, and (f): inverse pressure drop vs throughput for those initial pore radius profiles with homogeneous distributions of large-particle sizes, (3.28) ($g(s) = 0$), $\tilde{\lambda} = 2$, $\beta = 0.1$ and $\rho_{\mathrm{b}} = 2$.

BIBLIOGRAPHY

[1] *Reproduced from Pall Corporation Power Generation Catalog, available at* `http://www.pall.com/pdfs/Power-Generation/PowerGeneration_Catalog.pdf` *(accessed on 8/1/2013).*

[2] `http://web.njit.edu/ rmoore/MPI2014/MPI2014program.php (accessed on 2/1/2015)`, 2014.

[3] M. Abramowitz and I.A. Stegun. *Handbook of mathematical functions with formulas, graphs, and mathematical tables*, volume 9. Dover, New York, 1972.

[4] P. Apel. Track etching technique in membrane technology. *Radiation Measurements*, 34(1):559–566, 2001.

[5] P. Bacchin, P. Aimar, and R.W. Field. Critical and sustainable fluxes: theory, experiments and applications. *Journal of Membrane Science*, 281(1):42–69, 2006.

[6] G. Bolton, D. LaCasse, and R. Kuriyel. Combined models of membrane fouling: development and application to microfiltration and ultrafiltration of biological fluids. *Journal of Membrane Science*, 277(1):75–84, 2006.

[7] G.R. Bolton, A.W. Boesch, and M.J. Lazzara. The effects of flow rate on membrane capacity: development and application of adsorptive membrane fouling models. *Journal of Membrane Science*, 279(1):625–634, 2006.

[8] P.M. Boyle, B.C. Houchens, and A.S. Kim. Simulation of colloidal fouling by coupling a dynamically updating velocity profile and electric field interactions with force bias monte carlo methods for membrane filtration. *Journal of Colloid and Interface Science*, 399:77–86, 2013.

[9] A.I. Brown. *An ultra scale-down approach to the rapid evaluation of pleated membrane cartridge filter performance.* PhD thesis, UCL (University College London), UK, 2011.

[10] A.I. Brown, P. Levison, N.J. Titchener-Hooker, and G.J. Lye. Membrane pleating effects in 0.2 μm rated microfiltration cartridges. *Journal of Membrane Science*, 341(1):76–83, 2009.

[11] A.I. Brown, N.J. Titchener-Hooker, and G.J. Lye. Scale-down prediction of industrial scale pleated membrane cartridge performance. *Biotechnology and Bioengineering*, 108(4):830–838, 2011.

[12] J.C. Chen and A.S. Kim. Brownian dynamics, molecular dynamics, and monte carlo modeling of colloidal systems. *Advances in Colloid and Interface Science*, 112(1):159–173, 2004.

[13] J.C. Chen and A.S. Kim. Monte carlo simulation of colloidal membrane filtration: Principal issues for modeling. *Advances in Colloid and Interface Science*, 119(1):35–53, 2006.

[14] Y. Chen, X. Hu, and H. Kim. Monte carlo simulation of pore blocking phenomena in cross-flow microfiltration. *Water Research*, 45(20):6789–6797, 2011.

[15] Y. Chen and H. Kim. Monte carlo simulation of pore blocking and cake formation by interfacial interactions during membrane filtration. *Desalination*, 233(1-3):258–266, 2008.

[16] M.P. Dalwadi, I.M. Griffiths, and M. Bruna. Understanding how porosity gradients can make a better filter using homogenization theory. In *Proc. R. Soc. A*, volume 471, page 20150464. The Royal Society, 2015.

[17] R.C. Daniel, J.M. Billing, R.L. Russell, R.W. Shimskey, H.D. Smith, and R.A. Peterson. Integrated pore blockage-cake filtration model for crossflow filtration. *Chemical Engineering Research and Design*, 89(7):1094–1103, 2011.

[18] P. Dechadilok and W.M. Deen. Hindrance factors for diffusion and convection in pores. *Industrial and Engineering Chemistry Research*, 45(21):6953–6959, 2006.

[19] S. Fotovati, S.A. Hosseini, H.V. Tafreshi, and B. Pourdeyhimi. Modeling instantaneous pressure drop of pleated thin filter media during dust loading. *Chemical Engineering Science*, 66(18):4036–4046, 2011.

[20] S. Giglia, K. Rautio, G. Kazan, K. Backes, M. Blanchard, and J. Caulmare. Improving the accuracy of scaling from discs to cartridges for dead end microfiltration of biological fluids. *Journal of Membrane Science*, 365(1):347–355, 2010.

[21] S. Giglia and G. Straeffer. Combined mechanism fouling model and method for optimization of series microfiltration performance. *Journal of Membrane Science*, 417:144–153, 2012.

[22] H.P. Grace. Structure and performance of filter media. ii. performance of filter media in liquid service. *AIChE Journal*, 2(3):316–336, 1956.

[23] I.M. Griffiths, A. Kumar, and P.S. Stewart. A combined network model for membrane fouling. *Journal of Colloid and Interface Science*, 432:10–18, 2014.

[24] I.M. Griffiths, A. Kumar, and P.S. Stewart. Designing asymmetric multilayered membrane filters with improved performance. *Journal of Membrane Science*, 511:108–118, 2016.

[25] P.H. Hermans and H.L. Bredee. Zur kenntnis der filtrationsgesetze. *Recueil des Travaux Chimiques des Pays-Bas*, 54(9):680–700, 1935.

[26] J. Hermia. Constant pressure blocking filtration law application to powder-law non-newtonian fluid. *Trans. Inst. Chem. Eng.*, 60:183–187, 1982.

[27] C.C. Ho and A.L. Zydney. Effect of membrane morphology on the initial rate of protein fouling during microfiltration. *Journal of Membrane Science*, 155(2):261–275, 1999.

[28] C.C. Ho and A.L. Zydney. A combined pore blockage and cake filtration model for protein fouling during microfiltration. *Journal of Colloid and Interface Science*, 232(2):389–399, 2000.

[29] K.J. Hwang, C.Y. Liao, and K.L. Tung. Analysis of particle fouling during microfiltration by use of blocking models. *Journal of Membrane Science*, 287(2):287–293, 2007.

[30] E. Iritani. A review on modeling of pore-blocking behaviors of membranes during pressurized membrane filtration. *Drying Technology*, 31(2):146–162, 2013.

[31] N.B. Jackson, M. Bakhshayeshi, A.L. Zydney, A. Mehta, R. Reis, and R. Kuriyel. Internal virus polarization model for virus retention by the ultipor® vf grade dv20 membrane. *Biotechnology Progress*, 30(4):856–863, 2014.

[32] D.M. Kanani, W.H. Fissell, S. Roy, A. Dubnisheva, A. Fleischman, and A.L. Zydney. Permeability–selectivity analysis for ultrafiltration: Effect of pore geometry. *Journal of Membrane Science*, 349(1):405–410, 2010.

[33] J.R. King and C.P. Please. Asymptotic analysis of the growth of cake layers in filters. *IMA, Journal of Applied Mathematics*, 57(1):1–28, 1996.

[34] A. Kumar. *Private Communication, Pall Corporation*, 2014.

[35] A. Kumar. Effect of prefiltration on scalability of 0.1 μm-rated membrane filters. *Bioprocess International, Industry Yearbook*, 7(part 7):129–130, 2009.

[36] A. Kumar, J. Martin, and R. Kuriyel. Scale-up of sterilizing-grade membrane filters from discs to pleated cartridges: effects of operating parameters and solution properties. *PDA Journal of Pharmaceutical Science and Technology*, 69(1):74–87, 2015.

[37] A. Mehta and A.L. Zydney. Permeability and selectivity analysis for ultrafiltration membranes. *Journal of Membrane Science*, 249(1):245–249, 2005.

[38] A. Mehta and A.L. Zydney. Effect of membrane charge on flow and protein transport during ultrafiltration. *Biotechnology Progress*, 22(2):484–492, 2006.

[39] F. Meng, S.R. Chae, A. Drews, M. Kraume, H.S. Shin, and F. Yang. Recent advances in membrane bioreactors (mbrs): membrane fouling and membrane material. *Water Research*, 43(6):1489–1512, 2009.

[40] S. Mochizuki and A.L. Zydney. Theoretical analysis of pore size distribution effects on membrane transport. *Journal of Membrane Science*, 82(3):211–227, 1993.

[41] S.V. Polyakov, E.D. Maksimov, and V.S. Polyakov. One-dimensional microfiltration models. *Theoretical Foundations of Chemical Engineering*, 29(4):329–332, 1995.

[42] V.S. Polyakov. Design of microfilters operating under depth-filtration conditions. *Theoretical Foundations of Chemical Engineering*, 32(1):18–22, 1998.

[43] Y.S. Polyakov. Depth filtration approach to the theory of standard blocking: Prediction of membrane permeation rate and selectivity. *Journal of Membrane Science*, 322(1):81–90, 2008.

[44] Y.S. Polyakov and A.L. Zydney. Ultrafiltration membrane performance: Effects of pore blockage/constriction. *Journal of Membrane Science*, 434:106–120, 2013.

[45] R.E. Problestein. Physicochemical hydrodynamics, an introduction, 1994.

[46] N.S. Pujar and A.L. Zydney. Charge regulation and electrostatic interactions for a spherical particle in a cylindrical pore. *Journal of Colloid and Interface Science*, 192(2):338–349, 1997.

[47] S. Roy. Innovative use of membrane technology in mitigation of ghg emission and energy generation. *Procedia Environmental Sciences*, 35:474–482, 2016.

[48] P. Sanaei and L.J. Cummings. Flow and fouling in membrane filters: effects of membrane morphology. *Journal of Fluid Mechanics*, 818:744–771, 2017.

[49] P. Sanaei, G.W. Richardson, T. Witelski, and L.J. Cummings. Flow and fouling in a pleated membrane filter. *Journal of Fluid Mechanics*, 795:36–59, 2016.

[50] A. Santos, P. Bedrikovetsky, and S. Fontoura. Analytical micro model for size exclusion: Pore blocking and permeability reduction. *Journal of Membrane Science*, 308(1):115–127, 2008.

[51] R.G.M. Van der Sman, H.M. Vollebregt, A. Mepschen, and T.R. Noordman. Review of hypotheses for fouling during beer clarification using membranes. *Journal of Membrane Science*, 396:22–31, 2012.

[52] R. van Reis and A.L. Zydney. Bioprocess membrane technology. *Journal of Membrane Science*, 297(1):16–50, 2007.

[53] M. Wessling. Two-dimensional stochastic modeling of membrane fouling. *Separation and Purification Technology*, 24(3):375–387, 2001.

[54] L.J. Zeman and A.L. Zydney. Microfiltration and ultrafiltration: principles and applications. *M. Dekker*, 1996.

[55] A.L. Zydney. High performance ultrafiltration membranes: pore geometry and charge effects. *Inorganic, Polymeric, and Composite Membranes: Structure, Function, and other Correlations. Elsevier, Netherland, Amsterdam*, pages 333–352, 2011.